Alexandre Cardaillac

Towards autonomous underwater navigation and perception for end-to-end ship hull inspection

Thesis for the degree of Philosophiae Doctor

Trondheim, March 2024

Norwegian University of Science and Technology
Faculty of Engineering
Department of Marine Technology

NTNU
Norwegian University of
Science and Technology

"Nothing in life is to be feared, it is only to be understood. Now is the time to understand more, so that we may fear less."
— Marie Curie, Nobel Laureate in Chemistry and Physics

Abstract

This thesis presents an innovative and integrated solution for end-to-end underwater ship hull inspection using a small and low-cost Remotely Operated Vehicle (ROV). In a world where maritime activities have significant and distinctive impacts in many sectors, where over 5000 ships operate daily, safety concerns from the structural integrity of the hulls are raised. These concerns are not only related to the ship's crew safety if there are apparent damages to the hull, but also related to the environmental cause. Indeed, an unmaintained hull will provoke a significant rise of the fuel consumption over time. Although successful, traditional inspection methods in dry docks fail to be fast-paced, which would decrease the ship's down time and cost. Remote inspections are promising to address this issue. ROV-based inspections enable efficient visual documentation while the ship is still in water and docked. Further automating the process increases the efficiency since it brings consistency and faster data processing. With the inspection culture and regulations in mind, this thesis aims to achieve a fully automated inspection of underwater ship hulls, i.e., from the deployment of the vehicle to the assistance of the surveyor to generate the inspection reports. To achieve this, the drone is equipped with a set of navigation and perception sensors to ensure hull relative navigation and guarantee full visual coverage. Maneuvering based guidance is employed to navigate along the hull. Its relative orientation and distance to the ROV is computed using a forward looking sonar and set as constraints to the guidance mechanism to make sure the vehicle is facing the hull at a constant distance. Additionally, the sonar enables online acoustic mapping of the hull, tracking of the inspection progress, and visual representations of the hull. This relies on a flat surface assumption when operating at close range. When inspecting particular points of interests such as propellers, keels, and gratings, acoustic and optical data are combined to provide a better understanding of the structure through accurate 3D modelling of the scene and improved localisation of the vehicle. The acoustic-visual combination occurs at the feature level based on the relative distances of the detected points to the perception sensors. To constrain the search space of the features that can be matched, the intersection area between the sonar acoustic beams and the camera image plane is dynamically estimated. The acoustic-visual combination is activated when the specific areas of interest are detected. This is done through the use of deep learning models, trained on a tailor made dataset for image classification and semantic segmentation of ship parts and faults. Verified by domain experts, this dataset was made to match the needs of the surveyors and is the first of its kind publicly

available for ship hull inspection systems. Sequences of the data collected by the vehicle during the mission are automatically marked based on their relevance for the inspection to further assist the surveyor. These data markers are attached with visual data, models and the ROV telemetry to provide insights and to be compatible with the guidelines from the international regulations. The complete solution was tested in ten harbors and on six ships of different size and strutures to ensure the adaptability of the methods and consistency of the results. By taking advantage of the available sensors, it was possible to move along the hull with high precision at the same time as mapping it. The proposed methods outperformed the related existing one and showed new promising opportunities for future research. Finally, the adaptability of the proposed solution made it possible to apply it for inspection of different structures than ship hulls, including aquaculture fish net pens and subsea structures.

Preface

This thesis is submitted in partial fulfillment of the requirements for the degree of Philosophiae Doctor (PhD) at the Norwegian University of Science and Technology (NTNU), Trondheim.

Acknowledgements

List of Publications

During the course of the PhD, ten articles were published. Among them, seven were published in conference proceedings, and the remaining three submitted to journals (one published, one accepted, one submitted). The full papers can be found in the Part II of the thesis. They are listed in reversed chronological order of submission.

Conference papers:

A. **A. Cardaillac**, H. B. Amundsen, E. Kelasidi, and M. Ludvigsen, "Application of maneuvering based control for autonomous inspection of aquaculture net pens," in *2023 8th Asia-Pacific Conference on Intelligent Robot Systems (ACIRS)*, 2023, pp. 44–51. DOI: 10.1109/ACIRS58671.2023.10239708

B. M. Scheiber, **A. Cardaillac**, C. Brommer, S. Weiss, and M. Ludvigsen, "Modular multi-sensor fusion for underwater localization for autonomous rov operations," in *OCEANS 2022, Hampton Roads*, 2022, pp. 1–5. DOI: 10.1109/OCEANS47191.2022.9977298

C. J. Hirsch, B. Elvesæter, **A. Cardaillac**, B. Bauer, and M. Waszak, "Fusion of multi-modal underwater ship inspection data with knowledge graphs," in *OCEANS 2022, Hampton Roads*, 2022, pp. 1–9. DOI: 10.1109/OCEANS47191.2022.9977371

D. **A. Cardaillac** and M. Ludvigsen, "Marine snow detection for real time feature detection," in *2022 IEEE/OES Autonomous Underwater Vehicles Symposium (AUV)*, 2022, pp. 1–6. DOI: 10.1109/AUV53081.2022.9965895

E. **A. Cardaillac** and M. Ludvigsen, "A communication interface for multi-layer cloud computing architecture for low cost underwater vehicles*," *IFAC-PapersOnLine*, vol. 55, no. 14, pp. 77–82, 2022, 11th IFAC Symposium on Intelligent Autonomous Vehicles IAV 2022. DOI: 10.1016/j.ifacol.2022.07.586

F. **A. Cardaillac** and M. Ludvigsen, "Path following for underwater inspection allowing manoeuvring constraints," in *Intelligent Autonomous Systems 17*, Cham: Springer Nature Switzerland, 2023, pp. 867–880. DOI: 10.1007/978-3-031-22216-0_58

G. **A. Cardaillac** and M. Ludvigsen, "Ruled path planning framework for safe and dynamic navigation," in *OCEANS 2021: San Diego – Porto*, 2021, pp. 1–7. DOI: 10.23919/OCEANS44145.2021.9705699

Journal papers:

H. **A. Cardaillac** and M. Ludvigsen, "Camera-sonar combination for improved underwater localization and mapping," *IEEE Access*, vol. 11, pp. 123 070–123 079, 2023. DOI: 10.1109/ACCESS.2023.3329834

I. **A. Cardaillac**, R. Skjetne, and M. Ludvigsen, "Rov-based autonomous maneuvering for ship hull inspection with coverage monitoring," *Journal of Intelligent & Robotic Systems*, 2023, [IN REVIEW]

J. M. Waszak, **A. Cardaillac**, B. Elvesæter, F. Rødølen, and M. Ludvigsen, "Semantic segmentation in underwater ship inspections: Benchmark and data set," *IEEE Journal of Oceanic Engineering*, pp. 1–12, 2022. DOI: 10.1109/JOE.2022.3219129

Contents

Acronyms

ABS American Bureau of Shipping

AUV Autonomous Underwater Vehicle

CLAHE Contrast Limited Adaptive Histogram Equalisation

CV Computer Vision

DNV Det Norske Veritas

DoF Degrees of Freedom

DR Dead Reckoning

DVL Doppler Velocity Log

EKF Extended Kalman Filter

FLS Forward Looking Sonar

FoV Field-of-View

FPS Frames Per Second

GNSS Global Navigation Satellite System

GPS Global Positioning System

GPU Graphics Processing Unit

IACS International Association of Classification Societies

IMO International Maritime Organization

IMU Inertial Measurement Unit

INS Inertial Navigation System

IoU Intersection over Union

KF Kalman Filter

LBL Long Short Baseline

LOS Line Of Sight

MaRS Modular and Robust Sensor-fusion

MAV Micro Aerial Vehicle

MBFLS Multi Beam Forward Looking Sonar

MLE Maximum Likelihood Estimation

NTNU Norwegian University of Science and Technology

PhD Philosophiae Doctor

PID Proportional Integral Derivative

PLM Pig Loop Module

PoI Point of Interest

PRM Probabilistic Roadmap

PRRG Parameterized Rapidly-exploring Random Graph

RANSAC Random Sample Consensus

RD Research Direction

RINA Registro Italiano Navale

ROS Robotic Operating System

ROV Remotely Operated Vehicle

RRT Rapidly-exploring Random Tree

RTSP Real-Time Streaming Protocol

SBL Short Baseline

SLAM Simultaneous Localization and Mapping

SOTA State Of The Art

USBL Ultra Short Baseline

VO Visual Odometry

VR Virtual Reality

List of Figures

List of Tables

Part I

Thesis Content

Chapter 1

Introduction

> *"The sea is everything. It covers seven tenths of the terrestrial globe. Its breath is pure and healthy. It is an immense desert, where man is never lonely, for he feels life stirring on all sides."*
>
> — Jules Verne, Novelist

1.1 Background

With approximately 56,000 medium and large ships navigating the world's seas, maintaining and servicing these colossal vessels, particularly outer hull inspection and maintenance, have remained predominantly reliant on manual labor. This PhD thesis aims to contribute to robotic methods for ship hull inspections. The central objective of this doctoral research, is to bridge the existing gap between the current state of ship inspection and service robotics and the desired capabilities essential for automated maintenance practices but providing the robotic capabilities required.

1.1.1 Ship Life-cycle and Inspection Standards

The maritime industry has become a crucial part of the world's economy and more than 80% of the global trade rely on ship transport according to the United Nations [11]. The shipping industry includes most of the activities that are done at sea, such as the transportation of goods, products, and people. Vessels such as container ships, tankers, cruise ships, ferries, but also smaller vessels like fishing boats are employed.

The ship owners are required by international regulations to perform inspections to verify the structural integrity of their vessels. They are exposed to harsh oceanic environmental conditions and technical incidents will rise safety and environmental concerns. Structural degradation will develop over time, and cracks and corrosion
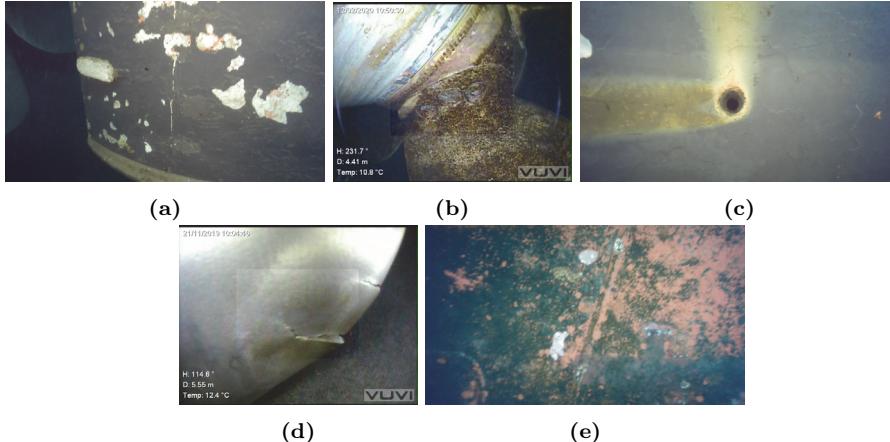
Figure 1.1: Sample underwater images of degradation that can appear on a hull, such as paint peel, marine growth, corrosion and cracks. [10]

will require costly repairs [12]. Accumulated bio-fouling will have a significant impact on the ship hydrodynamic resistance leading to increased fuel consumption and decreased speed as it generates friction [13], [14]. Sample images of such degradation on the hull are displayed in Figure 1.1.

Inspection and maintenance operations has to be performed efficiently and quickly to be able to reduce ship down-time so that the ship owners can resume their activities as soon as possible. Traditionally, outer hull inspection and maintenance services are completed in dry dock, and often performed manually by trained and qualified workers. This can take a full week of work, for this period the ship is immobilised and out of service. Fast and efficient inspection and maintenance operations can improve quality and utilization to enhance economical sustainability for the vessel operators.

Recently, service providers have taken advantage of modern technologies by deploying Remotely Operated underwater Vehicles (ROVs) to run a prior inspection to visually verify the structural integrity of the hull. However, skilled operators are required and their performance directly impact the quality of the inspection.

Emerging approaches include the use of autonomous systems where the robotic vehicles are used as mobile agents that efficiently and consistently achieve the required inspections. However, automated inspections still represent considerable technical challenges and one important task in the operation is to make the vehicle able to localise itself in the world and relative to the hull. Additionally, the required perception tasks incorporate specific challenges due to the underwater environment, with light attenuation, refraction and scattering, as well as the acoustic disturbances caused by sound reflections causing multi path features, ambient noise and ringing in man made structures.

The maritime industry is characterized by high volumes with many repetitive tasks that take humans a significant amount of time, whether it is because of safety concerns, or to comply with the current related regulations. Furthermore, the continuous expansion of the maritime industry results in the large development of subsea structures which require inspection, maintenance and repair operations. Since the appearance of ROVs, operations are simpler and safer to conduct and they have proven to be extremely valuable in ocean related applications [15]. They have replaced in most cases manned submersibles and divers in such operations.

1.1.2 Existing Underwater Robotic Technologies

Localisation

Navigation and perception for situational awareness are the central challenges for autonomous underwater operations. Underwater localisation is traditionally solved using Inertial Navigation System (INS) and Dead Reckoning (DR) methods. However, the position and orientation estimates will drift over time depending on the quality of the instruments used. Sensor fusion using filters such as Kalman Filters (KFs) are employed to quantify and compensate for the error components for the state estimates. Underwater acoustic signals are often used for position measurements and have the advantage to propagate well in water and can reach long distances. Acoustic ranging systems using Ultra Short Baseline (USBL), Short Baseline (SBL), or Long Short Baseline (LBL), enable the triangulation of the vehicle's localisation. The robot is equipped with an acoustic transmitter emitting signals that are received by an array of hydrophones which process them to obtain the source's position. The results are then usually fused with acceleration, velocity and orientation measurements in an integrated navigation system [16]–[18]. Although very efficient in open sea, such systems tend to perform poorly in enclosed space as the structures can block acoustic signals or create the multi-path effect. Doppler Velocity Log (DVL) sensors allow the computation of the vehicle's velocity relative to a surface, e.g., the sea bottom or a wall. It is achieved using acoustic beams and by measuring their Doppler shift. This sensor has become widely used because it presents a zero-mean bias and has no error growth over time for the velocity estimate. It is therefore frequently used as an aid to INS [19]–[21].

Close to objects and structures, visual features detected by a camera can be used to improve the navigation by providing a position estimate. Visual Odometry (VO) or Simultaneous Localization and Mapping (SLAM) [22] methods are often used to obtain position estimates of the vehicle at the same time as the surrounding objects positions. The work done in this field can be divided into two categories: direct approaches and feature-based approaches. Direct SLAM methods use the intensity values of pixels in an image and track them from frame to frame with the goal to minimise the photometric errors. Dense Tracking And Mapping (DTAM) [23] was one of the first implementation of the approach. It estimates dense depth maps that are used to reconstruct the scene. However, the proposed solution heavily relies on the Graphics Processing Unit (GPU), which makes it difficult to deploy in robotic applications. The Large Scale Direct SLAM (LSD-SLAM) [24] approach

proposed a direct SLAM solution more computationally efficient by selecting regions of pixels instead of all of them. High-gradient regions are selected and tracked as they hold most of the image information. More work has been done in this field [25]–[27] but this approach is particularly challenging to apply to underwater environment because of the disturbance and unstable light source which have a direct impact on the pixel intensities. This makes direct methods unavailable for underwater visual SLAM, or not in its current form. Indirect methods, or feature-based methods consist of detecting keypoints in the image and matching them between successive images. This approach is more robust against noise as it is more stable and less sensitive to the illumination of objects, which makes it a pertinent choice for underwater applications. Originally, monocular SLAM was solved using an Extended Kalman Filter (EKF) [28], [29] by doing a guided search by correlation. But keyframe-based approaches were found to be more appropriate as they estimate the pose and the map using selected frames, leaving computational space for optimisation method such as bundle adjustment. Parallel Tracking And Mapping (PTAM) [30] was one of the first and most representative method to use this optimisation method in real-time in addition to separating the tracking and mapping into two parallel threads. ORB-SLAM [31]–[33] is a complete SLAM system including bundle adjustment, loop closure, and relocalization. This enables short-term, mid-term, and long-term data association which results in very accurate results. ORB-SLAM is often used as the based method for underwater SLAM [34]–[38] because of its capabilities and ease of use. Nevertheless, there are successful attempts to dedicated underwater SLAM frameworks which better account for the underwater environment properties [39]–[41]. Overall, SLAM is especially important for scene understanding and situation awareness as it provides processed and robot-readable real-time data about what it sees.

Path Planning

In path planning for underwater vehicles, the vertical dimension of the environment must be taken into account. The path planning problem can be divided into two main categories: single robot targeted planning, and coverage planning. The former aims at defining a path to bring the robot at a target position while the latter defines a path that go through areas of interest to cover them respectively to a sensor. In traditional path planning methods, graphs and trees are frequently employed. They both are a collection of nodes, but their connections differ. In graphs, the nodes are inter-connected with directed or undirected edges, and have no root node. In trees, the edges are always directed and are formed with a parent and a child node. Graphs enable redundancy, loops, and higher level of complexity, but require the use of a search algorithm to extract a path. The most common algorithms are the Dijkstra algorithm [42], A* [43], and fast marching [44]. The graphs and trees are frequently generated using sampling-based methods which reduce the complexity of the state space compared to a grid, and therefore can significantly increase the efficiency and search speed of the optimal solution. The Rapidly-exploring Random Tree (RRT) [45] and Probabilistic Roadmap (PRM) [46] algorithms laid the basis of this category of methods. They both randomly sample points in the state space and create collision free routes. An RRT solution develops a tree with roots in the initial

configuration, e.g. the location of the robot, and tends to expand towards large and empty areas due to its probabilistic properties. The PRM solution has similar aspects but expands a graph in a bounded area instead of a tree and enables multi-query requests. Both algorithms were later updated to make them asymptotically optimal [47], RRT* and PRM*. Both graphs and trees are used in marine robotics with applications in exploration, monitoring, and search and rescue [48]–[53].

Coverage path planning consists of creating a path that enables sensor coverage of specific areas. It should be designed with as few repetitions and crossings as possible, be as short as possible, and should not require complex maneuvering. In underwater monitoring applications, patterns similar to or adapted version of a lawnmower pattern are very often employed [54]–[56]. However, when the task becomes more complex, for example detailed inspections of subsea structures, lawnmower-based patterns are not efficient. Therefore, the planning also has to adapt, either online according to the mission findings, or offline, if enough data is available prior to the deployment of the vehicle [57]–[59].

Guidance and Path Following

Path following is fundamental for autonomous vehicles as it is required to follow a pre-defined path. Different guidance strategies are employed to maintain the vehicle on the path and efficiently reach the waypoints that make up the path. Underwater guidance strategies are often related to the control system because of the maneuvering constraints underwater vehicles can have. The concept of the maneuvering problem [60], [61] defines the problem as a set of two tasks: first, a geometric task, which makes the vehicle stay on and follow the path. And the second task, a dynamic task, requiring the robot to satisfy a speed assignment along the path.

A common guidance approach is to use the Line Of Sight (LOS) guidance laws [62], [63] which provides a convenient description for course and heading control according to the available sensors and desired objectives. A LOS distance is defined and enables the creation of a reference point on the path at the defined distance. When no paths are pre-defined or they are unknown, two-point guidance scheme based laws can be employed. The Pure-Pursuit and Constant-Bearing guidance laws consider the vehicle and the target only. With the former, the goal is simply to align the LOS vector with the course with both pointing towards the target. Compared to Pure Pursuit, the Constant Bearing approach set the course and LOS vectors between the target and its course.

The path following approach is dependant on the type of the path, if it is composed of straight lines or curves. Using a curved path is not practical in many cases as the parametrization of the path must be known in advance. Path following for straight line paths is often resolved using the LOS steering laws which include two main steering principles: enclosure-based steering, and look-ahead-based steering. Both have the same goal, to minimise the cross track error, i.e., the normal to the path. The former consists of defining a circle enclosing the vehicle with a radius large

enough to intersect the path segment. The closest intersection to the next waypoint is selected and the vehicle is set to move towards this point. The look-ahead-based steering is different in the way the course angle is defined. Instead of drawing a circle, a look-ahead distance is defined and used to obtain a velocity-path relative angle which direct the vehicle towards the LOS point. It is added to the path tangential angle to estimate the desired course angle.

These methods are often used with underwater drones and are adapted to specific cases. In [64] and [65] LOS guidance is employed together with an integral action which allows to compensate for the environmental disturbances such as the current, wind, and waves. In [66], [67], experiments were conducted with applications to differently parameterized paths, including curved paths.

Object Detection

To develop perception systems for situational awareness and mapping, processing underwater optical imagery is essential due to the high level of detail in the data and the availability of the sensors, and the recent development of computer vision and machine learning creates opportunities to better understand the underwater world. However, the underwater image degradation due to the light absorption and scattering in seawater introduces challenges and limitations for underwater imaging systems. They inherently create the need for image reconstruction, restoration, and enhancement. The solutions developed to tackle this problem can be divided based on the processing method, either physics-based [68], [69], traditional image processing techniques [68], [70], [71], or deep learning-based [69], [72], [73]. These techniques enable further processing of the images, to better understand and represent the underwater structures, but also for robotic applications relying on optical data during the missions. This is particularly important for visual navigation, object recognition, or semantic segmentation. Most of the models that are used for underwater tasks are based on existing models that prove their efficiency in air. The popular model You Only Look Once (YOLO) [74] is commonly used for detection and classification of marine species and objects [75]–[78], as it offers very good capabilities and background training. The attempts to design models for underwater imagery tend to be focusing on semantic segmentation [79]–[81]. Some of these models include an enhancement step to improve the image.

Learning models are highly dependent on training data to perform well. While in air there is a large variety of openly available datasets [82]–[86] with numerous applications, underwater the data is limited. While the number of datasets for object detection is growing every year [78], [87], [88], the number of annotated dataset for semantic segmentation is very low [80], [89], [90].

1.1.3 Autonomous Ship Hull Inspection

Underwater robotics, navigation, path planning and optical perception for situational awareness have been used and combined to perform autonomous inspections of underwater structures and especially ship hulls. Interest and progress for

autonomous ship hull inspection started in a context of anti-terrorism and force protection, to ensure the ship is not a threat and is not used for smuggling. Early work on acoustic inspection using sonars was done in [91], where the vehicle relied on a high-frequency long baseline system for the navigation. It was suggested in [92] to adopt a hull-relative approach to vehicle navigation and control using a DVL facing the hull. It enabled continuous motion of the vehicle along the hull while keeping it facing the hull at the same time. Navigation along the hull using optical cameras was also studied in [93], where a vision system using a stereo camera is described and used to locate the target surface. A solution for drift-free self-localisation relative to the ship hull using only onboard sensors is proposed in [94]. The drift correction is relying on an imaging sonar which uses a different acoustic lens for the mapping task. An extension of this work is proposed in [95] where more details are given for the inspection of the complex areas of the ship, including the planning and waypoint following methods. A semi-autonomous method is presented in [96], making use of an onshore joystick to adapt the heading of the vehicle and its distance to the hull. This is combined with a waypoint tracking system to follow a vertical lawnmower pattern. In the recent years, the focus has been on visual odometry and optical mapping of ship hulls [97]–[99]. 3D mosaics of the hull are generated to render its texture at the same time as its shape. These enable a more efficient way of observing the hull condition, providing both geometrical information and texture revealing the state of the vessel to the inspector efficiently. Research has also been done on the actual visual detection of defects on the hull [100]–[103]. Although the methods proposed are not all made for detection in an underwater environment and very often tailor made for specific faults, they contributed to the progress of the field by their adaptation to the application.

Navigation and precise localisation, remains the main problem to be solved, and mapping is not always addressed properly. Additionally, not all solutions can autonomously adapt to the type of ship and its shape, which makes human intervention mandatory. To provide an industry relevant end-to-end robotic ship hull inspection solution, the full inspection pipeline should be considered. From the deployment of the vehicle and its access to the ship, to the reporting procedures. With the proper tools and an accredited inspector or service provider in the loop, this would enable consistent, reliable and efficient inspections supported by autonomous solutions.

1.1.4 Functional and Technical Requirements of Hull Inspections

Class societies and ship owners require tests and validations to approve the conditions for safe operations. They comply with the international rules and regulations from organisations such as the International Maritime Organization (IMO) [104] and International Association of Classification Societies (IACS) [105]. The procedures differ according the entity providing the services, but they comply to common categories. During the ship surveys, the class societies verify and evaluate the integrity of the structures and associate them to evaluation categories describing their condition. The American Bureau of Shipping (ABS) [106] provides

a tree-levels grade: good condition, fair condition, and poor condition. Based on data collected from the Det Norske Veritas (DNV) group [107], Registro Italiano Navale (RINA) [108], and ABS, the following categories can be defined for outer hull inspection:

- Overall condition of the coating including cleanliness and corrosion presence.
- Integrity and condition of specific structural points such as anodes, keels, etc.
- Consistency and physical properties of the structure, e.g., plate thickness and hull roughness.

The ship is divided in zones and the surveyor goes through all the class society's specific inspection categories for each zone and is not influenced by the existing inspection scores. The results of the inspection are carefully reported along with the ship's details. Typically, for each inspection finding, a grade is given and briefly explained. Additionally, a risk level and quantitative data is provided together with information like coverage percentage of corrosion in a zone.

For remote underwater inspections using ROVs and magnetic crawlers, the regulations and standards are not clearly defined yet. However, class societies such as RINA and ABS wrote initial guidelines and expressed potential mandatory and optional requirements. When performing the underwater inspection, the data, including high definition images and videos must be reliable and streamed to make it accessible at all time and must comply with the class society's standards and regulations for reporting. The vehicles must be able to operate with strict time constraints to comply with the harbour access time and minimise the operational downtime of the vessel, and be able to detect potential issues with the hull at an early stage. When applicable, the underwater vehicle should clean and measure the hull according to the coating and bio-fouling type and condition. Finally, the vehicle needs to be deploy-able in enclosed and small spaces, and in at least similar environmental conditions as in human inspections. Optionally, the integrated robotic system should support the surveyor in the decision-making and reporting process.

1.1.5 End-to-end robotic inspection systems

In this section, a definition of end-to-end robotic operation is proposed. End-to-end refers to a complete procedure from beginning to conclusion. In robotic operations, the term refers to the complete operation, regardless of the robot's involvement.

An end-to-end robotic solution for technical inspections of infrastructures involves the integration of a robot platform, sensors, navigation solution, data collection and processing, communication, and control technologies and components to enable autonomous or semi-autonomous inspection of infrastructures. For ship hull inspections, this includes the selection of appropriate underwater vehicle and sensors for navigation and data collection to be able to document the status of the ship hull and inspection points such as keels, propellers, anodes and sea chests. For

(a)   **(b)**
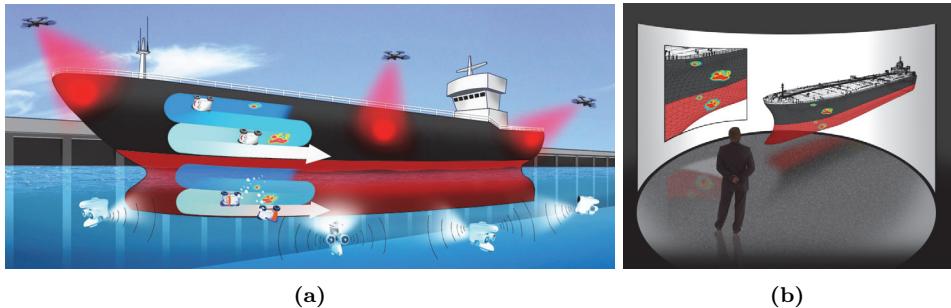
Figure 1.2: The autonomous inspection concept displayed in (a) with all the robotic
fleets working together. In (b) the Virtual Reality (VR) interface with an inspector in it
is pictured.

underwater operations, the system needs to include cameras, lights, and sonars,
both for mapping and for safe operations. Autonomous underwater navigation is
essential for an end-to-end robotic ship hull inspection system. The system will
further need to collect, assess and process data in real-time to provide feature
extraction, anomaly detection and assessment. A reliable communication to both
potential centralised processing and expert interpretation is a central capability
of the system. The data collection and processing will allow automated reporting
improving the efficiency of the inspection process. To reduce the dependence of
skilled operators, the system will also need to have safety mechanisms to ensure
the safety of the robot and the surrounding environment such as obstacle avoid-
ance and emergency stop protocols. Implementing an end-to-end robotic solution
for technical inspections of ship hulls and submerged infrastructures requires a mul-
tidisciplinary approach, combining robotics, sensor technology, data analysis, and
automation to enhance the efficiency and accuracy of infrastructure maintenance
and ensure the safety of critical assets.

An end-to-end robotic inspection platform following the remote inspection guide-
lines from the class societies would significantly increase the efficiency of the ship
hull inspection and would represent considerable progress towards cleaner, more
economical and more environmentally-friendly inspections.

1.1.6   The BugWright2 Project

This PhD project is part of the European project "BugWright2: Autonomous
Robotic Inspection and Maintenance on Ship Hulls and Storage Tanks", co-funded
by the European Union's Horizon 2020 Research and Innovation program under
Grant Agreement No. 871260. It brings together 21 universities and industries from
all over Europe. The project aims at developing an adaptable autonomous robotic
solution for servicing ship outer hulls, including visual inspection, cleaning, and
monitoring. For this purpose multiple robotic fleets are deployed, including Mi-
cro Aerial Vehicles (MAVs), magnetic-wheeled crawlers, and ROVs. A platform
for real-time visualization and decision-support is developed using Virtual Reality

(VR) technologies to enable continuous monitoring and situation awareness. The big picture concept of the project is depicted in Figure 1.2.

This thesis contributes to the BugWright2 project by focusing on and developing an adaptable solution for autonomous underwater inspection of ship hulls. Although only single robot inspection is considered, all the work done is adaptable and can be scaled up to a fleet of ROVs for collaborative missions.

1.2 Scope and Objectives

In this PhD project, new algorithms for efficient navigation and mapping for vessel hull inspection using a small underwater drone were developed. The project also included development of robot in operation/mission, planning, and obstacles perception and avoidance to enhance autonomous operations for ship inspection and includes documenting the ship hull, planning mapping trajectories, planning a coverage pattern, and implementing autonomous behaviours. The project was based on available and low-cost solutions.

The proposed work can be divided into four main Research Directions (RDs): Localisation, Planning and Control, Mapping and Perception, and Mission Planning and Execution. Altogether, they make the autonomous agent enabling the robotic inspection of the hull.

RD.1 Localisation: Localisation is central for an autonomous system as it is key to safe operations and spatial information for all collected data. The vehicle should be able to locate itself in the world's frame as well as relative to the surface being inspected. The localisation methodology should make use of the available on-board sensors to provide accurate pose estimates over time. This should include the navigation sensors as the core sensors, and the perception sensors as aiding sensors.

RD.2 Planing and Control: The ROV should be able to generate and autonomously follow a path to perform the inspection. This includes an online path update mechanism to avoid obstacles or to update the inspection procedure based on the findings. Following the inspection path is not the only case considered, the vehicle should also be able to navigate from the deployment point to the inspection Point of Interests (PoIs), given that the positions are known.

RD.3 Mapping and Perception: The aim is to create a local map for safe and dynamic navigation that can be re-used to keep track of the inspection progress, by monitoring which areas where inspected and which are missing. Local parallel maps of the PoIs should be generated for documentation and reporting purposes. Both acoustic and optic data should be used to obtain accurate and robust estimates along with automated detection of technical findings.

RD.4 Mission Planning and Execution: A mission manager should be developed to keep track of the mission progress, and possibly update it. The manager
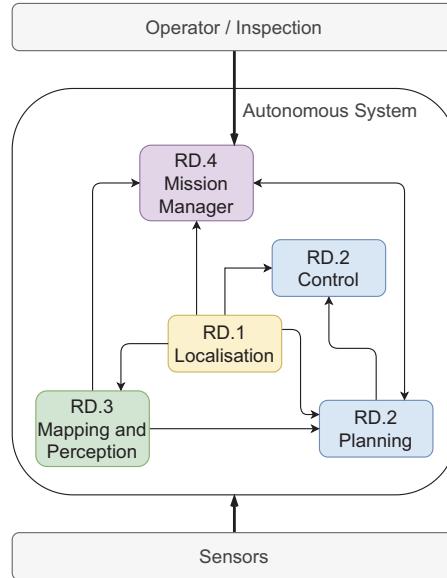
Figure 1.3: The four research directions are represented together with their respective interactions.

also supervises all the sub-modules composing the autonomous agent and ensures they are fully working and interacting with each other. There should be a direct link between the mission manager module and the person in charge, an operator or inspector, who can send manual requests to update the mission.

The research directions are represented as modules in Figure 1.3 and correspond to what was developed during the PhD project with the aim to create a solution towards end-to-end autonomous robotic inspection of underwater outer ship hulls. The autonomy starts at the deployment of the ROV, and ends at the generation of inspection reports complying with the current rules and regulations to be compatible with the class societies' surveys. This also includes the full visual coverage of the hull and the detection of faults. Consequently, with the proposed solution, a surveyor should not need to interact with the robotic platform and inspection findings, except to validate the results. The Figure 1.4 shows how the RDs relate to the end-to-end system and the articles. To enable such a solution, four main objectives are highlighted based on the RDs:

1. Enabling navigation and adaptive path generation independent of prior structure geometry representation to be able to maneuver efficiently and collect relevant inspection data regardless of the ship category. The objective is to perform the relative navigation by leveraging the data from a Forward Looking Sonar (FLS). (Papers B(5.3.2), F(5.3.6), G(5.3.7), I(5.4.2))

2. Detect online PoIs and main hull defects to assist surveys and enable automatic reporting of the inspection findings using deep learning models for
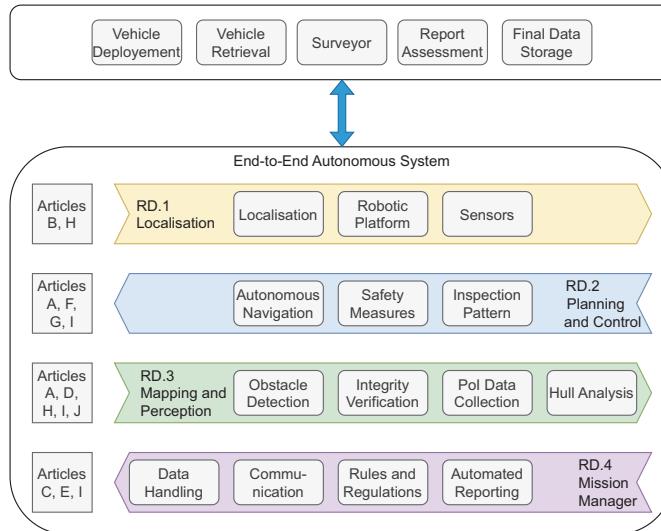
Figure 1.4: The components of the end-to-end system is displayed with respect to the research directions and articles.

monocular imagery for detection and segmentation tasks. (Papers C(5.3.3), J(5.4.3))

3. Combining visual and acoustic data allows to better understand the environment. Using a camera and a FLS, the aim is to generate an accurate and scaled model of the ship's PoIs in real-time, as well as improving the current localisation. (Papers D(5.3.4), H(5.4.1))

4. Industrial third party inspections require to follow guidelines and regulations. Creating solutions that comply with those rules would enable industry efficient monitoring, documentation, and reporting. Therefore, the aim is to suggest a complete inspection pipeline that follows as much as possible the international regulations. (Papers C(5.3.3), I(5.4.2), J(5.4.3))

To establish an end-to-end robotics solution for ship hull inspection, the technical components need to be performing in real-time to produce a coherent result, but parts of the data analysis could be post-processed. The project objective is to run all the proposed and developed solutions for the inspection together to demonstrate the capabilities of a small ROV to perform an end-to-end inspection. This demonstration only includes human intervention to deploy and retrieve the vehicle, and monitor the data. The ROV is given the main dimensions of the ship and inspect one side of the hull to provide full visual and acoustic coverage along with the detected ship parts and associated potential faults. Inspection maps are generated and the PoIs modelled and geo-localised. When the operation is completed, reports are generated and waiting for validation from a accredited expert.

1.3 Approach

Given the main aim of this thesis, the components of the system are tested in separate experiments scaled to a level making the logistics possible to handle, while providing results of high quality. Each research direction is first individually studied and then integrated into the global solution with the objectives in mind. For each new development, a three-steps experiment process is applied. Firstly, methods and algorithms are tested numerically through developed simulations, in order to asses their suitability to the problem. Secondly, using real data collected during field trials, the algorithms are refined and tuned to better match and resolve the problem. And finally, tests in real-time and conditions are conducted at sea to validate the methods.

Close collaborations with service providers and shipyards were setup to enable a continuous discussion of the needs and problems faced by experts. This opportunity made it possible to considerably improve the performance of the developed solution and to make it an attractive solution for the domain experts. Access to a mock-up and full scaled ships were provided to enable real case inspection scenarios. This includes Ro-Ro cruise ferries of the Perama shipyard, near Athens in Greece, lake boats and ferries of the Wörthersee lake, in Klagenfurt, Austria, research vessels of the Univerity of Porto, Portugal, warships of the Portuguese Navy in the Lisbon Naval Base, Portugal, and the research vessels and facilities of NTNU.

1.4 Contributions

This thesis contributes towards autonomous robotic operations for underwater ship hull inspections. For each research objective, the following main contributions are proposed:

1. Objective 1: Efficiently navigate along the ship hull

    - A collision-free and and adaptive coverage path planning framework is developed leveraging the knowledge of the onboard sensor coverage capabilities. Over time, the lawnmower-based coverage pattern adopts the shape of the structure being inspected without prior knowledge of its geometry.

    - A maneuvering-based guidance strategy is developed with online adaptation and constraints for inspection operations. It is designed for high precision low-speed path following while accounting for inspection errors.

    - Sonar processing is performed for hull relative navigation based on estimations of the relative orientation and distance to the hull. For this, an acoustic line is robustly and continuously detected in the sonar imagery using the assumption of a local flat surface.

2. Objective 2: Detection of ship parts and faults

- The first dataset dedicated to underwater ship hull inspection containing labelled data of ship parts and faults is developed and made openly available.
- The labels were decided in cooperation with domain experts to make the dataset industry and scientific relevant. Additionally, the data and results were verified by the experts.
- A benchmark including quantitative and qualitative evaluations was performed to measure the capabilities of State Of The Art (SOTA) models on such a dataset. This also helped identify models suited for real-time detection and semantic segmentation tasks.

3. Objective 3: Ship parts modelling

- An integrated feature-based acoustic and visual combination using a monocular camera and a FLS is developed with a SLAM framework. This is done by estimating the areas where the sonar beams intersect the camera image plane and enables to augment the visual SLAM framework with robust acoustic features.
- The visual-acoustic correspondence mechanism enables to continuously re-scale and verify the estimated trajectory and point cloud. A depth ration is estimated and optimised over time to provide scale stability and drift correction.
- The combination allows to more accurately model the ship parts by obtaining a denser point cloud and realistic surface reconstruction with incremental estimations and reconstruction.

4. Objective 4: Compatibility with international regulations

- The relevant rules and guidelines for remote inspection operations from the international organisations and class societies are identified in the context of autonomous underwater robotic inspection of outer ship hull.
- The solutions developed are compatible with the international regulations and were discussed with domain experts to ensure their industrial relevance.
- An acoustic inspection map is generated in real-time to enable efficient monitoring of the mission. The sonar imagery is processed to obtain a dense point cloud discretised into a voxel map representing the inspected areas. Uncertainty estimation is embedded into the map for further understanding of the inspection quality.
- Reports are automatically generated at the end of the robotic operation. They include the inspection findings and post-processed meta-data to support the decision making of the surveyor in charge.

1.5 Thesis Structure

This thesis is divided in five chapters. Chapter 1 provides an overall introduction to underwater ship hull inspection and how is this thesis contributing to it. This is followed by a presentation of the project settings in Chapter 2, including the

robotic platform and the sensors. The actual inspection methodology is then presented in Chapter 3, along with what can be achieved with the proposed solutions. A discussion of how the methods can adapt and scale to other underwater problems is proposed in Chapter 4. And finally, Chapter 5 contains the remarks and conclusions.

Chapter 2

Vehicle and Sensor Settings

This chapter presents the equipment used in the project. First the robotic platform is described followed by the on-board sensors used for navigation and by the sensors used for the perception of the underwater environment.

2.1 Low-Cost ROV

The two most common categories of underwater vehicles are Autonomous Underwater Vehicles (AUVs) and ROVs. An AUV is untethered and operates without real-time communication with an operator, whereas an ROV is physically connected to the operator on the surface. The objective of the PhD project is to develop systems capable of autonomous missions with minimum interaction from an operator. But to provide real-time data access for data monitoring and processing, the proposed system is based on an ROV. To provide cost effective logistics and access to confined volumes to comply with the regulations from the class societies, a small and energy efficient vehicle is used.

A Blueye X3 ROV was configured for the underwater tasks of BugWright2 and used throughout the project. It is produced by Blueye Robotics [109], and is a small low-cost vehicle with high maneuvering capabilities, see Figure 2.1. The platform is actuated in four Degrees of Freedom (DoFs), surge, sway, heave, and yaw. The buoyancy is slightly positive, and for roll and pitch, the righting moment provides passive stability. The characteristics of the vehicle enable quick and easy deployments in any environments, including enclosed spaces, and its maneuvering capabilities allow it to navigate efficiently. The capacity for external equipment allows up to three sensors with real-time communication. The ROV is connected to a network router located above water with a 225 meters long tether. The operator laptop connected to the router contains an Intel Core i7 vPRO CPU and 16GB RAM. The onboard computational operations are limited by the vehicle IMX6 processor, which is equivalent to a Raspberry Pi 3 Model B [110]. For that reason, all processing related to navigation, including localisation, planing and control, is done onboard, whereas the tasks related to perception and Computer Vision (CV),
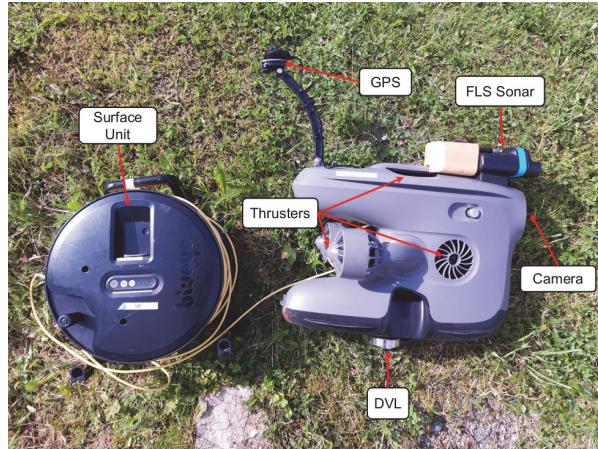
Figure 2.1: The Blueye X3 ROV used for the experiments is displayed with the list of apparent equipped sensors.

are done on a topside laptop. The robotic middleware Robotic Operating System (ROS) is used to facilitate data communication and management.

2.2 Navigation Sensors

The Blueye ROV is equipped with two Inertial Measurement Units (IMUs) and magnetometers to obtain the attitude of the vehicle, and a pressure sensor to estimate its depth. Additionally, a small and low-cost DVL was added. The Water Linked A50 was mounted on the ROV. The DVL provides velocities and attitude measurements. As the vehicle is small and lightweight, the instrument needs to nimble. The ROV is deployed in harbor-like areas, usually with shallow and flat sea floor depth, making the selected DVL a good choice. This sensor enables the ROV to locate itself in a local reference frame, but it also needs global reference. An USBL system was tested, but performed poorly because of the acoustic shadows and multi-paths in the harbour environment, especially when operating close to the ship hulls. Therefore, it was replaced by a standard Global Navigation Satellite System (GNSS) to obtain the position in the global reference while the drone is at the water surface. A list of all the navigation sensors on the ROV is provided in Table 2.1 along with their details.

Table 2.1: Navigation sensor list and details

Sensor	Rate (Hz)	Details
IMU	100.0	Acceleration readings
Magnetometer	100.0	Direction readings
DVL	5.0	Velocities and attitude
Pressure	45.0	Depth
GNSS	1.0	Global position

This combination of sensors enables precise localisation for the duration of the mission, given that the sensors were correctly calibrated prior to deployment. Longer missions would require better sensors due to the drift of dead-reckoning, but they are also more expansive. However, the solutions developed within this thesis are re-usable and can be configured for a different ROV and navigation sensor suite.

2.3   Perception Sensors

There are two types of perception sensors used to observe the environment on the vehicle in this project: an integrated camera in the ROV, providing optical data, and a Multi Beam Forward Looking Sonar (MBFLS) that provides acoustic data. Although cameras are cheaper than sonars, sonars bring data essential for inspection tasks, and not accessible by cameras. The Oculus M750d multibeam sonar was selected based a trade-off between quality, price, and ease of use. The details of both perception sensors are given in Table 2.2. The resolution corresponds to the image resolution of the sensor outputs. In the case of the sonar, it is an acoustic image formed after the processing of each acoustic beam and ping.

Table 2.2: Perception sensor list and details

Sensor	Rate (Hz)	Resolution (px)	Details
Camera	25.0	1080×720	Optic data
MBFLS	10.0	256×405	Acoustic data

The camera has a Field-of-View (FoV) of $\sim 48°$ vertically and $\sim 77°$ horizontally. It was calibrated underwater with a checkerboard and using the pinhole model. This model allows to formulate the 2D-3D correspondence as

$$p = \frac{P}{P_z} K, \tag{2.1}$$

where P is the 3D point in the world converted to p, the 2D point in the image. The intrinsic matrix of the camera used, K, is defined as

$$K = \begin{pmatrix} f_x & 0 & c_u \\ 0 & f_y & c_v \\ 0 & 0 & 1 \end{pmatrix}, \tag{2.2}$$

with the pixel coordinates of the optical centre of the camera represented by (c_u, c_v), and the focal length described by (f_x, f_y).

The sonar on the other hand has an horizontal aperture of $130°$ and $20°$ vertically. The system emits acoustic beams in a fan shaped pattern, and each beam has a fixed vertical opening angle. When the echo reaches a target, it bounces back to the
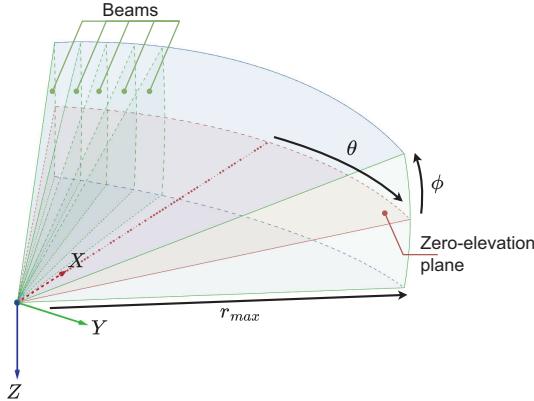
Figure 2.2: The FLS footprint is represented in a 3D space with the corresponding geometry. All the elevation planes between the minimum (green) and maximum (blue) elevation planes are merged into the zero-elevation plane (orange) after the processing of the measurements. A beam i (green) is also represented, going through all the elevation planes. [8]

sonar which measures the signal strength and time difference between the signal emission and its reception. The target range is calculated using the time-of-flight for the signal combined with knowledge of the speed of sound in water, and the horizontal bearing angle is given for each beam by the beamformer of the sonar. The vertical angle remains ambiguous as it cannot be derived by the sonar.

In this thesis, the acoustic images from the sonar are referred to as scans. A scan is an acoustic array describing features in the spherical coordinate system $[\theta, \phi, r]^\top$, where the columns are azimuth angles θ and rows, ranges r. The elevation angles ϕ are unknown and merged into one zero-elevation plane. The geometry for the sonar set up is described in Figure 2.2. The features in spherical coordinates can be converted to Cartesian coordinates using the following transformation,

$$
P = \begin{bmatrix} P_x \\ P_y \\ P_z \end{bmatrix} = r \begin{bmatrix} \cos\phi \cos\theta \\ \cos\phi \sin\theta \\ \sin\phi \end{bmatrix} . \tag{2.3}
$$

The employed MBFLS has two frequency operating modes, 750 kHz and 1,2 MHz. Only the high frequency configuration, enabling higher acoustic precision, was used in the experiments in this thesis. A setup with low gain and constant range of 4 meters was applied since the vehicle was expected to operate close to the inspection targets.

The sonar and camera were horizontally aligned with a small measured vertical offset. They were pointing towards the same direction. Both sensor footprints are represented in Figure 2.3, with the vehicle in front of a simulated ship.
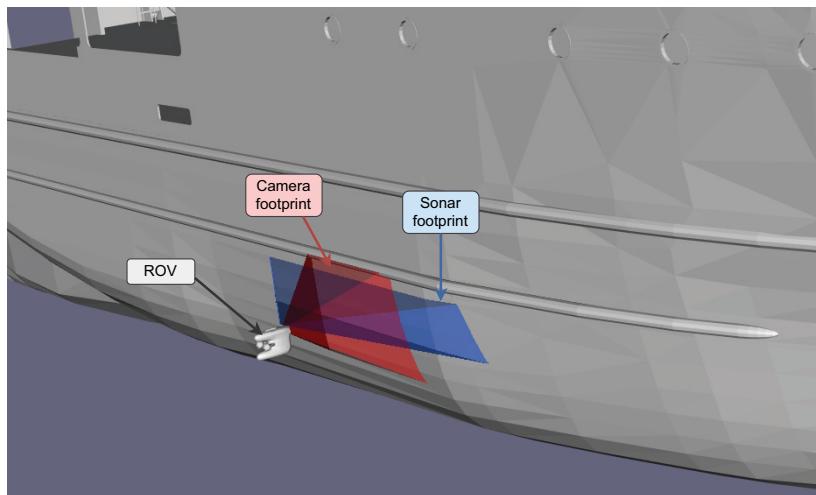
Figure 2.3: The footprints of the camera and sonar are represented, with the vehicle facing a ship hull.

Chapter 3

Ship Hull Inspection

In this chapter, the robotic inspection is discussed, including the data processing and analysis. The setup for data processing, transfer, and sharing is first presented in Section 3.1. The methods to make the data acquisition and analysis autonomous are discussed and described in Section 3.2. The robotic perception methods to obtain a better understanding of the inspection progress and the ship condition are laid out in Section 3.3. Finally, the data post processing and reporting algorithms based on the accepted inspection regulation guidelines, are discussed in Section 3.4.

3.1 Data Communication Setup

The robotic system includes a specific communication system to ensure reliable data transfer within the network shared in the operation. This is essential to enable a shared workload among the connected devices using the previously described router connected to the underwater vehicle. The router is connected to the operator's laptop through ethernet instead of WiFi to obtain a more reliable and faster connection. This makes up the basic communication network, but it has capacity for more devices.

To efficiently share the workload among the connected devices, a top-down multi-layer architecture following a publish-subscribe model is defined [5]. The architecture makes it possible to specify the inputs and outputs for each layer and avoid over-communication of data. A visual representation of the architecture is presented in Figure 3.1, including the underwater unit as the ROV, the surface unit as the operator's laptop, and the external unit as any other devices connected. The latter can be another laptop physically present on site, or a cloud server, enabling the processing of computationally expensive data.

The transmitted messages are divided into two categories: small and large messages. The WebSocket protocol is used for messages of small size, whereas the Real-Time Streaming Protocol (RTSP) is employed for larger messages, typically multimedia messages such as videos and sounds, corresponding to the camera and sonar streams
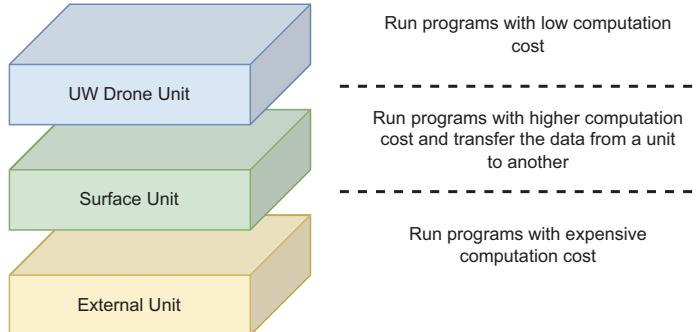
Figure 3.1: Representation of the multi-layer architecture including three processing devices.

in this project.

This architecture was deployed when it was necessary to compute additional data or when more advanced results were required quickly, e.g. textured surface reconstruction of sections of the ship, or object detection using deep learning models.

3.2 Inspection Strategy

3.2.1 Mission and Path Planning

To start the inspection operation, the location of the ship must be known, and the inspection vehicle ready in the water. When the ROV is deployed close to the ship, it can move directly towards the vessel and start the inspection. However, if the vehicle is deployed in the inspection area with obstacles on the way, the underwater drone must plan collision free paths to manoeuvre safely. For this purpose, the Parameterized Rapidly-exploring Random Graph (PRRG) framework is employed [7] to identify collision-free paths and plan inspection routes with optimised sensor coverage. The framework generates a planning graph using the same concepts as the RRT method [45], but includes interconnecting nodes to create a graph instead of tree. It is designed for safe and dynamic navigation in multi-dimensional bounded environments. To define a path within the planning graph, a planner must be setup, such as the Dijkstra algorithm [42]. To more efficiently handle obstacles discovered online, the D* Lite planner [111] is employed with the proposed PRRG. A real case example is depicted in Figure 3.2, using data collected during a field trial in a harbor. The ROV had to plan a collision-free path from the blue cell to the green cell, where a ship to inspect could be. The sonar was used to detect the obstacles and update the map to reach safely the end of the path.

The path P for the vehicle is composed of n waypoints WP,

$$P = [WP_0, WP_1, WP_2, ..., WP_n], \qquad (3.1)$$
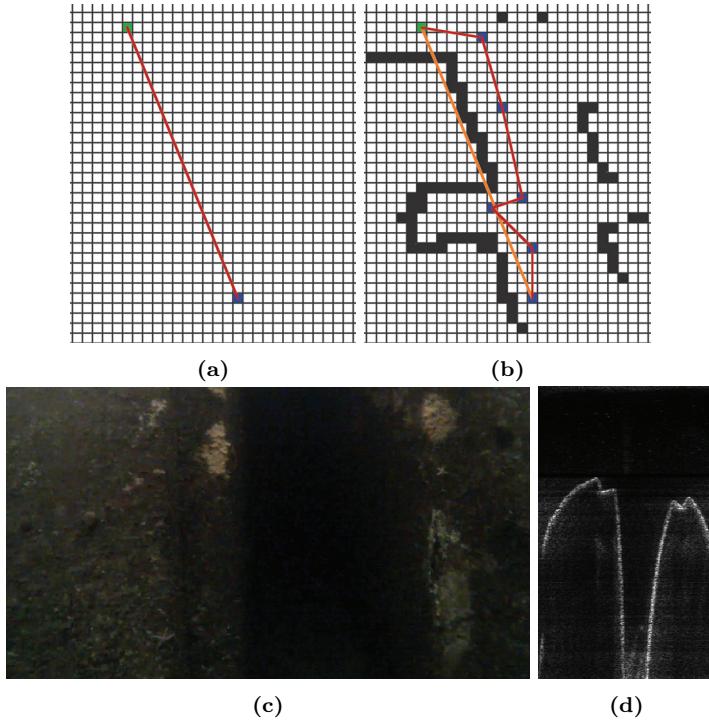
Figure 3.2: The top-down 2D map of the local area is displayed. The blue cell is the deployment point, the green cell is the goal point, and the red segments is the path. (a) is the initial map, without any obstacles discovered. In (b) the path is updated along the way to avoid the obstacles detected using the sonar data. The image and sonar scan of the discovered cavity in the wall are shown in (c) and (d).

and it can be divided in two parts. The path the vehicle has to follow to reach the vessel is referred to as the transit path, while the path followed to perform this inspection is the inspection path. Once the ROV has reached the end of the transit path, it switches to the inspection path which includes maneuvering constraints required to perform the inspection. The vehicle has to move along the hull while facing it at a constant distance. The inspection path is generated in parallel to the planning graph and consists of a time adaptive vertical lawnmower pattern dividing the inspection area in vertical or horizontal slices depending on the orientation of the path segments. The camera coverage is taken into account for the path planning to ensure full visual coverage and overlapping slices. Both cases are simulated in Figure 3.3.

The planning graph has a dynamic update mechanism to adapt to the changing perception of the scenery. Constraints can be applied to each node in the planning graph in real-time to deactivate or re-activate specific nodes based on the mission objective or environmental data. Nodes can also be resampled with a different resolution throughout the coverage area of the graph. This enables objective oriented

(a)

(b)

(c)
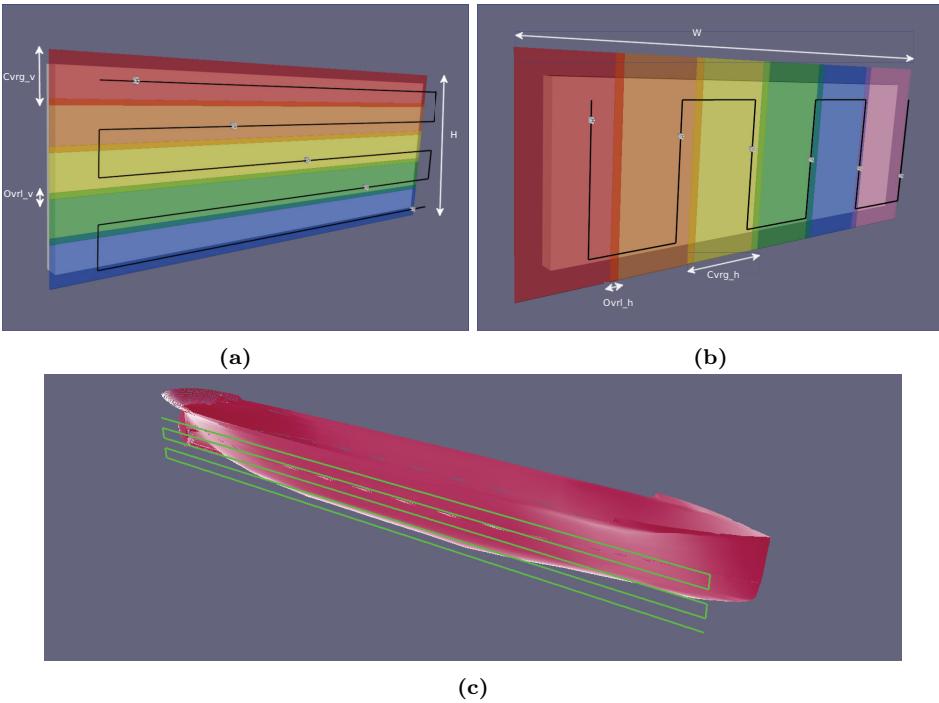
Figure 3.3: The reference patterns for the inspection are generated given the coverage capabilities of the camera, a width, a height, and a desired overlapping area. Horizontal slices are generated in (a), whereas in (b), vertical slices are provided. In (c), a pattern is generated given the ship dimensions and placed in front it.
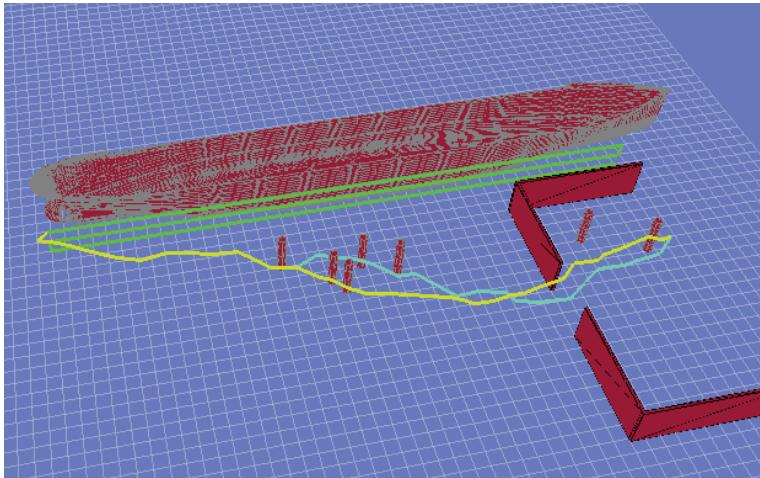
Figure 3.4: The path planning framework is tested in a simulated harbor environment. The ROV needs to go to the start of the inspection route which is on the top left of the green pattern. A first path is generated (blue), but considered not safe enough, therefore, a new one is computed (yellow), avoiding to go through the obstacles.

planning and prevent potential risks during the operation. For example, nodes in the proximity to obstacles discovered while operating the ROV in a harbour are automatically deactivated to avoid entanglement with the vehicle's cable. Such a scenario is presented in Figure 3.4 in a simulated environment.

3.2.2 Localisation

To track the 6DoF pose of the vehicle while in water, the Modular and Robust Sensor-fusion (MaRS) framework [2], [112] was utilized. It consists of a modular EKF which can perform online extrinsic sensor calibration and can handle sensor outages and measurement outliers. The navigation sensors are combined in a Kalman filter to estimate the vehicle's position, its attitude, velocity, and angular velocity and acceleration biases. The gravity vector together with the compass and the GNSS measurements are used to initialise the pose of the ROV. It is done while the drone is still at the water surface and away from the surrounding structures, to avoid magnetic disturbances in the measurements.

3.2.3 Guidance Strategies

The vehicle's pose information is not enough to navigate reliably along the hull for the inspection. Indeed, the hull geometry and its exact position would need to be known and the vehicle equipped with a drift free localisation system. Therefore, an additional sensor is required to ensure tracking of the hull to remain close to it and avoid collisions while mapping the structure. For this project, a MBFLS is used to measure distance and orientation of the vehicle relative to the hull. Only a line is expected to be seen in the sonar scan, as the local shape of the hull is close to flat and the operating range is low.

To detect and extract the line from the scan, a method based on Random Sample Consensus (RANSAC) [113] is proposed. A comparison of line detection methods is provided in [114], and identifies RANSAC based methods as advantageous when outliers are expected. Only good inliers are considered, which enables precise line estimation as opposed to maximizing the number of data points. To make sure the inliers provided by RANSAC contributes to the best hull line estimate, the sonar scans are pre-processed. First, a threshold operation is performed to keep only the features that potentially hold important information. This corresponds to keeping only the pixels of the scan with intensity between T_{low} and T_{high}. The Canny edge detector [115] is then applied in order to sparsify the data, and consequently remove the dense areas that can bias the line detector. This results in a better distribution of the features along the line. In Figure 3.5, a raw sonar scan is displayed along with the final result after detecting the line.

To place the hull in the ROV's reference frame, two values are extracted from the detected line. The first value is the 2D line inclination α_l, which is to the angle between the local section of the hull and the normal of the line of sight of the vehicle. The second value is the forward distance d_w, the vertical distance to the center of the line in the 2D image, physically corresponding to the distance from

(a)   **(b)**
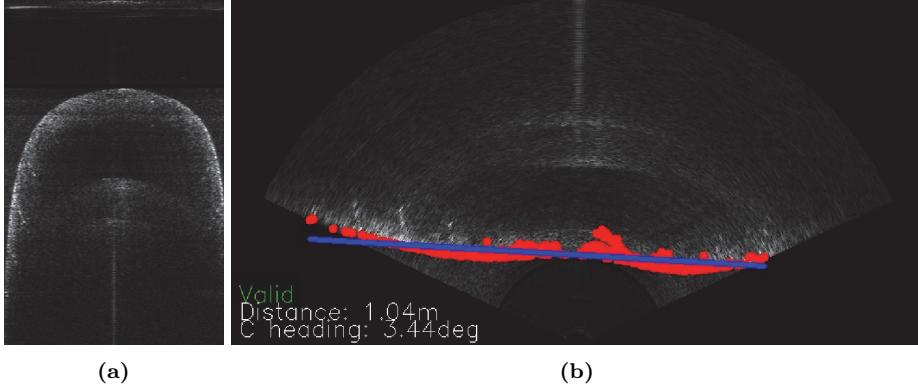
Figure 3.5: The original sonar scan is presented in (a), taken when the ROV was facing the hull. The scan is processed and converted to Cartesian coordinate in (b), where the extracted features are displayed in red, and the detected line in blue. In this case, a relative heading offset of 3.44 degrees and forward distance of 1.04 meters were estimated.

the ROV to the wall. With these two values, it is possible to place in the 3D space any points w_k representing the hull locally. They are given by

$$
w_k = \begin{bmatrix} w_{k,x} \\ w_{k,y} \\ w_{k,z} \end{bmatrix} = p + d_w \begin{bmatrix} \cos\left(\psi\right) \\ \sin\left(\psi\right) \\ 0 \end{bmatrix} \pm c_k \begin{bmatrix} \cos\left(\psi - \alpha_l + \frac{\pi}{2}\right) \\ \sin\left(\psi - \alpha_l + \frac{\pi}{2}\right) \\ 0 \end{bmatrix}, \tag{3.2}
$$

where $p \in \mathbb{R}^3$ is the vehicle's position, ψ, its heading, and $c_k \geq 0$ an arbitrary constant representing the distance to the wall's local origin, i.e., where the vehicle's line of sight hits the hull.

Because the hull is considered flat only locally, the path needs to be continuously updated to adapt to the global curvature of the hull. To achieve this, the current path segment is translated and rotated to keep the vehicle facing the hull at a constant distance. A new path segment is positioned parallel to the estimated line representing the hull and at a desired distance d_d from it. The geometry involved in the path update mechanism is explained and depicted in Figure 3.6. The path update is done online for each new sonar measurement and over time, with a constant distance, the inspection pattern should adopt the actual shape of the hull.

For the vehicle to maneuver efficiently, a specific guidance strategy is adopted and depends on the type of path the drone is following, transit or inspection. For the former, the employed method [6] is based on the LOS steering laws for straight line following [63], [116]. The look-ahead distance $\Delta(y_e)$ is time-varying depending on the cross-track error y_e. It is especially effective for avoiding oscillatory and aggressive motions as it smooths out the steering [117]. Additionally, to compensate
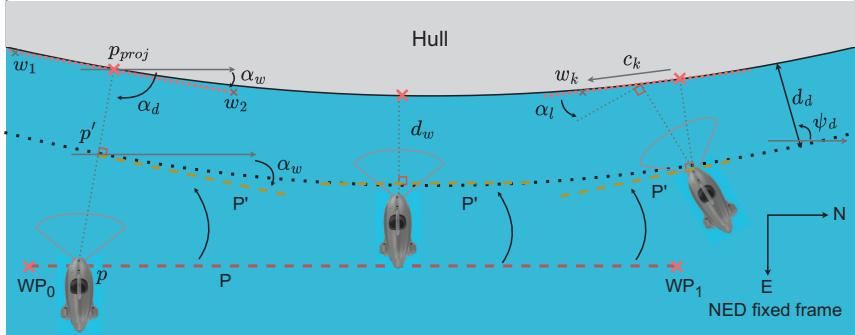
Figure 3.6: The original path segment P (red) is continuously updated to create a new one P' (yellow) solving locally the inspection constraints. To position correctly P', the vehicle's position is projected on the wall, p_{proj}, and the point p' is sampled on the projection line at the distance d_d from the local wall. Given the orientation of the new path segment α_w, estimated from α_l, the waypoints can be re-positioned. [9]

for external disturbances, an integral action is applied when the desired heading ψ_d is estimated [118]. It is given by

$$\psi_d = \gamma_p - \text{atan2}\left(y_e + \kappa y_{int},\ \Delta(y_e)\right) \tag{3.3}$$

$$\dot{y}_{int} = \frac{U y_e}{\sqrt{\Delta(y_e)^2 + (y_e + \kappa y_{int})^2}}, \tag{3.4}$$

where γ_p is the horizontal path-tangential angle, $\kappa > 0$, the tuning parameter of the integral action, and U, the ROV's total velocity.

To follow the inspection pattern, maneuvering-based guidance [60], [61] is used instead. It enables more precise control in slow speed, which is important when inspecting structures. The desired speed along the path is defined to account for the inspection constraints and errors that can occur, such as heading and depth errors. To make sure the vehicle reaches the waypoints and is always converging towards the path segment while maintaining its velocity, the constant bearing nonlinear approach [119] is utilized. Therefore, the desired velocity ν_d is defined by

$$\nu_d = p_d^s v_s - U_p \frac{e_1}{\sqrt{|e_1|^2 + \Delta_1^2}}, \tag{3.5}$$

and the component dependent of the position error $e_1 = p - p_d(s)$ is included and calculated from the 2D position of the vehicle p and its desired position p_d. This error is controlled with the tuning parameter $\Delta_1 > 0$, and $U_p > 0$ is the approach speed, corresponding to how rapidly the vehicle should converge to the current path segment. Finally, $v_s(s, t) \in \mathbb{R}^2$ for $\dot{s}$, is the speed assignment along
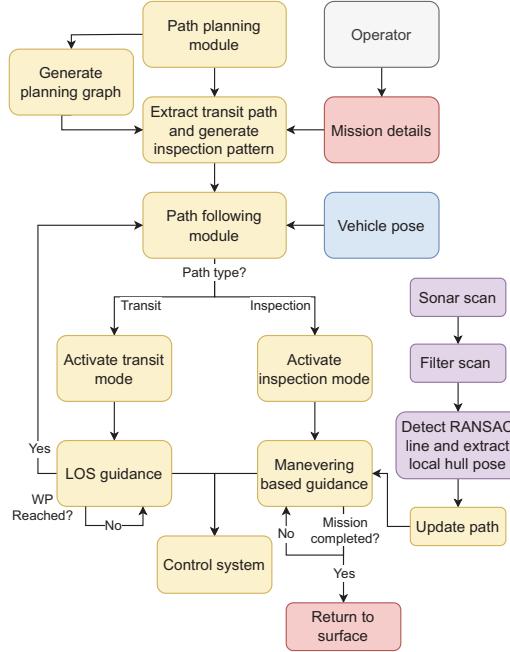
Figure 3.7: The stateflow diagram of the hull inspection operation and how the different modules, including planning, guidance and control, interact with each other.

the path with the path variable $s \in [0, n)$ which represents the global progression on the path for n waypoints. It consists of a manually set desired speed $u_d(t) > 0$ and a modifier $u_s(s) > 0$ to make sure the vehicle slows down at the waypoints. $p_d^s(s) = WP_i - WP_{i-1}$ describes the current path segment being followed and $||p_d^s(s)||$ its norm. The speed assignment

$$v_s(s, t, \epsilon_\psi, \epsilon_z) = \sigma_{\delta_\psi}(\epsilon_\psi)\sigma_{\delta_z}(\epsilon_z)\frac{u_s(s)}{||p_d^s(s)||}u_d(t), \tag{3.6}$$

is further modified using the ratios $\sigma_{\delta_\psi}(\epsilon_\psi)$ and $\sigma_{\delta_z}(\epsilon_z)$ which regulate the motions along the path according to the heading ϵ_ψ and depth ϵ_z errors when these grow too large.

The outputs from both guidance systems are then used as inputs to control the 4DoF of the vehicle. For this Proportional Integral Derivative (PID) controllers are setup.

The complete stateflow of the operation is depicted in Figure 3.7. It starts with the operator sending the mission details and ends with the vehicle returning to the surface when the operation is done. The ROV plans the transit and inspection when the mission details are received, and starts the mission execution. When the
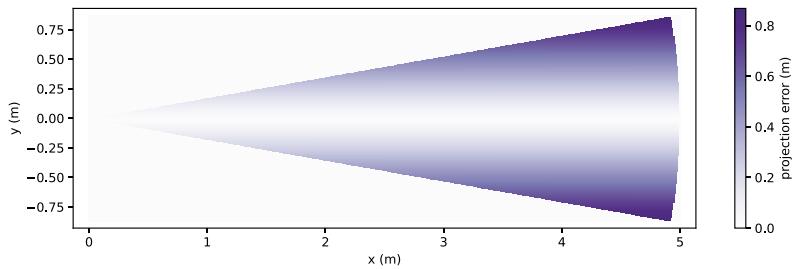
Figure 3.8: The reprojection error of the acoustic features projected onto the zero-elevation plane of the sonar is displayed as shades of purple. The figure includes an acoustic coverage of up to 5 meters and 20° vertical aperture.

vehicle has arrived close to the hull, the guidance strategy is updated to make use of the sonar measurements and move efficiently along the hull to collect inspection data. This concise stateflow enables consistency in the behavior of the underwater vehicle and makes it easy to track its current state. This is because the states and conditions are kept simple and deterministic, and the links are minimised. The operator can interact with the ROV while the autonomous mission is on-going. This can occur for multiple reasons. In a harbor, parallel activities might require the inspection mission to stop for a moment for safety concerns. The operator can then request the vehicle to pause and maintain its position, or to go to the seabed to make sure the ROV umbilical is out of the way for other vehicles. To obtain further details about a specific area of the hull, the operator can also send a request to the vehicle to collect complementary visual data. The position of the ROV is saved when a new request is sent to restart the original mission plan at a later point in time. When the operation is complete, the vehicle returns to the surface and holds its position, awaiting further instructions. When the inspection is complete, the vehicle is retrieved from the same location it was deployed.

3.3 Mapping and Monitoring

3.3.1 Acoustic Map Generation

To enable real-time monitoring of the condition of the ship hull, a real-time data stream is established with odometry, acoustic, and optic data, which is the essential data required to assess the operation. An inspection map is incrementally built as the operation is on-going, enabling the tracking of the inspection progress and covered areas. The map consists of a 3D acoustic model of the hull, downsampled to a voxelised grid.

The inspection map is generated from the MBFLS data, using the assumption of the ship hull being locally flat. This means the closest acoustic feature for each beam on the sonar scan can be placed on the zero-elevation plane of the sonar, i.e., at the same depth as the vehicle and accounting for the vertical offset. Given that the operating range of the sonar is setup to four meters, the maximum reprojection

33

(a)

(b)

(c)

(d)

(e)
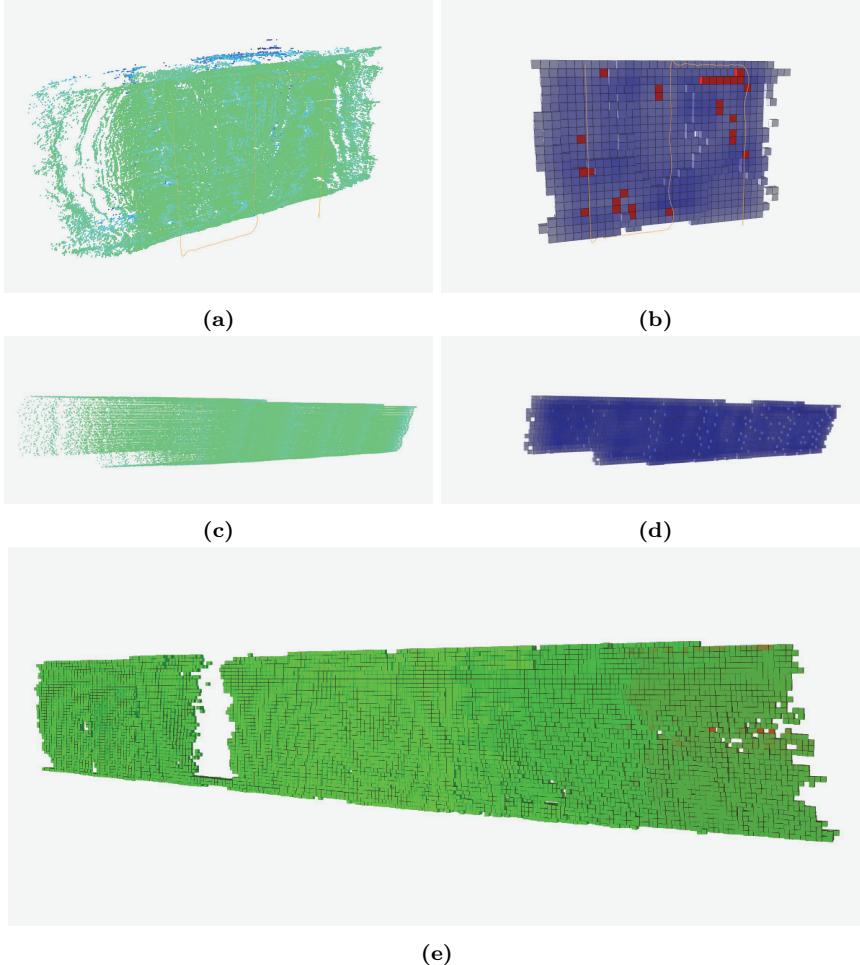
Figure 3.9: The occupancy maps from three inspection scenarios are presented. (a) and (b) are respectively the dense point cloud and its equivalent voxel map of a harbor wall. (c), (d), and (e) are ship hulls. To obtain these results, the vehicle followed an inspection pattern with vertical slices.

error on the zero-elevation plane is ~ 0.69m, considering an elevation of 10° and a range of 4 meters. This error corresponds to the distance between the actual point and the intersection between the corresponding circle arc and the zero-elevation plane. However, since during the inspection the ROV is typically at a distance of one meter to the hull, the maximum reprojection error becomes ~ 0.17m. Additionally, because the shape of the hull is locally flat, the closest features on the scan are very likely to be on the zero-elevation plane, resulting in a reprojection error very close to 0. This enables surface reconstruction of the ship using the acoustic scans and considering the zero-elevation plane only. Figure 3.8 displays the reprojection error according to the feature locations, the further away a point is from the sonar

and its zero-elevation plane, the greater the magnitude.

In the first step of the 3D map generation, the sonar scan is pre-processed with Gaussian and thresholding operations to reduce the visible noise, and the closest feature is extracted for each beam. This limits the data redundancy and the reprojection error. However, there can still remain residual noise in the data due to the environment and direct projection onto the zero-elevation plane, creating outliers and biasing the map generation. Bin based methods can be used to efficiently remove the outliers, by using the measured acoustic distances to the detected point and applying threshold operations within the bins [120]. To avoid true positive rejections, filtering points using a virtual moving window and averaging the valid data points will verify the integrity of the central point, and biases related to the geometry of the scene will be vanished.

The remaining reliable points are converted to 3D points and placed in the ROV's reference frame. A voxel is created if the volume contains enough points according to the grid resolution. The resolution must be set carefully and according to the sensors characteristics [121] and mission objectives. Since the inspection map is utilised for path planning and monitoring purposes, a grid with high resolution is not required but should be high enough to represent the geometry of the hull to avoid collisions and be able to observe the currently covered areas by the vehicle. Over time, a dense point cloud is generated and converted into a complete inspection map that the inspector can refer to and the vehicle can use for scene understanding. Figure 3.9 provides representative dense point clouds of structures and their corresponding inspection maps from experiments carried out in this project.

Each voxel contains uncertainty information in addition to the geometric information. The uncertainty is estimated from two separate sources, the acoustic features reliability, and the drone's pose reliability. The EKF employed to obtain the pose of the ROV includes a state covariance matrix $K_{x_{core}}$ of the drone's core state x_{core} with k core components included in the matrix [2]. It is reduced to a single value describing the point variance, or location precision [122], [123]. To achieve this, an 1-homogeneous function S with a normalization constraint [124] is defined such that

$$S(K_{x_{core}}) = \frac{\text{trace}\,(K_{x_{core}})}{k}.$$

(3.7)

To express the uncertainty from the sonar, the averaged distance values $\bar{d}^f$ from the previous sliding window are reused and fitted to a Gamma probability distribution. Its variance represents the sonar uncertainty and is computed from an estimated true mean $\mu_{\bar{d}^{f^T}}$ given a sonar scan and a detected line. To achieve this, an estimated true set of distance values is generated, corresponding to how the data should ideally look like given the current estimation of the hull's orientation, and the sliding window is passed through this new set to create new averaged distances $\bar{d}^{f^T}$. The variance of the original set $\bar{d}^f$ becomes

$$\mathrm{var}(\bar{d}^f) = \frac{1}{n} \sum_i^n \left(\bar{d}_i^f - \mu_{\bar{d}^{fT}} \right)^2.$$

(3.8)

The uncertainty for the sonar data is expressed per acoustic feature whereas the uncertainty for the pose of the vehicle is calculated for each new sonar scan. To represent both together as a single value, the total uncertainty u is obtained from a weighted sum to emphasise or minimise specific sources, that is,

$$u = S(\sigma_{\mathrm{x}_{core}} \mathrm{K}_{\mathrm{x}_{core}}) + \sigma_{\bar{d}^f} \mathrm{var}(\bar{d}^f),$$

(3.9)

where $\sigma_{\mathrm{x}_{core}} \in \mathbb{R}^{k,+}$ and $\sigma_{\bar{d}^f} \in \mathbb{R}^+$ are the weights.

Making the uncertainty estimates available to the inspector enables a new dimension of scene understanding which can lead to requests for re-inspection of regions with very high uncertainty to ensure good quality data is collected. The uncertainty can also indicate lack of instrument and software integrity.

3.3.2 Camera-Sonar Combination For PoI mapping

For hull inspection, PoIs represent geometrically complex sections and hull features. Here the sonar can not be used as the main perception sensor using the previous method since the assumption of a flat surface does not hold anymore. Also, the monocular camera can not be used alone since it cannot estimate the scale of a scene. Therefore, to enable an efficient visual representation of the PoIs, the sonar is combined with the monocular camera. The combination occurs in the SLAM framework ORB-SLAM3 [33] where the visual odometry and point cloud are made more robust and correctly rescaled. This is especially important for situational awareness and for the inspector to assess the structure integrity and potential deformations.

The camera images are first pre-processed to obtain images that are more robust to the underwater environment before they are combined with the acoustic data. The lack of contrast, due to the light attenuation, and to the underwater particles, also called marine snow is compensated in the process. The contrast is corrected using Contrast Limited Adaptive Histogram Equalisation (CLAHE), and the marine snow using a tailor made filter [4]. First, the previous and next frames are selected and the luminance component of the three images are extracted after converting them to the YCbCr color space. A first set of feature candidates is selected after applying a guided filter [125], [126] to retain the high frequency information of the images. Finally, convolution operations with an uniform kernel are performed on the previous and next image before they are compared to the current image to decide which pixels correspond to unwanted underwater particles. From this marine snow filter, masks are generated, corresponding to where in the image visual features should not be sampled.
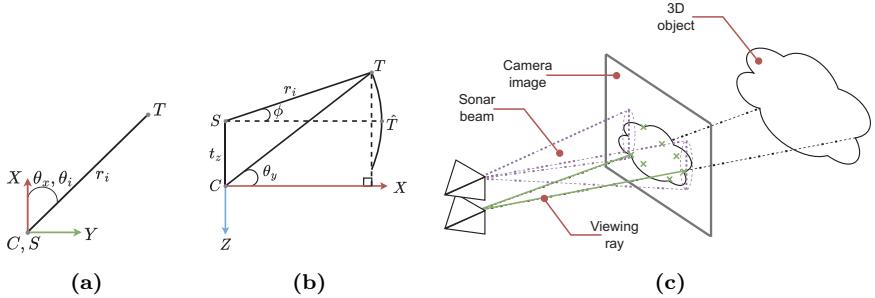
Figure 3.10: The correspondence and matching mechanisms are illustrated in this figure. (a) and (b) are respectively a top-down view and a side view representation of the geometry involved to obtain the pixel position on the camera image of a sonar feature T. (c) depicts a 3D scene with physical representations of the acoustic beams and visual features correspondence.

The combination of the camera and sonar sensors relies on internal geometry, they are horizontally aligned with a vertical offset. This setup enables an intuitive estimation of the intersection areas of the sonar's acoustic beams with the image plane [8]. Therefore, each beam can be represented as a set of vertical segments on the image. They are mapped to image pixels by using the pinhole model. For each sonar beam, the closest detected feature with high intensity is selected, and since both perception sensors are horizontally aligned, it is straightforward to obtain the horizontal pixels u_i of the ith beam with fixed azimuth θ_i,

$$u_i = f_x \tan(\theta_i \pm \sigma_h) + c_x, \tag{3.10}$$

where σ_h is the angular width, and f_x and c_x, the intrinsic camera parameters. However, the vertical offset of the sensors t_z and the acoustic distances to the objects r_i in the observed scene must be considered to estimate the beam's corresponding vertical pixels v in the image. Therefore, for an observed target T by the sonar in the Oxz plane, such that

$$T = \begin{bmatrix} 0 \\ t_z \end{bmatrix} + r_i \begin{bmatrix} \cos(\phi) \\ \sin(\phi) \end{bmatrix}, \tag{3.11}$$

where the elevation angle ϕ is in $[\phi_{min}, \phi_{max}]$, the possible corresponding vertical pixels become

$$v_i = \begin{cases} f_y \frac{T_z}{T_x} + c_y, & \text{if } T_x \neq 0 \\ c_y, & \text{otherwise}, \end{cases} \tag{3.12}$$

where f_y and c_y are the remaining intrinsic camera parameters. The working principle of the combination and matching method of the features from both sensors

37
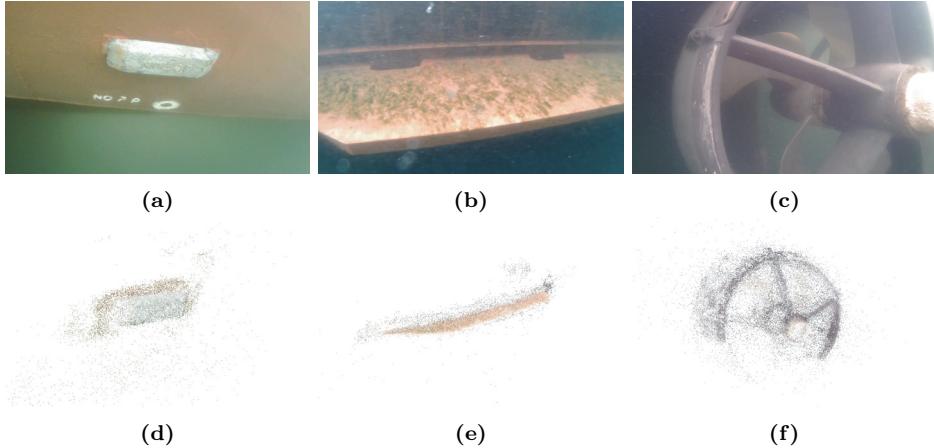
Figure 3.11: Point clouds of PoIs were generated during an inspection mission. The top row includes images extracted from the videos used to make the point clouds of the second row. (a) and (d) show an anode, (b) and (e) show a bildge keel, and (c) and (f), show a propeller.

is displayed in Figure 3.10. The correspondence mapping and the estimation of the intersection regions between the sonar beams and the image plane constrain the search for good visual features to match. Additionally, since only the closest acoustic features are selected, the same is done with the visual features, further restraining to number of potential match. Although the scenes are observed differently by both sensors, the detected relative distances remain the same, therefore the closest acoustic and visual features should correspond. Therefore, the closest detected visual feature that has its 2D projection on the image on the intersection region, is matched to the acoustic feature. This operation is repeated for each reliable acoustic feature.

Comparing each visual-acoustic match provides information about their scale and reliability. A set a scale ratios is obtained by dividing the acoustic distances by the visual distances. In this case, having a set instead of a single value enables robustness and stability for the final depth ratio estimation. The Maximum Likelihood Estimation (MLE) is continuously applied over all matches to obtain a unique and consistent ratio. The set of distance ratios is assumed to follow a Normal probability distribution and its log-likelihood is maximised to obtain an optimised mean which corresponds to the depth ratio of the current scene. Using the confidence intervals of the distribution, the outliers are detected and rejected.

The proposed estimation method was compared to the mean and median of the set, and single beam estimation. Although all methods converge rapidly, the alternative solutions are not continuously stable, making the rendering of a scene unstable and unreliable for robotic applications.

The estimation of the trajectory using the sonar and camera combination was

compared to alternative setups such as a simple monocular SLAM, a Visual Inertial SLAM, and dead reckoning based on a DVL and an IMU. The ground truth was estimated using a mix of Global Positioning System (GPS) fixes and visual landmarks. This enabled performance comparison and showed that the proposed solution outperformed the others.

During the testing and inspection missions, the updated SLAM framework enabled a better mapping of ship parts such as the propellers and bildge keels. A sample of the generated point clouds during operations is displayed in Figure 3.11.

3.3.3 Automatic Detection of Ship Parts and Faults

To move towards an autonomous end-to-end inspection system, the ship parts and faults must be automatically recognised. This domain suffers from the lack of publicly available data, significantly limiting the progress towards automated annotation of hull features and condition. The first large-scale dataset for underwater ship inspection was built to mitigate this situation and to enable development of models for image classification and semantic segmentation. 1893 images are included and 10 object categories are represented and divided into two system categories, faults and ship parts, listed in Table 3.1. The categories were selected based on their relevance for inspections and to provide meaningful insights to the inspector for the report generation.

Deep learning models were trained and tested on this data set to ensure its viability and applicability for real case scenarios. Multiple models with varying architectures were tested, including SOTA segmentation models [80], [127]–[131] and backbones [132]–[134]. Although their performance varies, they were all able to converge quickly during the training. To measure the performance of the models, the popular metric methods were used, the Intersection over Union (IoU) and the F1 Score. They provide a measure of the pixel-wise classification correctness. The results showed promising prediction results, with up to 86.07% mean IoU and 88.17% F1 Score. However, two of the proposed categories are particularly difficult to predict compared to others: paint peel and marine growth. The inference time was also considered since real-time results during an inspection prevents the inspector from having to go through the mission data once the operation is completed. Lighter segmentation models are advantageous in this respect. The U-Net segmentation model [127] with the MobileNetV2 backbone [132] was found to provide the best trade-off between segmentation results and inference time making it an efficient solution for the real case scenarios. On the testing data set, it achieved 80.09% mean IoU and 82.25% F1 Score. Additionally, it can process up to 23.17 Frames Per Second (FPS) on a standard GPU, and up to 12 FPS on a standard consumer laptop without a GPU.

3.4 Reporting

The robotic platform collects data throughout the inspection mission and process them in real-time to enable the inspector to monitor the operation. Several cate-

Table 3.1: Class categories and their descriptions [10]

Group	Class	Description	Mask color
Ship parts	Ship hull	The main ship structure.	Blue
	Propeller	All revolving structures on the ship.	Purple
	Bilge keel	A stabilizing structure on the ship hull to reduce rolling motion.	Orange
	Anode	Sacrificial anodes that provide galvanic cathodic protection of submerged metal structures from corrosion.	Cyan
	Sea chest grating	Sea chests are intake reservoirs for water piping systems on a ship. They are protected by removable gratings.	White
	Overboard valve	Usually located on the sides of the ship. They are round openings on the ship hull that serve as in and outlets.	Turquoise
Inspection criteria	Corrosion	Oxidized metal parts of the ship.	Yellow
	Paint peel	Any damage to the condition of the anti-fouling coverage on the ship hull. That is coating, paint, or other surface treatment that is used on a ship to control or prevent attachment of unwanted marine organisms.	Red
	Marine growth	The accumulation of aquatic organisms such as micro-organisms, algae, and animals on surfaces and structures immersed in or exposed to the aquatic environment. Biofouling types can include soft biofouling and hard calcareous biofouling.	Green
	Defect	All other defects that are neither corrosion, marine growth, nor paint peel.	Pink

gories of data can be identified:

- Navigation data, i.e., where is the vehicle and where it is going, and what is its progress.

- Scene data, corresponding to the data the autonomous system generates using the sonar and the camera for better scene understanding and situation awareness
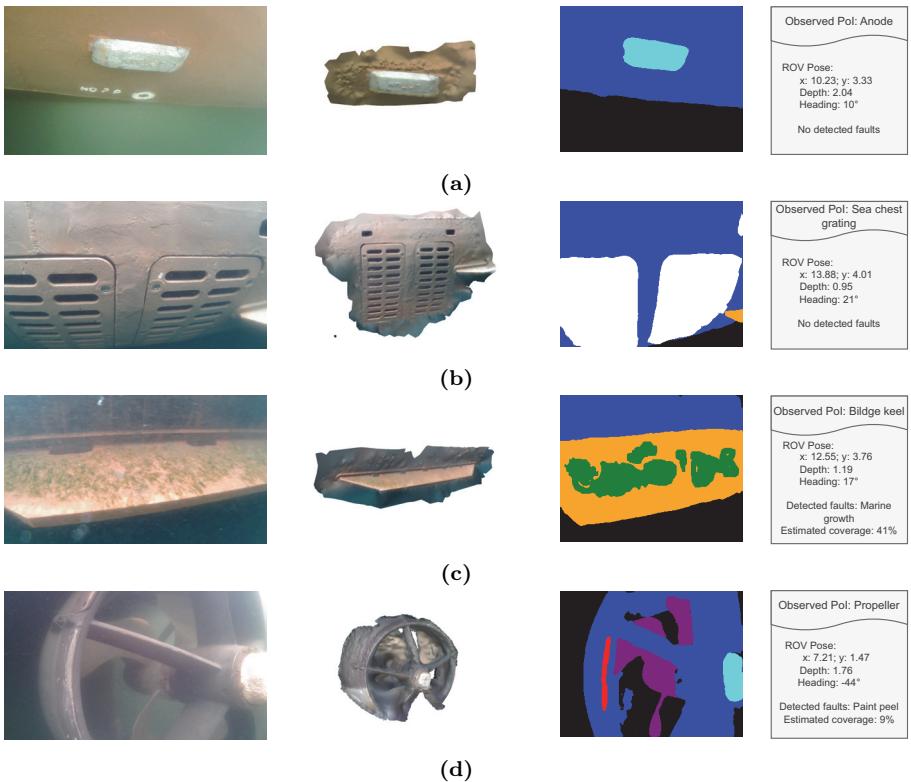
Figure 3.12: Examples of data that can be generated when a PoI is detected. The first column includes the representative images while the second shows the generated 3D textured model of the captured PoI. The third column displays the semantic segmentation masks that are used to detect the PoIs and faults. Finally, the last column reports the pose of the vehicle and the inspection findings. In (a), an anode is detected, a sea chest grating in (b), a bildge keel in (c), and a propeller in (d).

- Inspection aiding data, which includes the actual visual video feed and the detection of PoIs and faults.

The acquired data makes it possible to perform quantitative evaluations and automated data processing to ease the labour intensive process of writing inspection reports [3], [135]. The autonomous inspection is performed in a way to comply with the ABS regulations for remote inspections [106], by respecting the operation setup and collecting all the required data presented in Section 1.1.4 with the exception of physical measurements of the hull. With the aim to prevent the inspector from having to go through the data again and analyse it entirely, markers are placed in the dataset. They correspond to times with inspection findings. All the local mission metadata is attached to the markers, including position of the vehicle, what it is inspecting, and what it has found. Since this operation is done offline, more precise and textured visual models of the PoIs are generated and attached to the markers.

Figure 3.12 presents three examples of markers and associated metadata that can be generated. In [3], a tool to support detailed ship status report generation is proposed, using knowledge graphs in combination with the industry standards.

Such developments contributes to the end-to-end inspection, they enable efficient data retraceability which can be important for verification processes and long term inspection operations. However, a human in the loop is still required to select and approve the data before creating the inspection report.

Chapter 4

Related Applications

Although the proposed approach is designed and intended for underwater ship hull inspection, the problem can be generalized and applied in other domains, but the assumption of a flat surface, or estimable flat planes, must still hold for the proposed autonomous solutions to work; otherwise, the line extracted from the sonar scan is less accurate, making it difficult for the vehicle to correctly face the structure. When the assumption does not hold true, the ROV can perform semi-autonomous missions, relying on manual maneuvering aid for the heading. The methods were tested for harbor wall inspections (see Figure 3.9), for which the assumptions hold. To challenge the solutions and prove their adaptability and efficiency capabilities, aquaculture fish net pens are considered in Section 4.1 and a subsea module in Section 4.2.

4.1 Aquaculture Fish Net Pen Inspection

Today, half of the total seafood production originates from aquaculture facilities [136]. Monitoring the production sites is important to detect in the early stage the net pen degradation and prevent fish escapes which represent an economic loss and an environmental threat. According to reports, structural failures of net cages is one of the leading causes of escaped fish, accounting for up to 75% of all escaped fish [137]–[139].

During an inspection, it is challenging to cover the whole net and holes can be missed, especially when performed by divers which many fish farms still do. In addition to being time consuming, manual inspections represent HSE risks.

ROVs are employed as an alternative [140] and increasing their autonomy would increase safety, efficiency, and reduce cost. Very often optical vision-based navigation is set up [141]–[144] to navigate in the inspection area. Acoustic based methods are also used [145]–[147] to obtain the relative pose of the vehicle relative to the net. However, most of the methods have specific requirements such as known path, known geometry and position of the net, and known dynamic models.

These requirements make them difficult to adapt, scale, and to be used in a fully autonomous mission.

The autonomous inspection method proposed for ship hulls is tested on aquaculture fish net pens [1] and enables data collection for detection of holes and defects in the net pen. The circular geometry of aquaculture fish net pens requires the drone to continuously adapt its path. The vehicle is deployed on the inside and close to the net to be able to observe anomalies and the state of the structure using maneuvering based guidance with inputs from the sonar to navigate along the inspection pattern. It was possible to generate inspection maps and models of the fish cage similar to ship hulls to document and characterize the condition of the structure.

Field trials were carried out on the full-scale aquaculture laboratory SINTEF ACE Korsneset [148] situated on the coast of mid-Norway, see Figure 4.1(a). The data collected during the inspections enabled the generation of orthomosaics representing sections of the net pen. Mosaics consist of aligning and transforming multiple images to create a single image. They represent an effective method to represent larger areas than individual frames. They enable the inspector to visually inspect the net pen in one quick look, instead of going through the entire video data. An example is displayed in Figure 4.1, along with the corresponding acoustic point cloud and inspection map.

It was possible to obtain these results without modifying the methods, showing that the proposed methods for ship hull inspection is well suited for aquaculture fish net pen inspection. This also shows that the robotic inspection procedure is fundamentally the same for both structures and that a generalised method could be developed to include numerous underwater structures.

4.2 Subsea Structure Inspection

Inspection, maintenance, and repair operations on subsea structures are very expensive, and include a vessel with advanced underwater vehicles and specialized operator experts. The number a subsea structures continues to increase, driving the industry to develop further the autonomy in ROV operations. Offshore inspections mainly include underwater platforms, pipelines, and subsea installations [149]–[151]. Local high-level autonomy with automated data processing is still limited but would bridge the gap between manual operations and fully automated missions.

To demonstrate the applicability of the developed solution for subsea structure inspections, a semi-autonomous inspection of a Pig Loop Module (PLM) was performed. Due to the geometric complexity of the structure, it cannot be simplified to a set a planes. Therefore, the assumption of flat surfaces does not hold anymore. In such a scenario, the ROV still follows autonomously a vertical lawnmower pattern using maneuvering based guidance. The path is continuously and automat-
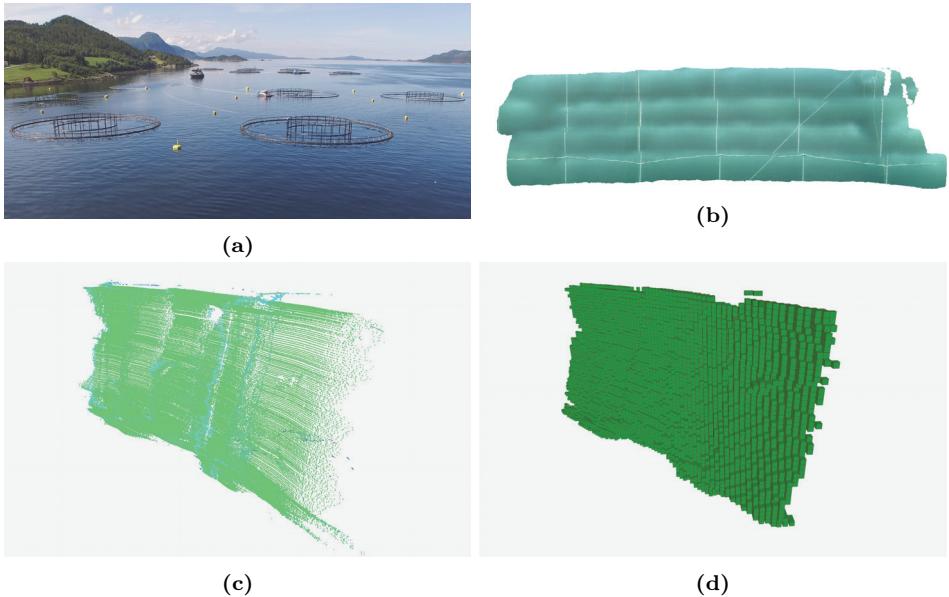
Figure 4.1: The results of the autonomous inspection are displayed in this figure. (a) is an aerial view of the testing site. The video from an inspection was used to generate an orthomosaic of the net pen in (b), and (c) and (d) are respectively the corresponding acoustic point cloud and inspection voxel map generated online.

ically translated using the measurements from the sonar and its processing. This makes it possible to respect the distance constraint to the module and to have a first estimation of the rotation that needs to be applied on the pattern. This rotation is corrected online by the operator to ensure the ROV is correctly facing the structure. Therefore, full visual coverage is still guaranteed as long as the operator rotates correctly the inspection path over time. The results of such a scenario are displayed in Figure 4.2. Compared to the inspection of the aquaculture fish net pen, the 3D textured model of the structure is generated instead of an orthomosaic because it better addresses the inspection needs of such a structure.

This experiment showed that with a more generalised method for sonar processing, i.e., without the flat surface assumption, the proposed inspection procedure can scale to more challenging structures and perform with consistent results regardless of the geometry involved.

(a)

(b)
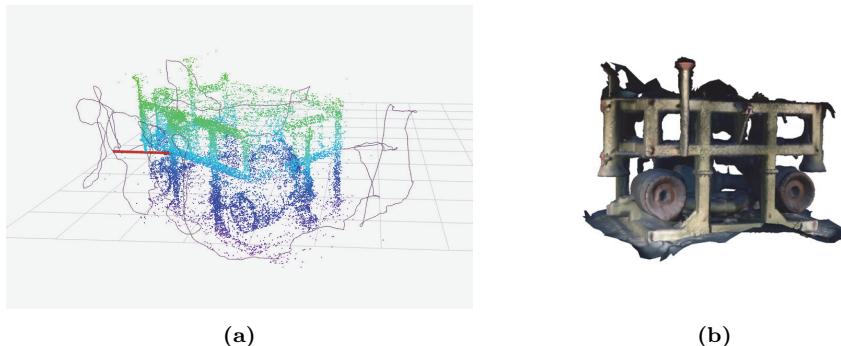
Figure 4.2: The results of the autonomous inspection are displayed in this figure. (a) is the online generated point cloud of the structure and (b) its 3D reconstruction.

Chapter 5

Remarks and Conclusions

5.1 Conclusions

In this thesis a solution contributing towards the end-to-end autonomous robotic inspection of underwater ship hull was presented. The proposed methods were developed while accounting for the limitations of a small and low-cost ROV. Starting with the deployment of the vehicle and ending with the generation of inspection reports, methods for autonomous inspections including localisation, guidance, and mapping were proposed, suggested, and discussed for each step of the remote inspection. They ensure that the mission runs smoothly and provide the necessary tools in real-time to assist the inspector in the assessment of the structure integrity of the ship. By detecting the defects located on the hull while navigating autonomously around it and displaying the corresponding telemetry and imagery, the proposed robotic procedure can be set in an industry relevant environment.

A total of four objectives were presented at the beginning of the thesis covering the inspection pipelines with specific methods.

1. Objective 1 was addressed by proposing a sonar aided guidance strategy. It enabled hull relative navigation to efficiently and consistently inspect the hull and fully visually cover it. The method was built on the assumption that the vehicle is facing a flat structure or estimable plane, allowing processing of the sonar scans to geometrically represent the geometry of the hull. By applying image processing techniques, a line can be extracted from the scan, describing locally the pose of the hull relative to the ROV. The proposed method takes full advantage of the sensors available to enable precise and robust hull relative navigation without prior knowledge of its morphoplogy in the presence of moderate environmental conditions. They include an IMU, a DVL, a pressure sensor and a FLS. The large set of inspected vessels and testing environment showed the adaptability and applicability of the methods in real case scenarios. Repeated tests were performed on ten different ships in six different environments and showed consistent and relevant results. Ad-

ditionally, the robotic procedure was tested on aquaculture fish net pens and subsea structures which allowed to show that it does not need to be changed to be used in other domains.

2. To cover the second objective (2), a dataset was specifically created with the aim to train models to detect PoIs and faults of the hull. Developed with domain experts, this dataset is the first open set dedicated to image classification and semantic segmentation to evaluate the ship's condition. It contains ten categories, defined to best match the inspection needs. To test the dataset, SOTA models were trained on it and quantitative and qualitative results were assessed. They indicated the relevance of the set as very good performance were achieved. The following field experiments further proved the importance of such a dataset in inspection scenarios and how SOTA models can be used online in this context.

3. A method to combine the optical and acoustic data respectively from a monocular camera and a FLS was proposed to resolve the problem of the objective 3. The method was founded on the concept of intersection between the sonar acoustic beams and the image plane, allowing to create correspondences between the acoustic and visual features. The proposed solution enabled real-time scaled mapping and localisation of a visual SLAM framework. It also significantly improved the accuracy of the estimates and outperformed the alternative methods. The improved localisation accuracy propagates to the generation of the point cloud that can be made more robust and denser using the acoustic measurements. Because the acoustic measurement tend to be more reliable than optical measurement, especially underwater, the corresponding extracted features can be used as reference points and constraints for the visual features. When accurate mapping is required, when the ROV is inspecting PoIs, this sensor combination allowed a more representative reconstruction of the structures.

4. The last objective (4) was addressed by providing a specific set of tools to enable the inspectors to have a better understanding of the robotic inspection and to assist them in the decision and report creation process. This was made possible thanks to the online generation of acoustic inspection maps and more detailed models of specific areas of interest with the associated detection of ship parts and faults. Additionally, the proposed solution suggests markers in the inspection dataset potentially containing information the inspector is looking for. The rules and regulations of the class societies formed a design basis for the proposed solution to be applicable to third party ship inspections.

This thesis contributes to the progress towards end-to-end autonomous inspections and when combined together, the proposed methods showcased functional results proving the potential of such end-to-end tasks. With constantly growing needs for automated and remote operations, such integrated tasks will continue to be explored and extended, creating an endless list of possibilities in terms of methodology and technology combinations.

5.2 Future Work

This thesis creates new opportunities for research in multiple fields including cross-disciplinary fields.

Detection of faults remains a challenging task underwater, and the further development of reliable detection methods for underwater imagery would improve the core task of an inspection mission. Better understanding of the scene, using for example semantic slam could be used both for navigation and mission management. Being able to classify and categorise what the robotic platform is currently observing and localising in space would greatly improve the autonomous decision making of the robot.

Handling tilting and turning perception sensors would significantly improve the situation awareness of the robotic platforms in addition to enabling sensor access to more difficult to reach areas. This would also overcome the motion constraints of the ROV.

To enable faster paced inspections, collaborative missions should be considered. Two main robot collaboration setups are identified as improvement for the inspections. The first one is the classic approach of dividing the inspection area according to the number of available autonomous agents, and distributing the tasks among them to share equally the workload. Alternatively, each robot can have an independent goal and work collaboratively to perform a complete inspection. The first drone would scan the hull and create an inspection map that will be used by a set of drones which will inspect more carefully PoIs or use mediums such as ultrasonic sensors for thickness measurement or brushes and pressurised washing tools.

References

[1] A. Cardaillac, H. B. Amundsen, E. Kelasidi, and M. Ludvigsen, "Application of maneuvering based control for autonomous inspection of aquaculture net pens," in *2023 8th Asia-Pacific Conference on Intelligent Robot Systems (ACIRS)*, 2023, pp. 44–51. DOI: 10.1109/ACIRS58671.2023.10239708.

[2] M. Scheiber, A. Cardaillac, C. Brommer, S. Weiss, and M. Ludvigsen, "Modular multi-sensor fusion for underwater localization for autonomous rov operations," in *OCEANS 2022, Hampton Roads*, 2022, pp. 1–5. DOI: 10.1109/OCEANS47191.2022.9977298.

[3] J. Hirsch, B. Elvesæter, A. Cardaillac, B. Bauer, and M. Waszak, "Fusion of multi-modal underwater ship inspection data with knowledge graphs," in *OCEANS 2022, Hampton Roads*, 2022, pp. 1–9. DOI: 10.1109/OCEANS47191.2022.9977371.

[4] A. Cardaillac and M. Ludvigsen, "Marine snow detection for real time feature detection," in *2022 IEEE/OES Autonomous Underwater Vehicles Symposium (AUV)*, 2022, pp. 1–6. DOI: 10.1109/AUV53081.2022.9965895.

[5] A. Cardaillac and M. Ludvigsen, "A communication interface for multilayer cloud computing architecture for low cost underwater vehicles*," *IFAC-PapersOnLine*, vol. 55, no. 14, pp. 77–82, 2022, 11th IFAC Symposium on Intelligent Autonomous Vehicles IAV 2022. DOI: 10.1016/j.ifacol.2022.07.586.

[6] A. Cardaillac and M. Ludvigsen, "Path following for underwater inspection allowing manoeuvring constraints," in *Intelligent Autonomous Systems 17*, Cham: Springer Nature Switzerland, 2023, pp. 867–880. DOI: 10.1007/978-3-031-22216-0_58.

[7] A. Cardaillac and M. Ludvigsen, "Ruled path planning framework for safe and dynamic navigation," in *OCEANS 2021: San Diego – Porto*, 2021, pp. 1–7. DOI: 10.23919/OCEANS44145.2021.9705699.

[8] A. Cardaillac and M. Ludvigsen, "Camera-sonar combination for improved underwater localization and mapping," *IEEE Access*, vol. 11, pp. 123 070–123 079, 2023. DOI: 10.1109/ACCESS.2023.3329834.

[9] A. Cardaillac, R. Skjetne, and M. Ludvigsen, "Rov-based autonomous maneuvering for ship hull inspection with coverage monitoring," *Journal of Intelligent & Robotic Systems*, 2023, [IN REVIEW].

[10] M. Waszak, A. Cardaillac, B. Elvesæter, F. Rødølen, and M. Ludvigsen, "Semantic segmentation in underwater ship inspections: Benchmark and data set," *IEEE Journal of Oceanic Engineering*, pp. 1–12, 2022. DOI: 10. 1109/JOE.2022.3219129.

[11] U. N. C. on Trade and Development, *Review of Maritime Transport 2022*. 2022.

[12] B. Boon, F. Brennan, Y. Garbatov, C. Ji, J. Parunov, T. Rahman, C. Rizzo, A. Rouhan, C. Shin, and N. Yamamoto, "Condition assessment of aged ships and offshore structures," in *International Ship and Offshore Structures Congress*, vol. 2, 2009, pp. 313–365.

[13] M. U. S. N. I. Woods Hole Oceanographic Institution. Annapolis, "Marine fouling and its prevention.," *Science*, vol. 118, no. 3061, pp. 257–257, 1953. DOI: 10.1126/science.118.3061.257.a.

[14] J. Lewis, "Marine biofouling and its prevention on underwater surfaces," *Materials Forum*, vol. 22, pp. 41–61, Jan. 1998.

[15] *NOAA Ocean Exploration*, https://oceanexplorer.noaa.gov, 2023.

[16] M. Morgado, P. Oliveira, C. Silvestre, and J. F. Vasconcelos, "Usbl/ins tightly-coupled integration technique for underwater vehicles," in *2006 9th International Conference on Information Fusion*, 2006, pp. 1–8. DOI: 10. 1109/ICIF.2006.301607.

[17] P. Batista, C. Silvestre, and P. Oliveira, "Tightly coupled long baseline/ultra-short baseline integrated navigation system," *International Journal of Systems Science*, vol. 47, no. 8, pp. 1837–1855, 2016. DOI: 10. 1080/00207721.2014.955070.

[18] T. Zhang, L. Chen, and Y. Li, "Auv underwater positioning algorithm based on interactive assistance of sins and lbl," *Sensors*, vol. 16, no. 1, 2016. DOI: 10.3390/s16010042.

[19] A. Tal, I. Klein, and R. Katz, "Inertial navigation system/doppler velocity log (ins/dvl) fusion with partial dvl measurements," *Sensors*, vol. 17, no. 2, 2017. DOI: 10.3390/s17020415.

[20] M. Karimi, M. Bozorg, and A. R. Khayatian, "A comparison of dvl/ins fusion by ukf and ekf to localize an autonomous underwater vehicle," in *2013 First RSI/ISM International Conference on Robotics and Mechatronics (ICRoM)*, 2013, pp. 62–67. DOI: 10.1109/ICRoM.2013.6510082.

[21] L. Zhao, Y. Kang, J. Cheng, and M. Wu, "A fault-tolerant polar grid sins/dvl/usbl integrated navigation algorithm based on the centralized filter and relative position measurement," *Sensors*, vol. 19, p. 3899, Sep. 2019. DOI: 10.3390/s19183899.

[22] H. Durrant-Whyte and T. Bailey, "Simultaneous localization and mapping: Part i," *IEEE Robotics & Automation Magazine*, vol. 13, no. 2, pp. 99–110, 2006. DOI: 10.1109/MRA.2006.1638022.

[23] R. A. Newcombe, S. J. Lovegrove, and A. J. Davison, "Dtam: Dense tracking and mapping in real-time," in *2011 International Conference on Computer Vision*, 2011, pp. 2320–2327. DOI: 10.1109/ICCV.2011.6126513.

[24] J. Engel, T. Schöps, and D. Cremers, "Lsd-slam: Large-scale direct monocular slam," in *Computer Vision – ECCV 2014*, D. Fleet, T. Pajdla, B. Schiele, and T. Tuytelaars, Eds., Cham: Springer International Publishing, 2014, pp. 834–849. DOI: 10.1007/978-3-319-10605-2_54.

[25] C. Forster, M. Pizzoli, and D. Scaramuzza, "Svo: Fast semi-direct monocular visual odometry," in *2014 IEEE International Conference on Robotics and Automation (ICRA)*, 2014, pp. 15–22. DOI: 10.1109/ICRA.2014.6906584.

[26] C. Forster, Z. Zhang, M. Gassner, M. Werlberger, and D. Scaramuzza, "Svo: Semidirect visual odometry for monocular and multicamera systems," *IEEE Transactions on Robotics*, vol. 33, no. 2, pp. 249–265, 2017. DOI: 10.1109/TRO.2016.2623335.

[27] J. Engel, V. Koltun, and D. Cremers, "Direct sparse odometry," *IEEE Transactions on Pattern Analysis & Machine Intelligence*, vol. 40, no. 03, pp. 611–625, Mar. 2018. DOI: 10.1109/TPAMI.2017.2658577.

[28] Davison, "Real-time simultaneous localisation and mapping with a single camera," in *Proceedings Ninth IEEE International Conference on Computer Vision*, 2003, 1403–1410 vol.2. DOI: 10.1109/ICCV.2003.1238654.

[29] A. J. Davison, I. D. Reid, N. D. Molton, and O. Stasse, "Monoslam: Real-time single camera slam," *IEEE Transactions on Pattern Analysis and Machine Intelligence*, vol. 29, no. 6, pp. 1052–1067, 2007. DOI: 10.1109/TPAMI.2007.1049.

[30] G. Klein and D. Murray, "Parallel tracking and mapping for small ar workspaces," in *2007 6th IEEE and ACM International Symposium on Mixed and Augmented Reality*, 2007, pp. 225–234. DOI: 10.1109/ISMAR.2007.4538852.

[31] R. Mur-Artal, J. M. M. Montiel, and J. D. Tardós, "ORB-SLAM: A versatile and accurate monocular SLAM system," *IEEE Transactions on Robotics*, vol. 31, no. 5, pp. 1147–1163, 2015. DOI: 10.1109/TRO.2015.2463671.

[32] R. Mur-Artal and J. D. Tardós, "ORB-SLAM2: An open-source SLAM system for monocular, stereo and RGB-D cameras," *IEEE Transactions on Robotics*, vol. 33, no. 5, pp. 1255–1262, 2017. DOI: 10.1109/TRO.2017.2705103.

[33] C. Campos, R. Elvira, J. J. G. Rodríguez, J. M. M. Montiel, and J. D. Tardós, "Orb-slam3: An accurate open-source library for visual, visual–inertial, and multimap slam," *IEEE Transactions on Robotics*, vol. 37, no. 6, pp. 1874–1890, 2021. DOI: 10.1109/TRO.2021.3075644.

[34] Y. Zhang, L. Zhou, H. Li, J. Zhu, and W. Du, "Marine application evaluation of monocular slam for underwater robots," *Sensors*, vol. 22, no. 13, 2022. DOI: 10.3390/s22134657.

[35] F. Hidalgo, C. Kahlefendt, and T. Bräunl, "Monocular orb-slam application in underwater scenarios," in *2018 OCEANS - MTS/IEEE Kobe Techno-Oceans (OTO)*, 2018, pp. 1–4. DOI: 10.1109/OCEANSKOBE.2018.8559435.

[36] M. Leonardi, A. Stahl, E. F. Brekke, and M. Ludvigsen, "Uvs: Underwater visual slam—a robust monocular visual slam system for lifelong underwater operations," *Autonomous Robots*, Sep. 2023. DOI: 10.1007/s10514-023-10138-0.

[37] E. Vargas, R. Scona, J. S. Willners, T. Luczynski, Y. Cao, S. Wang, and Y. R. Petillot, "Robust underwater visual slam fusing acoustic sensing," in *2021 IEEE International Conference on Robotics and Automation (ICRA)*, 2021, pp. 2140–2146. DOI: 10.1109/ICRA48506.2021.9561537.

[38] H. Huang, W.-Y. Lin, S. Liu, D. Zhang, and S.-K. Yeung, "Dual-slam: A framework for robust single camera navigation," in *2020 IEEE/RSJ International Conference on Intelligent Robots and Systems (IROS)*, 2020, pp. 4942–4949. DOI: 10.1109/IROS45743.2020.9341513.

[39] M. Ferrera, J. Moras, P. Trouvé-Peloux, and V. Creuze, "Real-time monocular visual odometry for turbid and dynamic underwater environments," *Sensors*, vol. 19, no. 3, 2019. DOI: 10.3390/s19030687.

[40] F. Hidalgo and T. Bräunl, "Review of underwater slam techniques," in *2015 6th International Conference on Automation, Robotics and Applications (ICARA)*, 2015, pp. 306–311. DOI: 10.1109/ICARA.2015.7081165.

[41] J. D. Hernández, K. Istenič, N. Gracias, N. Palomeras, R. Campos, E. Vidal, R. García, and M. Carreras, "Autonomous underwater navigation and optical mapping in unknown natural environments," *Sensors*, vol. 16, no. 8, p. 1174, 2016. DOI: 10.3390/s16081174.

[42] E. W. Dijkstra, "A note on two problems in connexion with graphs," *Numer. Math.*, vol. 1, no. 1, pp. 269–271, Dec. 1959. DOI: 10.1007/BF01386390.

[43] P. E. Hart, N. J. Nilsson, and B. Raphael, "A formal basis for the heuristic determination of minimum cost paths," *IEEE Transactions on Systems Science and Cybernetics*, vol. 4, no. 2, pp. 100–107, 1968. DOI: 10.1109/TSSC.1968.300136.

[44] J. Sethian, "Level set methods and fast marching methods: Evolving interfaces in computational geometry, fluid mechanics, computer vision, and materials science," 1999.

[45] S. M. LaValle, "Rapidly-exploring random trees: A new tool for path planning," Computer Science Dept, Iowa State University, Tech. Rep., 1998.

[46] L. E. Kavraki, P. Svestka, J. .-. Latombe, and M. H. Overmars, "Probabilistic roadmaps for path planning in high-dimensional configuration spaces," *IEEE Transactions on Robotics and Automation*, vol. 12, no. 4, pp. 566–580, 1996. DOI: 10.1109/70.508439.

[47] S. Karaman and E. Frazzoli, "Sampling-based algorithms for optimal motion planning," *The International Journal of Robotics Research*, vol. 30, no. 7, pp. 846–894, 2011. DOI: 10.1177/0278364911406761.

[48] J. McMahon and E. Plaku, "Mission and motion planning for autonomous underwater vehicles operating in spatially and temporally complex environments," *IEEE Journal of Oceanic Engineering*, vol. 41, no. 4, pp. 893–912, 2016. DOI: 10.1109/JOE.2015.2503498.

[49] J. Poppinga, A. Birk, K. Pathak, and N. Vaskevicius, "Fast 6-dof path planning for autonomous underwater vehicles (auv) based on 3d plane mapping," in *2011 IEEE International Symposium on Safety, Security, and Rescue Robotics*, 2011, pp. 345–350. DOI: 10.1109/SSRR.2011.6106771.

[50] R. Cui, Y. Li, and W. Yan, "Mutual information-based multi-auv path planning for scalar field sampling using multidimensional rrt*," *IEEE Transactions on Systems, Man, and Cybernetics: Systems*, vol. 46, no. 7, pp. 993–1004, 2016. DOI: 10.1109/TSMC.2015.2500027.

[51] Z. Zhang, D. Wu, J. Gu, and F. Li, "A path-planning strategy for unmanned surface vehicles based on an adaptive hybrid dynamic stepsize and target attractive force-rrt algorithm," *Journal of Marine Science and Engineering*, vol. 7, no. 5, 2019. DOI: 10.3390/jmse7050132.

[52] E. Taheri, M. H. Ferdowsi, and M. Danesh, "Closed-loop randomized kinodynamic path planning for an autonomous underwater vehicle," *Applied Ocean Research*, vol. 83, pp. 48–64, 2019. DOI: 10.1016/j.apor.2018.12.008.

[53] J. D. Hernández, E. Vidal, G. Vallicrosa, E. Galceran, and M. Carreras, "Online path planning for autonomous underwater vehicles in unknown environments," in *2015 IEEE International Conference on Robotics and Automation (ICRA)*, 2015, pp. 1152–1157. DOI: 10.1109/ICRA.2015.7139336.

[54] Y. S. Song and M. R. Arshad, "Coverage path planning for underwater pole inspection using an autonomous underwater vehicle," in *2016 IEEE International Conference on Automatic Control and Intelligent Systems (I2CACIS)*, 2016, pp. 230–235. DOI: 10.1109/I2CACIS.2016.7885320.

[55] G. A. Hollinger, U. Mitra, and G. S. Sukhatme, "Active and adaptive dive planning for dense bathymetric mapping," in *Experimental Robotics: The 13th International Symposium on Experimental Robotics*, J. P. Desai, G. Dudek, O. Khatib, and V. Kumar, Eds. Heidelberg: Springer International Publishing, 2013, pp. 803–817. DOI: 10.1007/978-3-319-00065-7_54.

[56] B. Chen, P. Pandey, and D. Pompili, "An adaptive sampling solution using autonomous underwater vehicles," *IFAC Proceedings Volumes*, vol. 45, no. 27, pp. 352–356, 2012, 9th IFAC Conference on Manoeuvring and Control of Marine Craft. DOI: 10.3182/20120919-3-IT-2046.00060.

[57] E. Galceran, R. Campos, N. Palomeras, M. Carreras, and P. Ridao, "Coverage path planning with realtime replanning for inspection of 3d underwater structures," in *2014 IEEE International Conference on Robotics and Automation (ICRA)*, 2014, pp. 6586–6591. DOI: 10.1109/ICRA.2014.6907831.

[58] Y.-H. Lin, L.-C. Huang, S.-Y. Chen, and C.-M. Yu, "The optimal route planning for inspection task of autonomous underwater vehicle composed of mopso-based dynamic routing algorithm in currents," *Applied Ocean Research*, vol. 75, pp. 178–192, 2018. DOI: 10.1016/j.apor.2018.03.016.

[59] S.-H. Yoo, A. Stuntz, Y. Zhang, R. Rothschild, G. A. Hollinger, and R. N. Smith, "Experimental analysis of receding horizon planning algorithms for marine monitoring," in *Field and Service Robotics: Results of the 10th International Conference*, D. S. Wettergreen and T. D. Barfoot, Eds. Cham: Springer International Publishing, 2016, pp. 31–44. DOI: 10.1007/978-3-319-27702-8_3.

[60] J. Hauser and R. Hindman, "Maneuver regulation from trajectory tracking: Feedback linearizable systems*," *IFAC Proceedings Volumes*, vol. 28, no. 14, pp. 595–600, 1995, 3rd IFAC Symposium on Nonlinear Control Systems Design 1995, Tahoe City, CA, USA, 25-28 June 1995. DOI: 10.1016/S1474-6670(17)46893-5.

[61] R. Skjetne, "The maneuvering problem," Ph.D. dissertation, Norwegian University of Science and Technology (NTNU), Trondheim, Norway, 2005.

[62] T. Fossen, *Handbook of Marine Craft Hydrodynamics and Motion Control*. John Wiley & Sons, Ltd, May 2011, p. 575. DOI: 10.1002/9781119994138.

[63] M. Breivik and T. Fossen, "Principles of guidance-based path following in 2D and 3D," in *Proc. the 44th IEEE Conference on Decision and Control*, 2005, pp. 627–634. DOI: 10.1109/CDC.2005.1582226.

[64] W. Caharija, K. Y. Pettersen, M. Bibuli, P. Calado, E. Zereik, J. Braga, J. T. Gravdahl, A. J. Sørensen, M. Milovanović, and G. Bruzzone, "Integral line-of-sight guidance and control of underactuated marine vehicles: Theory, simulations, and experiments," *IEEE Transactions on Control Systems Technology*, vol. 24, no. 5, pp. 1623–1642, 2016. DOI: 10.1109/TCST.2015.2504838.

[65] E. Kelasidi, P. Liljebäck, K. Y. Pettersen, and J. T. Gravdahl, "Integral line-of-sight guidance for path following control of underwater snake robots: Theory and experiments," *IEEE Transactions on Robotics*, vol. 33, no. 3, pp. 610–628, 2017. DOI: 10.1109/TRO.2017.2651119.

[66] *3D Path Following and Tracking for an Inspection Class ROV*, vol. Volume 7A: Ocean Engineering, International Conference on Offshore Mechanics and Arctic Engineering, Jun. 2017, V07AT06A019. DOI: 10.1115/OMAE2017-61170.

[67] S. Moe, K. Y. Pettersen, T. I. Fossen, and J. T. Gravdahl, "Line-of-sight curved path following for underactuated usvs and auvs in the horizontal plane under the influence of ocean currents," in *2016 24th Mediterranean Conference on Control and Automation (MED)*, 2016, pp. 38–45. DOI: 10.1109/MED.2016.7536018.

[68] C. Tang, U. F. von Lukas, M. Vahl, S. Wang, Y. Wang, and M. Tan, "Efficient underwater image and video enhancement based on retinex," *Signal, Image and Video Processing*, vol. 13, no. 5, pp. 1011–1018, Jul. 2019. DOI: `10.1007/s11760-019-01439-y`.

[69] C. Desai, B. S. S. Reddy, R. A. Tabib, U. Patil, and U. Mudenagudi, "Aquagan: Restoration of underwater images," in *2022 IEEE/CVF Conference on Computer Vision and Pattern Recognition Workshops (CVPRW)*, 2022, pp. 295–303. DOI: `10.1109/CVPRW56347.2022.00044`.

[70] X. Li, G. Hou, K. Li, and Z. Pan, "Enhancing underwater image via adaptive color and contrast enhancement, and denoising," *Engineering Applications of Artificial Intelligence*, vol. 111, p. 104 759, 2022. DOI: `10.1016/j.engappai.2022.104759`.

[71] K. Iqbal, R. Abdul Salam, O. Azam, and A. Talib, "Underwater image enhancement using an integrated colour model," *IAENG International Journal of Computer Science*, vol. 34, Jan. 2007.

[72] Z. Wang, W. Liu, Y. Wang, and B. Liu, "Agcyclegan: Attention-guided cyclegan for single underwater image restoration," in *ICASSP 2022 - 2022 IEEE International Conference on Acoustics, Speech and Signal Processing (ICASSP)*, 2022, pp. 2779–2783. DOI: `10.1109/ICASSP43922.2022.9746215`.

[73] M. J. Islam, Y. Xia, and J. Sattar, "Fast underwater image enhancement for improved visual perception," *IEEE Robotics and Automation Letters*, vol. 5, no. 2, pp. 3227–3234, 2020. DOI: `10.1109/LRA.2020.2974710`.

[74] J. Redmon, S. Divvala, R. Girshick, and A. Farhadi, "You only look once: Unified, real-time object detection," in *2016 IEEE Conference on Computer Vision and Pattern Recognition (CVPR)*, 2016, pp. 779–788. DOI: `10.1109/CVPR.2016.91`.

[75] X. Hu, Y. Liu, Z. Zhao, J. Liu, X. Yang, C. Sun, S. Chen, B. Li, and C. Zhou, "Real-time detection of uneaten feed pellets in underwater images for aquaculture using an improved yolo-v4 network," *Computers and Electronics in Agriculture*, vol. 185, p. 106 135, 2021. DOI: `10.1016/j.compag.2021.106135`.

[76] K. M. Knausgård, A. Wiklund, T. K. Sørdalen, K. T. Halvorsen, A. R. Kleiven, L. Jiao, and M. Goodwin, "Temperate fish detection and classification: A deep learning based approach," *Applied Intelligence*, vol. 52, no. 6, pp. 6988–7001, Apr. 2022. DOI: `10.1007/s10489-020-02154-9`.

[77] J. Yan, Z. Zhou, D. Zhou, B. Su, Z. Xuanyuan, J. Tang, Y. Lai, J. Chen, and W. Liang, "Underwater object detection algorithm based on attention mechanism and cross-stage partial fast spatial pyramidal pooling," *Frontiers in Marine Science*, vol. 9, 2022. DOI: `10.3389/fmars.2022.1056300`.

[78] M. Pedersen, J. Bruslund Haurum, R. Gade, and T. B. Moeslund, "Detection of marine animals in a new underwater dataset with varying visibility," in *Proceedings of the IEEE/CVF Conference on Computer Vision and Pattern Recognition (CVPR) Workshops*, Jun. 2019.

[79] H. Qin, X. Li, J. Liang, Y. Peng, and C. Zhang, "Deepfish: Accurate underwater live fish recognition with a deep architecture," *Neurocomputing*, vol. 187, pp. 49–58, 2016, Recent Developments on Deep Big Vision. DOI: `10.1016/j.neucom.2015.10.122`.

[80] M. J. Islam, C. Edge, Y. Xiao, P. Luo, M. Mehtaz, C. Morse, S. S. Enan, and J. Sattar, "Semantic segmentation of underwater imagery: Dataset and benchmark," in *2020 IEEE/RSJ International Conference on Intelligent Robots and Systems (IROS)*, 2020, pp. 1769–1776. DOI: `10.1109/IROS45743.2020.9340821`.

[81] J. Wang, X. He, F. Shao, G. Lu, R. Hu, and Q. Jiang, "Semantic segmentation method of underwater images based on encoder-decoder architecture," *PLOS ONE*, vol. 17, no. 8, pp. 1–19, Aug. 2022. DOI: `10.1371/journal.pone.0272666`.

[82] T.-Y. Lin, M. Maire, S. Belongie, J. Hays, P. Perona, D. Ramanan, P. Dollár, and C. L. Zitnick, "Microsoft coco: Common objects in context," in *Computer Vision – ECCV 2014*, D. Fleet, T. Pajdla, B. Schiele, and T. Tuytelaars, Eds., Cham: Springer International Publishing, 2014, pp. 740–755.

[83] B. Zhou, H. Zhao, X. Puig, S. Fidler, A. Barriuso, and A. Torralba, "Scene parsing through ade20k dataset," in *2017 IEEE Conference on Computer Vision and Pattern Recognition (CVPR)*, 2017, pp. 5122–5130. DOI: `10.1109/CVPR.2017.544`.

[84] J. Deng, W. Dong, R. Socher, L.-J. Li, K. Li, and L. Fei-Fei, "Imagenet: A large-scale hierarchical image database," in *2009 IEEE Conference on Computer Vision and Pattern Recognition*, 2009, pp. 248–255. DOI: `10.1109/CVPR.2009.5206848`.

[85] B. Zhou, H. Zhao, X. Puig, T. Xiao, S. Fidler, A. Barriuso, and A. Torralba, "Semantic understanding of scenes through the ade20k dataset," *International Journal of Computer Vision*, vol. 127, no. 3, pp. 302–321, 2019.

[86] M. Cordts, M. Omran, S. Ramos, T. Rehfeld, M. Enzweiler, R. Benenson, U. Franke, S. Roth, and B. Schiele, "The cityscapes dataset for semantic urban scene understanding," in *2016 IEEE Conference on Computer Vision and Pattern Recognition (CVPR)*, Los Alamitos, CA, USA: IEEE Computer Society, Jun. 2016, pp. 3213–3223. DOI: `10.1109/CVPR.2016.350`.

[87] M. J. Islam, M. Fulton, and J. Sattar, "Toward a generic diver-following algorithm: Balancing robustness and efficiency in deep visual detection," *IEEE Robotics and Automation Letters*, vol. 4, no. 1, pp. 113–120, 2019. DOI: `10.1109/LRA.2018.2882856`.

[88] O. Beijbom, P. J. Edmunds, D. I. Kline, B. G. Mitchell, and D. Kriegman, "Automated annotation of coral reef survey images," in *2012 IEEE Conference on Computer Vision and Pattern Recognition*, 2012, pp. 1170–1177. DOI: `10.1109/CVPR.2012.6247798`.

[89] I. Alonso, M. Yuval, G. Eyal, T. Treibitz, and A. C. Murillo, "Coralseg: Learning coral segmentation from sparse annotations," *Journal of Field Robotics*, vol. 36, no. 8, pp. 1456–1477, 2019. DOI: `10.1002/rob.21915`.

[90] M. Radolko, F. Farhadifard, and U. F. von Lukas, "Dataset on underwater change detection," in *OCEANS 2016 MTS/IEEE Monterey*, 2016, pp. 1–8. DOI: `10.1109/OCEANS.2016.7761129`.

[91] G. Trimble and E. Belcher, "Ship berthing and hull inspection using the cetusii auv and miris high-resolution sonar," in *OCEANS '02 MTS/IEEE*, vol. 2, 2002, 1172–1175 vol.2. DOI: `10.1109/OCEANS.2002.1192132`.

[92] J. Vaganay, M. Elkins, S. Willcox, F. Hover, R. Damus, S. Desset, J. Morash, and V. Polidoro, "Ship hull inspection by hull-relative navigation and control," in *Proceedings of OCEANS 2005 MTS/IEEE*, 2005, 761–766 Vol. 1. DOI: `10.1109/OCEANS.2005.1639844`.

[93] S. Negahdaripour and P. Firoozfam, "An rov stereovision system for ship-hull inspection," *IEEE Journal of Oceanic Engineering*, vol. 31, no. 3, pp. 551–564, 2006. DOI: `10.1109/JOE.2005.851391`.

[94] M. Kaess, H. Johannsson, B. Englot, F. S. Hover, and J. J. Leonard, "Towards autonomous ship hull inspection using the bluefin hauv," in *9th International Symposium on Technology and the Mine Problem. Conference Proceedings*, 2010, pp. 1–10.

[95] F. S. Hover, R. M. Eustice, A. Kim, B. Englot, H. Johannsson, M. Kaess, and J. J. Leonard, "Advanced perception, navigation and planning for autonomous in-water ship hull inspection," *The International Journal of Robotics Research*, vol. 31, no. 12, pp. 1445–1464, 2012. DOI: `10.1177/0278364912461059`.

[96] S. Hong, D. Chung, J. Kim, Y. Kim, A. Kim, and H. K. Yoon, "In-water visual ship hull inspection using a hover-capable underwater vehicle with stereo vision," *Journal of Field Robotics*, vol. 36, no. 3, pp. 531–546, 2019. DOI: `10.1002/rob.21841`.

[97] S. Hong and J. Kim, "Three-dimensional visual mapping of underwater ship hull surface using image stitching geometry," *Ocean Engineering*, vol. 269, p. 113 575, 2023. DOI: `10.1016/j.oceaneng.2022.113575`.

[98] D. Chung and J. Kim, "Underwater visual mapping of curved ship hull surface using stereo vision," *Autonomous Robots*, vol. 47, Jan. 2023. DOI: `10.1007/s10514-022-10071-8`.

[99] S. Hong and J. Kim, "Three-dimensional visual mapping of underwater ship hull surface using piecewise-planar slam," *International Journal of Control, Automation and Systems*, vol. 18, pp. 564–574, Mar. 2020. DOI: `10.1007/s12555-019-0646-8`.

[100] F. Bonnin-Pascual and A. Ortiz, "A novel approach for defect detection on vessel structures using saliency-related features," *Ocean Engineering*, vol. 149, pp. 397–408, 2018. DOI: `10.1016/j.oceaneng.2017.08.024`.

[101] C. Fernández-Isla, P. J. Navarro, and P. M. Alcover, "Automated visual inspection of ship hull surfaces using the wavelet transform," *Mathematical Problems in Engineering*, vol. 2013, p. 101 837, May 2013. DOI: `10.1155/2013/101837`.

[102] B. C. Kim, H. C. Kim, S. Han, and D. K. Park, "Inspection of underwater hull surface condition using the soft voting ensemble of the transfer-learned models," *Sensors*, vol. 22, no. 12, p. 4392, Jun. 2022. DOI: `10.3390/s22124392`.

[103] R. Andersen, L. Nalpantidis, O. Ravn, and E. Boukas, "Investigating deep learning architectures towards autonomous inspection for marine classification," in *2020 IEEE International Symposium on Safety, Security, and Rescue Robotics (SSRR)*, 2020, pp. 197–204. DOI: `10.1109/SSRR50563.2020.9292621`.

[104] *International Maritime Organization*, `https://www.imo.org`, 2023.

[105] *International Association of Classification Societies*, `https://iacs.org.uk/`, 2023.

[106] *American Bureau of Sipping*, `https://ww2.eagle.org`, 2023.

[107] *Det Norske Veritas group*, `https://www.dnv.com`, 2023.

[108] *Registro Italiano Navale*, `https://www.rina.org/en`, 2023.

[109] *Blueye Robotics*, `https://www.blueyerobotics.com/`, 2023.

[110] *Raspberry Pi*, `https://www.raspberrypi.com/`, 2023.

[111] S. Koenig and M. Likhachev, "Fast replanning for navigation in unknown terrain," *IEEE Transactions on Robotics*, vol. 21, no. 3, pp. 354–363, 2005. DOI: `10.1109/TRO.2004.838026`.

[112] C. Brommer, R. Jung, J. Steinbrener, and S. Weiss, "Mars: A modular and robust sensor-fusion framework," *IEEE Robotics and Automation Letters*, vol. 6, no. 2, pp. 359–366, 2021. DOI: `10.1109/LRA.2020.3043195`.

[113] M. A. Fischler and R. C. Bolles, "Random sample consensus: A paradigm for model fitting with applications to image analysis and automated cartography," *Commun. ACM*, vol. 24, no. 6, pp. 381–395, Jun. 1981. DOI: `10.1145/358669.358692`.

[114] V. Nguyen, A. Martinelli, N. Tomatis, and R. Siegwart, "A comparison of line extraction algorithms using 2d laser rangefinder for indoor mobile robotics," in *2005 IEEE/RSJ International Conference on Intelligent Robots and Systems*, 2005, pp. 1929–1934. DOI: `10.1109/IROS.2005.1545234`.

[115] J. Canny, "A computational approach to edge detection," *IEEE Transactions on Pattern Analysis and Machine Intelligence*, vol. PAMI-8, no. 6, pp. 679–698, 1986. DOI: `10.1109/TPAMI.1986.4767851`.

[116] M. Breivik and T. I. Fossen, "Guidance laws for autonomous underwater vehicles," in *Underwater Vehicles*, A. V. Inzartsev, Ed., Rijeka: IntechOpen, 2009, ch. 4, pp. 51–76. DOI: `10.5772/6696`.

[117] A. M. Lekkas and T. I. Fossen, "A time-varying lookahead distance guidance law for path following," *IFAC Proceedings Volumes*, vol. 45, no. 27, pp. 398–403, 2012, 9th IFAC Conference on Manoeuvring and Control of Marine Craft. DOI: `10.3182/20120919-3-IT-2046.00068`.

[118] E. Børhaug, A. Pavlov, and K. Y. Pettersen, "Integral LOS control for path following of underactuated marine surface vessels in the presence of constant ocean currents," in *Proc. 47th IEEE Conference on Decision and Control*, 2008, pp. 4984–4991. DOI: `10.1109/CDC.2008.4739352`.

[119] M. E. N. Sørensen, M. Breivik, and R. Skjetne, "Comparing combinations of linear and nonlinear feedback terms for ship motion control," *IEEE Access*, vol. 8, pp. 193 813–193 826, 2020. DOI: `10.1109/ACCESS.2020.3033409`.

[120] C. Cheng, C. Wang, D. Yang, W. Liu, and F. Zhang, "Underwater localization and mapping based on multi-beam forward looking sonar," *Frontiers in Neurorobotics*, vol. 15, 2022. DOI: `10.3389/fnbot.2021.801956`.

[121] R. Dia, J. Mottin, T. Rakotovao, D. Puschini, and S. Lesecq, "Evaluation of occupancy grid resolution through a novel approach for inverse sensor modeling," *IFAC-PapersOnLine*, vol. 50, no. 1, pp. 13 841–13 847, 2017, 20th IFAC World Congress. DOI: `10.1016/j.ifacol.2017.08.2225`.

[122] D. E. Tyler, "A Distribution-Free M-Estimator of Multivariate Scatter," *The Annals of Statistics*, vol. 15, no. 1, pp. 234–251, 1987. DOI: `10.1214/aos/1176350263`.

[123] L. Dümbgen, "On tyler's m-functional of scatter in high dimension," *Annals of the Institute of Statistical Mathematics*, vol. 50, no. 3, pp. 471–491, 1998. DOI: `10.1023/A:1003573311481`.

[124] D. Paindaveine, "A canonical definition of shape," *Statistics & Probability Letters*, vol. 78, no. 14, pp. 2240–2247, 2008. DOI: `10.1016/j.spl.2008.01.094`.

[125] K. He, J. Sun, and X. Tang, "Guided image filtering," *IEEE Transactions on Pattern Analysis and Machine Intelligence*, vol. 35, no. 6, pp. 1397–1409, 2013. DOI: `10.1109/TPAMI.2012.213`.

[126] K. He and J. Sun, *Fast guided filter*, 2015. DOI: `10.48550/ARXIV.1505.00996`.

[127] O. Ronneberger, P.Fischer, and T. Brox, "U-net: Convolutional networks for biomedical image segmentation," in *Medical Image Computing and Computer-Assisted Intervention (MICCAI)*, ser. LNCS, vol. 9351, Springer, 2015, pp. 234–241.

[128] L.-C. Chen, G. Papandreou, F. Schroff, and H. Adam, "Rethinking atrous convolution for semantic image segmentation," *2017 IEEE Conference on Computer Vision and Pattern Recognition (CVPR)*, 2017.

[129] T.-Y. Lin, P. Dollár, R. Girshick, K. He, B. Hariharan, and S. Belongie, "Feature pyramid networks for object detection," *2017 IEEE Conference on Computer Vision and Pattern Recognition (CVPR)*, 2017.

[130] H. Zhao, J. Shi, X. Qi, X. Wang, and J. Jia, "Pyramid scene parsing network," in *2017 IEEE Conference on Computer Vision and Pattern Recognition (CVPR)*, 2017. DOI: 10.1109/CVPR.2017.660.

[131] V. Badrinarayanan, A. Kendall, and R. Cipolla, "Segnet: A deep convolutional encoder-decoder architecture for image segmentation," *IEEE Transactions on Pattern Analysis and Machine Intelligence*, vol. 39, no. 12, pp. 2481–2495, 2017. DOI: 10.1109/TPAMI.2016.2644615.

[132] M. Sandler, A. G. Howard, M. Zhu, A. Zhmoginov, and L.-C. Chen, "Mobilenetv2: Inverted residuals and linear bottlenecks," *2018 IEEE/CVF Conference on Computer Vision and Pattern Recognition*, pp. 4510–4520, 2018.

[133] K. Simonyan and A. Zisserman, "Very deep convolutional networks for large-scale image recognition," in *3rd International Conference on Learning Representations, ICLR 2015, San Diego, CA, USA, May 7-9, 2015, Conference Track Proceedings*, Y. Bengio and Y. LeCun, Eds., 2015.

[134] K. He, X. Zhang, S. Ren, and J. Sun, "Deep residual learning for image recognition," in *2016 IEEE Conference on Computer Vision and Pattern Recognition (CVPR)*, 2016.

[135] M. O'byrne, B. Ghosh, F. Schoefs, and V. Pakrashi, *Image-based Damage Assessment for Underwater Inspections*. CRC Press, Aug. 2018, p. 230. DOI: 10.1201/9781351052580.

[136] FAO, *The State of World Fisheries and Aquaculture 2022. Towards Blue Transformation.* 2022.

[137] D. Jackson, A. Drumm, S. McEvoy, Ø. Jensen, D. Mendiola, G. Gabiña, J. A. Borg, N. Papageorgiou, Y. Karakassis, and K. D. Black, "A pan-European valuation of the extent, causes and cost of escape events from sea cage fish farming," *Aquaculture*, vol. 436, pp. 21–26, 2015. DOI: 10.1016/j.aquaculture.2014.10.040.

[138] Norwegian Directorate of Fisheries, *Rømmingsstatistikk*, 2023.

[139] H. M. Føre and T. Thorvaldsen, "Causal analysis of escape of Atlantic salmon and rainbow trout from Norwegian fish farms during 2010–2018," *Aquaculture*, vol. 532, p. 736 002, 2021. DOI: 10.1016/j.aquaculture.2020.736002.

[140] E. Kelasidi and E. Svendsen, "Robotics for sea-based fish farming," in *Encyclopedia of Smart Agriculture Technologies*, Q. Zhang, Ed. Cham: Springer International Publishing, 2022, pp. 1–20. DOI: 10.1007/978-3-030-89123-7_202-1.

[141] H. Lee, D. Jeong, H. Yu, and J. Ryu, "Autonomous underwater vehicle control for fishnet inspection in turbid water environments," *International Journal of Control, Automation, and Systems*, vol. 20, no. 10, pp. 3383–3392, 2022. DOI: 10.1007/s12555-021-0357-9.

[142] C. Schellewald, A. Stahl, and E. Kelasidi, "Vision-based pose estimation for autonomous operations in aquacultural fish farms," *IFAC-PapersOnLine*, vol. 54, no. 16, pp. 438–443, 2021, 13th IFAC Conference on Control Applications in Marine Systems, Robotics, and Vehicles CAMS 2021. DOI: `10.1016/j.ifacol.2021.10.128`.

[143] V. Chalkiadakis, N. Papandroulakis, G. Livanos, K. Moirogiorgou, G. Giakos, and M. Zervakis, "Designing a small-sized autonomous underwater vehicle architecture for regular periodic fish-cage net inspection," in *Proc. IEEE International Conference on Imaging Systems and Techniques (IST)*, 2017, pp. 1–6. DOI: `10.1109/IST.2017.8261525`.

[144] G. Livanos, M. Zervakis, V. Chalkiadakis, K. Moirogiorgou, G. Giakos, and N. Papandroulakis, "Intelligent navigation and control of a prototype autonomous underwater vehicle for automated inspection of aquaculture net pen cages," in *Proc. IEEE International Conference on Imaging Systems and Techniques (IST)*, 2018, pp. 1–6. DOI: `10.1109/IST.2018.8577180`.

[145] P. Rundtop and K. Frank, "Experimental evaluation of hydroacoustic instruments for ROV navigation along aquaculture net pens," *Aquacultural Engineering*, vol. 74, pp. 143–156, 2016. DOI: `10.1016/j.aquaeng.2016.08.002`.

[146] H. B. Amundsen, W. Caharija, and K. Y. Pettersen, "Autonomous ROV inspections of aquaculture net pens using DVL," *IEEE Journal of Oceanic Engineering*, vol. 47, no. 1, pp. 1–19, 2022. DOI: `10.1109/JOE.2021.3105285`.

[147] E. Kelasidi, B. Su, W. Caharija, M. Føre, M. Pedersen, and K. Frank, "Autonomous monitoring and inspection operations with UUVs in fish farms," *IFAC-PapersOnLine*, vol. 55, no. 31, pp. 401–408, 2022, 14th IFAC Conference on Control Applications in Marine Systems, Robotics, and Vehicles CAMS 2022. DOI: `10.1016/j.ifacol.2022.10.461`.

[148] *SINTEF ACE*, `https://www.sintef.no/en/all-laboratories/ace/`, 2023.

[149] C. Mai, S. Pedersen, L. Hansen, K. L. Jepsen, and Z. Yang, "Subsea infrastructure inspection: A review study," in *2016 IEEE International Conference on Underwater System Technology: Theory and Applications (USYS)*, 2016, pp. 71–76. DOI: `10.1109/USYS.2016.7893928`.

[150] I. Schjølberg, T. B. Gjersvik, A. A. Transeth, and I. B. Utne, "Next generation subsea inspection, maintenance and repair operations," *IFAC-PapersOnLine*, vol. 49, no. 23, pp. 434–439, 2016, 10th IFAC Conference on Control Applications in Marine SystemsCAMS 2016. DOI: `10.1016/j.ifacol.2016.10.443`.

[151] A. G. Rumson, "The application of fully unmanned robotic systems for inspection of subsea pipelines," *Ocean Engineering*, vol. 235, p. 109 214, 2021. DOI: `10.1016/j.oceaneng.2021.109214`.

Part II

Articles

5.3 Conference Papers

5.3.1 Paper A

Application of Maneuvering Based Control for Autonomous Inspection of Aquaculture Net Pens

Alexandre Cardaillac, Herman Biørn Amundsen, Eleni Kelasidi and Martin Ludvigsen

2023 the 8th Asia-Pacific Conference on Intelligent Robot Systems

This paper is not included due to copyright restrictions
available in 8th Asia-Pacific Conference on Intelligent Robot Systems (ACIRS). IEEE
conference proceedings https://doi.org/10.1109/ACIRS58671.2023.10239708

5.3.2 Paper B

Modular Multi-Sensor Fusion for Underwater Localization for Autonomous ROV Operations

Martin Scheiber, Alexandre Cardaillac, Christian Brommer, Stephan Weiss and Martin Ludvigsen

OCEANS 2022, Hampton Roads

This paper is not included due to copyright restrictions
available in OCEANS 2022 Hampton Roads
https://doi.org/10.1109/OCEANS47191.2022.9977298

5.3.3   Paper C

Fusion of Multi-Modal Underwater Ship Inspection Data with Knowledge Graphs

Joseph Hirsch, Brian Elvesæter, Alexandre Cardaillac, Bernhard Bauer, and Maryna Waszak

OCEANS 2022, Hampton Roads

This paper is not included due to copyright restrictions
available in OCEANS 2022 Hampton Roads.
https://doi.org/ 10.1109/OCEANS47191.2022.9977371

5.3.4   Paper D

Marine Snow Detection for Real Time Feature Detection

Alexandre Cardaillac, and Martin Ludvigsen

2022 IEEE/OES Autonomous Underwater Vehicles Symposium (AUV)

This paper is not included due to copyright restrictions
available in
Proceedings of the Symposium on Autonomous Underwater Vehicle Technology
2022 IEEE/OES
https://doi.org/10.1109/AUV53081.2022.9965895

5.3.5 Paper E

A Communication Interface for Multilayer Cloud Computing Architecture for Low Cost Underwater Vehicles

Alexandre Cardaillac, and Martin Ludvigsen

A Communication Interface for Multilayer Cloud Computing Architecture for Low Cost Underwater Vehicles ⋆

Alexandre Cardaillac * Martin Ludvigsen *,**,***

* Department of Marine Technology, Norwegian University of Science
and Technology, Trondheim, Norway (e-mail: {alexandre.cardaillac,
martin.ludvigsen}@ntnu.no).
** Department of Arctic Technology, University Centre in Svalbard,
Longyearbyen, Norway
*** Department for Arctic and Marine Biology, The Arctic University
of Norway, Tromsø, Norway

Abstract: To enable high computational loads for low cost underwater drones, a cloud based
architecture is proposed to take advantage of recent development in machine learning and
computer vision. The processing power made available will benefit vehicles with limited onboard
processing capacity. The rapid development of cloud computing services have made servers with
significant computational resources easier to access. In this paper, a communication interface for
cloud based multilayer architecture is proposed to enable real time performance by distributing
the workload to networked processing devices. It adopts a publish-subscribe model for efficient
communication between the layers. The latency and workload distribution are evaluated to assess
the efficiency of the proposed method. An application to semantic segmentation of under-water
scenes is also tested to measure the framework capabilities for real-time operation using more
resource-demanding tools. The conducted experiments resulted in time and performance gains
through offloading the underwater vehicle, and forwarding the computations to the cloud based
layer.

Keywords: Cloud computing, Underwater vehicles, Multi-layer architecture, Communication
interface, Computer vision

1. INTRODUCTION

Remotely Operated Vehicles (ROVs) allow simple and
efficient underwater operations and are mainly used for
monitoring, exploration and inspection tasks. To automate
the repetitive sub-tasks in subsea inspections, the need
for autonomy increases. However, it is more expensive
in terms of computing power, and many vehicles can
not afford to handle all the processing tasks onboard in
real time. The dampening of electromagnetic signals in
the ocean requires underwater drones to be tethered to
a surface unit for broad band signal transmission. The
processing power of the surface unit can enable a first
sharing of the workload, however, this does not allow full
exploitation of the technological possibilities and modern
techniques for underwater vehicles, including, methods for
vehicle localization, environment mapping or the use deep
learning tools. To overcome this, it is possible to add
cloud based solutions. Cloud servers provide high storage
capacity and significant computational resources, all with
high-bandwidth connections.

This paper presents a communication interface for cloud
based multilayer architecture. It enables low cost underwa-
ter vehicles with limited computing capacity to have access

to more resources in order improve their performance
while in operation. The proposed framework is based on a
publish-subscribe model for connecting sensor data from a
layer to another. Therefore, within each layer it is possible
to select the inputs it should receive and the outputs it will
provide. In this way, only the data necessary for each layer
will be communicated and shared. The number of layers is
adaptable and have bi-directional connections with other
layers following a top-down model of structure of layers.

This publish-subscribe model is beneficial for real-time
robotic applications because they are often event-based.
The traditional approach which has a request-response
model suffers from a higher latency, mainly because of the
polling actions.

2. RELATED WORK

The Internet of Things or IoT, enables the interconnec-
tion of devices through internet or other communications
networks. It facilitates the exchange of data with other
devices or systems inside the network.

In Kamburugamuve et al. (2015), Internet of Things
Cloud is proposed. It is a platform that makes it possible
to connect IoT devices to cloud services for real-time
data processing and control. It is composed of three
main layers which all have their own defined tasks: a

gateway layer, a publish-subscribe messaging layer and a cloud-based big data processing layer. Its scalable and distributed architecture design allows a large number of robots and devices to connect while maintaining a low-latency messaging system.

In Jiao et al. (2017), a robotic cloud-based framework for Visual SLAM (Simultaneous Localization And Mapping) processing of low-cost agents is developed. It enables real-time rate even if the band-width is limited. It uses WebSocket and HTTP as the communication protocols according to the message size which is in a compressed JSON format. The system is based on two components, the robots and a server which internally runs a cloud-based framework and can concurrently process requests from multiple robots at the same time.

In the underwater environment, the IoT, sometimes referred as the Internet of Things Ocean (IoTO) or Internet of Underwater Things (IoUT), is an emerging communication ecosystem to connect underwater agents and gives rise to the concept of Big Marine Data (BMD) because of the increasing volume and availability of data Jahanbakht et al. (2021). It is most of the time used for marine data management Luo et al. (2018); Albaladejo et al. (2010) based on networks of interconnected sensors/devices. These IoT solutions find many applications in marine environment monitoring and protection such as water quality monitoring or coral reef monitoring Xu et al. (2019).

An hybrid use of cloud and edge technologies is proposed in Salhaoui et al. (2020) in order to track the fan mussel population on the seabed in real time. The approach is based on Deep Learning (DL) techniques for image processing techniques such as Convolutional Neural Networks (CNN), which is known to require more computational resources than traditional methods. The solution takes advantage of the resources available thanks to the IoT architecture developed to optimize and improve the vision based method. To achieve this, an Autonomous Underwater Vessel (AUV) is connected to a communication bridge at the surface which is then connected to cloud AI services and a specific platform for AUV operations. The same sort of structures also find applications in autonomous surveillance in marine protected areas Molina Molina et al. (2021).

The proposed framework in this paper enables variable number of processing layers based on the computational load, enabling distributed computing to overcome potential bottle-neck in communication and processing. The tasks of each layer are user defined, allowing a more advanced custom design of the architecture and less requirements to make it possible for the framework to be implemented with a large variety of agents.

3. ARCHITECTURE OVERVIEW

In this section and the followings, all devices/platforms that implement communication interfaces are referred as units or layers in the architecture.

3.1 Communication module design

To maximise its adaptability and scalability, the communication interface is designed to be able to work indepen-
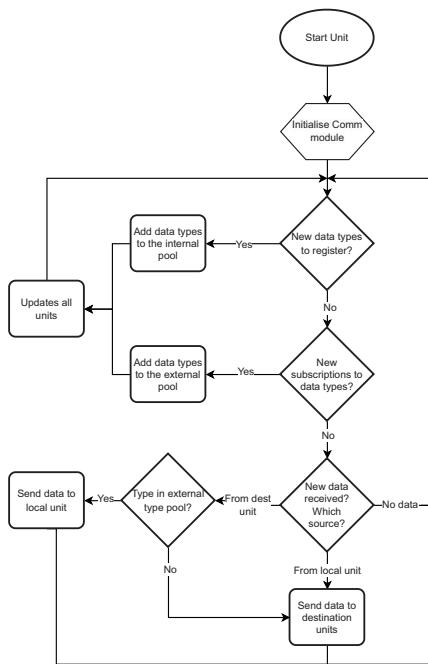
Fig. 1. Flow chart of the communication module.

dently. Therefore, it allows the users to use it with any software or robotic platforms such as ROS Quigley et al. (2009) or DUNE Pinto et al. (2013).

The architecture adopts a publish-subscribe model. To be able to receive and share data with other units, a processing unit will interact with a communication module in order to register and subscribe to data types. For local units subscribing to a data type, the interface saves the transmitted information in a set of data types called external pool along with the unit ID. The updated information distribution scheme is then communicated to all agents in the network. Similarly, when registering a data type, the local unit will assign information to the new data type, and the interface saves it in an other set called internal pool, and updates the other units. In other words, the external pool contains all the data types a unit produces and provides, whereas the internal pool contains the types that are needed for the local processing.

Registrations and subscriptions can be done at any time, enabling new data types to be created during the operation. When the behavior of the units changes during the operation, new subscriptions and registrations can be added to improve the information flow. It enables dynamic adaptation of the units, data requirements and results.

When the communication module receives data, it checks the source, the data type and the associated pool. If the data type is part of the internal pool, the data comes from the local unit and therefore needs to be published in order to communicate it to the other units. When the data comes from another unit, there are two possibilities: either the type is in the external pool, in which case the
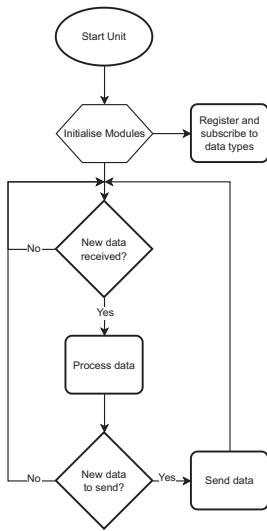
Fig. 2. Flow chart of an unit that interacts with the communication interface.

data is transmitted to the local unit, or, if it is not, it is sent to the next unit, acting like a bridge.

All the above procedures are repeated in a loop according to the received data until the module is stopped. The global design of the communication module is summarised in the flow chart of Figure 1.

A possible interaction between a unit and the communication module is shown in Figure 2. In this example, the registration and subscription procedures of data types are done during the initialisation step. The unit waits to receive data, processes them, and if there are results to send, transmits them to the communication module and starts over.

Making the communication module an independent component enables a higher level of abstraction and ensures reusability. In the example depicted above, the unit only interacts with abstracted functions which makes it impossible for the unit to impact the logical behavior of the module.

The proposed method does not have a limit for the number of layers. However in our application, a minimum of three is required as there must be one layer for the underwater drone, one layer in the cloud and one layer to make the bridge. In Figure 3, the typical architecture, involving three layers is illustrated. To optimally and fully use all the layers, they should all process some data to handle a sub-task in addition to run the communication module. It enables workload distribution, significantly improving the global performance, even for large-scale projects.

3.2 Communication protocols

According to the mission of the drone, the data types and their associated payload of varying sizes will need to be shared between the units. However, communication protocols have size limitations. It is possible to divide the
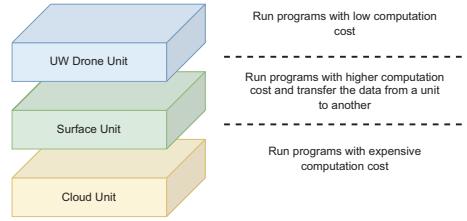
Fig. 3. Framework architecture involving three units.

messages carrying the data into two categories: small messages and large messages. For small messages, WebSockets are used, they are a very good solution for data streaming in real time as they provide full duplex communication channels with low latency. However, they are not well suited to large messages. For larger messages, which correspond to multimedia messages such as, but not limited to, images and sounds, the Real-Time Streaming Protocol (RTSP) is used. This protocol is designed to carry real-time delay-sensitive payloads. It can also stream data from specific sensors of the underwater drone such as sonars.

4. EXPERIMENTS

4.1 Setup

In this section, a series of experiments are described with the main focus on the efficiency and latency of the system. The proposed framework was used in the three-layer architecture presented in Section 3.1. The Blueye Pioneer underwater drone [1] served as UW Unit, containing a single circuit board with a quad core CPU up to 1.2 GHz per core and 4 GB of memory. For the Surface Unit, a laptop was used with an Intel Core i7 vPro with base frequency 1.8 GHz per core and 16 GB of memory. Finally for the Cloud Unit, running on the NTNU IDUN computing cluster Själander et al. (2019), with an Intel Xeon Processor with base frequency 2.2 GHz, 128 GB of memory and an NVIDIA Tesla P100. The underwater drone is tethered to a router to which the laptop is connected over Wi-Fi in a local network. The laptop is also connected to the Internet in order to have access to the cloud server. The implementation of the RTSP is done using the GStreamer framework [2], a pipeline-based multimedia framework that enables streaming workflows.

For all the experiments, each layer has the same communication module but the internal software may differ from one experiment to another.

4.2 Latency Evaluation

To measure the latency of small messages from one unit to another, the average Round Trip Time (RTT) was calculated for each message. This was done in three independent scenarios with message payloads of varying sizes. Each scenario corresponds to a possible route, i.e. from the UW Unit to the Surface Unit (1), from the Surface Unit to the Cloud Unit (2) and from the UW Unit to the Cloud Unit (3). The results are shown in Figure 4. The tested size

---

[1] Blueye, https://www.blueyerobotics.com/
[2] GStreamer, https://gstreamer.freedesktop.org/
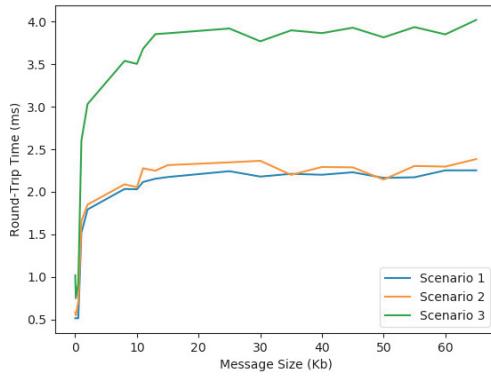
Fig. 4. Round Trip Time of messages of different sizes in three scenarios. Scenario 1: messages between the UW Unit and the Surface Unit. Scenario 2: messages between the Surface Unit and the Cloud Unit. Scenario 3: messages between the UW Unit and the Cloud Unit.

of the messages goes up to 65 Kb as larger messages are considered as media messages.

As expected the third scenario takes twice as long on average as the time of the first and second scenario. It also means that the time needed for a message to change network, i.e. from the local network to the cloud network and vice versa, is extremely low and therefore does not need to be taken into account. It is also possible to observe that the latency in scenario two is on average slightly higher than in scenario one but it is only a matter of tenth of a millisecond. Globally, the latency evaluation shows the viability of the WebSockets in this context for small messages.

The delay for large messages was tested by transmitting video streams from the underwater unit to the surface unit. Four video streams were tested with different combinations of resolution and frame per second (FPS). In Table 1, it is possible to observe the average measured delay and frame per second of video streams from a unit to another using different combinations of resolution and frame per second.

Table 1. Evaluation of communication with video payload

ID	Resolution	Video FPS	Measured FPS	Delay (ms)
1	1280×480	30.0	29.77	42.2
2	1280×480	60.0	57.12	45.2
3	2560×720	30.0	29.64	45.5
4	2560×720	60.0	56.52	47.3

The Video FPS column corresponds to the video streaming source FPS, therefore is the expected FPS, whereas the Measured FPS column corresponds to the FPS at the other end of the streaming pipeline. To ensure a minimum delay, some frames might be dropped because of potential latency in the streaming pipeline on one of the end. To increase the quality of the stream, it is possible to introduce controlled latency, however the global delay of the stream will be increased. In some applications, this does not represent an
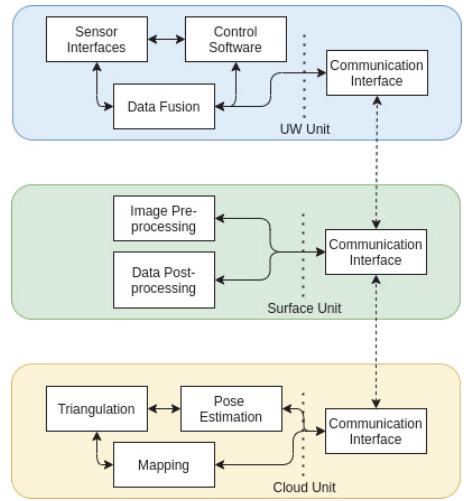
Fig. 5. Software setup for a light Visual SLAM to test the framework. It contains three layers.

issue, or can be easily compensated. This is can be done by adapting the GStreamer pipeline parameters.

The delay here corresponds to the Glass-to-Glass (G2G) measurement, which can be referred as the time it takes for a visible event to go from the glass of a camera to the glass of a display Bachhuber et al. (2017). The measurements were done by aiming the camera at a laptop screen setup to have the same rate as the camera, i.e. 30/60 Hz, which is displaying the video stream. The measured delays are all very close to each other, of about 45ms, although comparing Video 1 and Video 2 allows to spot a difference of 5.1ms which may have an impact on the application over time. Overall, the results show the protocol scale well with the resolution and FPS of the video.

4.3 Efficiency Evaluation

To test how efficient the method is or how it enables more efficient solutions, a special software setup is implemented to match a possible real-world scenario. The Figure 5 represents this setup which is distributed over the three units. It corresponds to a light visual localisation and mapping framework implemented using the OpenCV library OpenCV (2015). The control of the drone is based on PIDs, and two Inertial Measurement Units (IMUs) are used to compute the attitude of the drone based on the filter developed in Madgwick (2010) which is then used to restore the scale of the visual odometry. Each unit has its own set of tasks so that the workload can be shared. In this experiment, the video stream has a resolution of 1080×720 and 30 FPS and continuously ran for about 6 minutes.

Four independent configurations were designed to test and assess the efficiency of the proposed architecture:

- Configuration 1: Everything is running in the Underwater Unit - no communication needed, 0 shared data types.
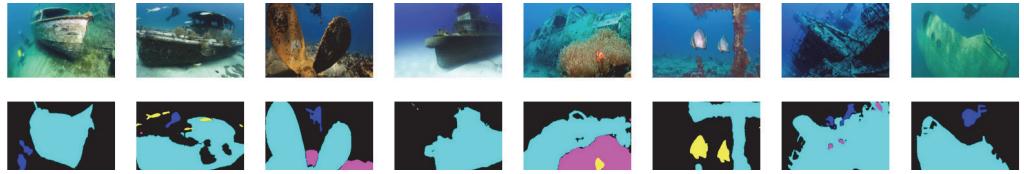
Fig. 6. Set of sample images from SUIM data set Islam et al. (2020), the original images are on the top row and the corresponding pixel-annotations after the SUIM-NET predictions are on the bottom row.
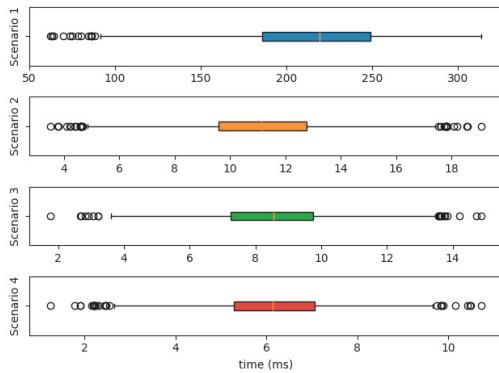
Fig. 7. Processing time benchmark of the developed framework with a three-layers architecture in four scenarios displayed as box-and-whisker diagrams.

- Configuration 2: Control processing and data fusion are done in the Underwater Unit, the rest is done in the Surface Unit - 3 shared data types.
- Configuration 3: The Underwater Unit does the same as in configuration 2. Only data pre-processing and post-processing are done in the Surface Unit, the rest is done in the Cloud Unit, see Figure 5 - 6 shared data types.
- Configuration 4: Same as configuration 3, but the code of the Cloud Unit is optimised to use the available resources in the cloud infrastructure. Additional data processing are done for solution optimisation - 6 shared data types.

The results for each configuration is displayed in Figure 7. The time measured corresponds to the time needed to complete a full loop of the algorithm, including the data communication. In each case, the box-and-whisker diagram is calculated from a sample of 3500 loops. It is clear that the UW Unit alone does not perform well, it can only complete approximately three loops in one second, which makes it not suitable for this type of operation. With the addition of the Surface Unit, the performances are significantly improved and can allow good real-time performances. The third scenario performs similarly but when the resources of the cloud server are used, the algorithm results are similar but it is considerably faster. This gives room to add more features or replace some of the existing features by more computationally expensive ones in order to improve the results. The fourth scenario which includes these changes and is still faster than the other scenarios including better algorithm results.
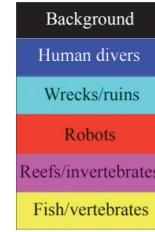
Fig. 8. Corresponding colors to the categories of objects classified by SUIM-NET.

4.4 Application to real time semantic segmentation of underwater scenes

Modern autonomous technologies take advantage of deep learning techniques at an increasing rate, and it is useful to enable real time implementation of the proposed framework. For this, SUIM-Net and the associated data set Islam et al. (2020) were used. It consists of a fully-convolutional encoder-decoder model trained for semantic segmentation of underwater images. It allows to detect five categories of objects: human divers, wrecks and ruins, robots and instruments, reefs and invertebrates, fish and vertebrates. This deep learning solution was chosen because, firstly, it requires computational resources that not all the platforms have, and secondly, because it can be used in multiple applications in the field of underwater robotic vision which makes it a tool to improve the performance and autonomy of an underwater vehicle. It can be integrated into the complete robotic system in order to solve or contribute to tasks such as visual tracking, scene understanding and autonomous exploration. These tasks have to be able to run the model with low-latency. The lower the latency, the more images will be processed and therefore more data will be available, enabling potentially a deeper and more accurate analysis for a given task.

To test the proposed cloud based architecture, the same three layers were deployed and the sub set of the data set used for model testing was used to simulate a real-time feed of images coming from the drone through the surface unit in order to be inferred by the artificial neural network located in the cloud unit. For comparison, the model also ran independently in the surface unit, reducing the global architecture to a two-layers structure.

Although the execution speed are different according to the unit, the result for a same given image remains the same. With the cloud unit, it was possible to run the model with on average 24.23 frames per second which makes it possible to run it in real time and use it for visual aid and/or visual-guided navigation. However, on the surface

unit, it reached 2.5 frame per second on average which is about 10 times less than the previous test. This highlight the use of the previous setup and how important it can be, especially because drone operators do not often have a laptop with a graphical card at hand. A sample of images and their corresponding semantic segmentation predicted by SUIM-NET is displayed in Figure 6. The color code is presented in Figure 8.

5. DISCUSSION

The proposed communication interface for a multilayer structure showed satisfying results for real-time operations of underwater vehicles. The implementation of the communication interface makes it easy to use and adapt, and enables the user to add middleware. It enables quick deployment of additional layers for independent processing and further workload sharing.

However, the current implementation only allows a two-links top-down structure of layers which means that each layer can only be connected to the previous and next layers if they exist. It has the benefits of incremental functionalities, i.e. as the data moves down or top, it produces new results on top of the previous ones. It also allows a clear understanding of the structure and the dependencies of each unit. The main drawback of this type of structure is that it may introduce additional delays for each layer. If the ultimate functionality is located in the last layer, it might take more time, especially if the results need to be sent back to the first layer. Fortunately, these delays can be distributed and dispersed according to the design and locations of the functionalities in the layers.

While this method enables low-latency communications for messages of variable size, which are important for real time operations, it involves risks for the multimedia payloads. Indeed, the protocol used for this type of payload, RTSP, relies on UDP and can lead to packet loss. If important packets are lost, it may affect significantly the behaviour of the implemented algorithms.

Although the framework was experimented using a local computer and with cloud computing, it is possible to imagine alternatives, such as edge computing with different sensors/agents setups. For example an underwater agent connected to a buoy which is itself connected to a surface vessel. Also, despite the fact that the proposed method is used for underwater applications, it can be used for other categories of devices/robots such as ground vehicles.

6. CONCLUSION AND FUTURE WORK

In this paper, a communication interface for cloud based multilayer architecture was developed. It is based on a publish-subscribe model with a topic system to enable clear and effective communication between the units. The access to other units also enables work load distribution according to the resources available. With this architecture, low cost underwater agents with reduced computational capabilities are able to operate in real-time using advanced tools which require important resources.

Future work includes study of how this architecture can scale to cooperative missions involving multiple underwa-

ter drones and how the work load can be further distributed to reduce the software latency. This corresponds also to a study of how the layers can be inter-connected, adopting a more complex distributed structure.

REFERENCES

Albaladejo, C., Sanchez, P., Iborra, A., Soto, F., López, J., and Torres, R. (2010). Wireless sensor networks for oceanographic monitoring: A systematic review. *Sensors (Basel, Switzerland)*, 10, 6948–68. doi: 10.3390/s100706948.

Bachhuber, C., Steinbach, E., Freundl, M., and Reisslein, M. (2017). On the minimization of glass-to-glass and glass-to-algorithm delay in video communication. *IEEE Transactions on Multimedia*, PP, 1–1. doi: 10.1109/TMM.2017.2726189.

Islam, M.J., Edge, C., Xiao, Y., Luo, P., Mehtaz, M., Morse, C., Enan, S.S., and Sattar, J. (2020). Semantic segmentation of underwater imagery: Dataset and benchmark.

Jahanbakht, M., Xiang, W., Hanzo, L., and Rahimi Azghadi, M. (2021). Internet of underwater things and big marine data analytics—a comprehensive survey. *IEEE Communications Surveys Tutorials*, 23(2), 904–956. doi:10.1109/COMST.2021.3053118.

Jiao, J., Yun, P., and Liu, M. (2017). A cloud-based visual slam framework for low-cost agents. 471–484. doi: 10.1007/978-3-319-68345-4_2.

Kamburugamuve, S., Christiansen, L., and Fox, G. (2015). A framework for real time processing of sensor data in the cloud. *Journal of Sensors*, 2015, 1–11. doi: 10.1155/2015/468047.

Luo, H., Wu, K., Ruby, R., Liang, Y., Guo, Z., and Ni, L.M. (2018). Software-defined architectures and technologies for underwater wireless sensor networks: A survey. *IEEE Communications Surveys Tutorials*, 20(4), 2855–2888. doi: 10.1109/COMST.2018.2842060.

Madgwick, S. (2010). An efficient orientation filter for inertial and inertial / magnetic sensor arrays.

Molina Molina, J., Salhaoui, M., González, A., and Arioua, M. (2021). Autonomous marine robot based on ai recognition for permanent surveillance in marine protected areas. *Sensors*, 21, 2664. doi:10.3390/s21082664.

OpenCV (2015). Open source computer vision library.

Pinto, J., Dias, P.S., Martins, R., Fortuna, J., Marques, E., and Sousa, J. (2013). The lsts toolchain for networked vehicle systems. In *2013 MTS/IEEE OCEANS - Bergen*, 1–9. doi:10.1109/OCEANS-Bergen.2013.6608148.

Quigley, M., Conley, K., Gerkey, B., Faust, J., Foote, T., Leibs, J., Wheeler, R., and Ng, A. (2009). Ros: an open-source robot operating system. volume 3.

Salhaoui, M., Molina Molina, J., González, A., Arioua, M., and Ortiz, F. (2020). Autonomous underwater monitoring system for detecting life on the seabed by means of computer vision cloud services. *Remote Sensing*, 12, 1981. doi:10.3390/rs12121981.

Själander, M., Jahre, M., Tufte, G., and Reissmann, N. (2019). EPIC: An energy-efficient, high-performance GPGPU computing research infrastructure.

Xu, G., Shi, Y., Sun, X., and Shen, W. (2019). Internet of things in marine environment monitoring: A review. *Sensors*, 19(7). doi:10.3390/s19071711. URL https://www.mdpi.com/1424-8220/19/7/1711.

5.3.6 Paper F

Path Following for Underwater Inspection Allowing Manoeuvring Constraints

Alexandre Cardaillac, and Martin Ludvigsen

Intelligent Autonomous Systems 17

Path Following for Underwater Inspection Allowing Manoeuvring Constraints

Alexandre Cardaillac[1]([✉]) and Martin Ludvigsen[1,2,3]

[1] Department of Marine Technology, Norwegian University of Science and Technology, Trondheim, Norway
{alexandre.cardaillac,martin.ludvigsen}@ntnu.no
[2] Department of Arctic Technology, University Centre in Svalbard, Longyearbyen, Norway
[3] Department for Arctic and Marine Biology, The Arctic University of Norway, Tromsø, Norway

Abstract. A guidance system is proposed for underwater navigation and inspection of structures to enable path-following control objectives with manoeuvring constraints such as velocity and orientation instructions. To document a vertical surface like a ship hull, a submerged drone will take benefit of maneuvering with the heading perpendicular object, while during transit the most efficient would be to align the heading towards the next way point. The proposed system is simulated using a small underactuated Remotely Operated underwater Vehicle (ROV) with control in surge, sway, heave and yaw (4 DOF). It is based on the Line Of Sight (LOS) steering laws and PID controllers for the 4 DOF motion control. The waypoints are generated together with a list of instructions for orientation and velocity for the ROV using the Parametrised Rapidly exploring Random Graph (PRRG). The LOS vector is used for heading control during transit whereas during inspection, it is used for course control. The proposed framework is tested in simulation to follow 3D straight lines in a lawnmower pattern and a typical path for ship hull inspection. Simulations shows that the paths generated using the proposed solution are viable for inspection tasks taking into account the manoeuvring constraints posed by the inspection mission and the properties of the vehicle.

Keywords: Line of sight guidance · 3D path-following · Inspection · Remotely operated underwater vehicle · Control system

1 Introduction

In the maritime industry, inspections of ship hulls and submerged installations are often done with divers. Some structures require regular supervision and can be difficult to access. Inspections are often required to guaranty the safety and integrity of the structure. This is a repeated task that often require human intervention.

Using a Remotely Operated underwater Vehicle (ROV) can help reduce risks for human operators and divers. ROVs can be deployed with a simple set up. They can also be used for underwater inspection of ship hulls, and in some cases to avoid expensive dry docking. The vehicle can fly around the hull for visual inspection and determine whether maintenance is required. Such inspection tasks can be automated, reducing human interventions. To enable autonomous ROV-based ship hull inspections, multiple dedicated systems need to be developed including mission planning, path planning and control.

This paper presents a method for path following with constraints to enable visual inspection of underwater structures. The paths are planned based on the Parametrised Rapidly exploring Random Graph (PRRG) presented in [4] with two types of paths according to the steps of the mission: transit and inspection. For inspection missions, transit paths are defined to bring the vehicle in position for the observation, while inspection paths define the maneuver during the actual survey. The optimal and possible velocity will depend on the quality of the acquired optical or acoustical data and the hydrodynamic parameters of the vehicle and vary between transit lines and inspection lines. This online 3D path-planning module generates a set of waypoints which contains instructions for orientation and velocity for the ROV.

The proposed system is tested in a simulation environment with two missions designs. The first one is based on a lawnmower pattern composed of four rows and the second one is a path following simulation for the inspection of one side of a ship.

The combination of the proposed path following system and the previously developed path planning framework makes it possible to perform efficiently inspection missions which may contain constraints and requirements.

For path following, straight-lines are considered, and the Line-Of-Sight (LOS) steering law is applied for both course control and heading control according to the type of path and the constraints in a 3-D decoupled motions design inspired by [10]. When following transit paths, the LOS law is extended by adding integral action of a function of the cross track error as modelled in [11]. The surge, sway and yaw motions is controlled based on the instructions received from the horizontal LOS model whereas the heave motion is based on a desired underwater depth at which the trajectory should be followed. The LOS is a popular method which is known to be stable and effective with a simple design. It is largely used in underwater applications [8,12,13].

2   Modelling of the ROV

For the numerical simulation, the drone is modelled based on the 6 DOF model for ROV provided in [7]. The 6 DOF nonlinear equations of motion can be written as,

$$\dot{\eta} = J_{\Theta}(\eta)\nu \tag{1}$$

$$M\dot{\nu} + C(\nu)\nu + D(\nu)\nu + g(\eta) = \tau \tag{2}$$

where $M \in \mathcal{R}^{6\times6}$ is the system inertia matrix from the addition of the rigid body and added mass inertia matrix $M = M_{RB} + M_A$. $C \in \mathcal{R}^{6\times6}$ represents Coriolis and centrifugal forces similarly based of the rigid body and added mass. $D \in \mathcal{R}^{6\times6}$ is the damping matrix, $g(\eta) \in \mathcal{R}^6$, the vector of restoring forces and moments and $\tau \in \mathcal{R}^6$, the vector of generalized forces. The velocity vector $\nu = [u, v, w, p, q, r]^T$ is in the drone body frame and its position $\eta = [x, y, z, \phi, \theta, \psi]^T$ is in the NED frame based on the rotation matrix $J_\Theta(\eta)$ from body-fixed to NED frame.

3   Path Planning

Planning a path is primordial to execute a mission. If it has online capabilities, it makes it more efficient in order to plan safe path that can adapt to the changes in the environment. For underwater drones, the planned paths need to be in the 3D space.

The proposed guidance system utilizes the Parametrised Rapidly exploring Random Graph (PRRG) [4] which is a sampling based planner with efficient real time capabilities. The large set of parameters proposed makes it possible to easily adapt it to any mission. It includes parameters such as the minimum and maximum distance of a path segment, obstacle inflation radius, about node neighboring management, and a set of rules for specific customisation of the planning graph. The Dijkstra search algorithm [5] is employed in this paper to find a path in the graph. This framework also proposes a rule system for dynamic node management. It is employed to generate two types of paths: transit paths, which correspond to the paths the drone will have to follow to reach the target of the mission, and inspection paths, to carry out the inspection mission.

This path planning framework allows an easier and more adaptable creation of inspection routes as it can take into account the vehicle parameters and inspection criteria.

When the final path is computed, each attached node receives a list of guidance instructions that will be shared with the drone when it reaches the point. All of them contain at least the guidance mode. Transit paths can be free of constraints, but still receive instruction about the LOS vector and waypoint management that will be explained in more details in their dedicated sections. On the contrary, for inspection paths, constraints are frequently included. The most common constraints are related to the drone's velocity and heading because they can have an important impact in the inspection results. The 3D waypoints of the planned path are then used as reference positions that the ROV will have to go through. The waypoint set is defined as,

$$\text{WP} = [\text{WP}_1, \text{WP}_2, \text{WP}_3, \ldots, \text{WP}_n] \tag{3}$$

$$\text{WP}_k = [x_k, y_k, z_k]^T \tag{4}$$

where WP_k is the last waypoint reached by the vehicle and WP_{k+1} the target. The list of instructions that the waypoint contains is of variable size, and a

typical set can be defined as,

$$S_k = (\Delta_k, \psi_k, d_{hk}, d_{vk}) \tag{5}$$

with Δ_k, ψ_k, d_{hk} and d_{vk} respectively the lookahead distance, desired heading, horizontal acceptance distance and vertical acceptance distance.

4   Path Following

4.1   Objective

The path following objective is to converge to and follow the desired path which is represented as a set of 3D straight lines.

Given the vehicle position $P = [x, y, z]^T$ and WP_k the last waypoint it has reached, the along-track error x_e and the cross-track error y_e can be calculated as,

$$\begin{bmatrix} x_e \\ y_e \end{bmatrix} = R^T(\gamma_p) \begin{bmatrix} x - x_k \\ y - y_k \end{bmatrix} \tag{6}$$

where $R^T(\gamma_p)$ is defined as,

$$R^T(\gamma_p) = \begin{bmatrix} \cos(\gamma_p) & -\sin(\gamma_p) \\ \sin(\gamma_p) & \cos(\gamma_p) \end{bmatrix} \tag{7}$$

and γ_p is the horizontal path-tangential angle,

$$\gamma_p = \mathrm{atan2}(y_{k+1} - y_k, x_{k+1} - x_k) \tag{8}$$

Regarding the error in depth, the direct depth measurements are used and is therefore defined as,

$$z_e = z - z_{k+1} \tag{9}$$

The path tracking control objective is therefore to minimize the error $e(t) = [x_e(t), y_e(t), z_e(t)]^T$ over time (10) by applying guidance laws.

$$\lim_{t \to \infty} e(t) = 0 \tag{10}$$

Figure 1 represents the geometry used for the path following system.

4.2   Guidance Law

For path following in the horizontal plane, the LOS guidance law is applied using the lookahead-based version. According to the scenario, it is used for course control or augmented with integral action for heading control. In both cases, the lookahead distance Δ is provided by the mission handler which extract it from the waypoint properties. Based on [2,3], the lookahead-based guidance law can be given by,

$$\psi_d = \gamma_p + \arctan\left(\frac{-y_e}{\Delta}\right) \tag{11}$$
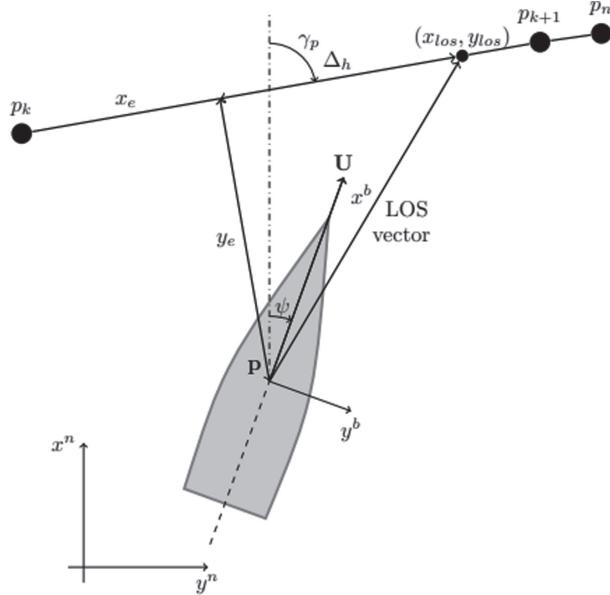
Fig. 1. Horizontal line of sight guidance for straight lines [10].

$$\chi_d = \psi_d \tag{12}$$

It defines the desired heading angle ψ_d and desired course angle χ_d with γ_p the horizontal path-tangential angle and y_e the cross-track error which needs to be minimized. However, the two angles are not always aligned, when the drone is turning, or because of the conditions in water, therefore,

$$\chi_d = \psi_d + \beta \tag{13}$$

where ψ_d and χ_d are related by the sideslip angle β that can be viewed as the angle between the orientation of the global velocity of the vehicle and its heading. It is defined as,

$$\beta = \arcsin\left(\frac{v}{U}\right) \tag{14}$$

where v is the sway velocity and U the total velocity of the ROV. In the presence of external forces, such as currents, the relative velocities need to be considered. However, calculating this drift angle based on direct measurements will results in small offsets and singularities at zero speed. Therefore, for transit paths, even though the sideslip angle can be assumed to be small, the Integral LOS guidance is applied, defined as in [11]:

$$\psi_d = \gamma_p - \arctan\left(\frac{y_e + \kappa y_{int}}{\Delta}\right) \tag{15}$$

$$\dot{y_{int}} = \frac{U y_e}{\sqrt{\Delta^2 + (y_e + \kappa y_{int})^2}} \tag{16}$$

with $\kappa > 0$, a tuning parameter. It makes the system capable of removing the cross-track error caused by external disturbances.

For inspection paths, conventional LOS is applied for course control and the desired heading is set according to the constraint contained in the last waypoint the drone has reached.

$$\psi_d = \psi_k \tag{17}$$

$$\chi_d = \gamma_p + \arctan\left(\frac{-y_e}{\Delta}\right) \tag{18}$$

which means the difference between the heading constraint and the desired course angle that points towards the LOS point should match the orientation difference β.

The choice of the lookahead distance Δ is very important as it can impact significantly the maneuvering characteristics of the drone. A low distance value can result in more aggressive steering compared to a larger value [10] which can be useful for a large cross-track error. On the contrary a high distance value will smooth out the steering and reduce oscillatory movements which is convenient when the error is small. For this reason, it can be practical to have a distance value Δ that varies. If the lookahead distance is defined in the waypoint properties as a set of two different values, the Time-Varying Lookahead Distance $\Delta(y_e)$ [9] is utilized. It is defined as,

$$\Delta(y_e) = (\Delta_{max} - \Delta_{min})e^{\gamma_r|y_e|} + \Delta_{min} \tag{19}$$

where Δ_{max} and Δ_{min} are the minimum and maximum values that Δ can adopt, and $\gamma_r > 0$ is the convergence rate. It allows to adopt a more flexible behavior which contributes to faster convergence to the desired path and reduced the oscillations around the path.

For vertical guidance, the desired depth z_d is the corresponding depth of the closest point to the vehicle on the reference line such that,

$$P_{proj} = \mathrm{WP}_k + ((P - \mathrm{WP}_k) \cdot n) \circ n \tag{20}$$

$$z_d = P_{proj\_z} \tag{21}$$

with P_{proj} the projected position on the reference line and n the normalized vector of the reference line:

$$n = \frac{WP_{k+1} - WP_k}{||WP_{k+1} - WP_k||} \tag{22}$$

The vehicle is considered to have reached the waypoint when it has entered the acceptance area which is defined according to an horizontal and vertical distance, d_{hk} and d_{vk}. If a heading constraint is present, it also need to be satisfied before moving to the next waypoint.

5   Control System

Surge, sway, heave and yaw, are controlled using Proportional Integral Derivative (PID) controllers. However, for the surge and sway, additional processing is performed to ensure the safety and successful completion of the operation. The resulting vector of desired forces and moments $\tau = [\tau_X, \tau_Y, \tau_Z, \tau_N]$ is based on the vector of error $\epsilon = [\epsilon_x, \epsilon_y, \epsilon_z, \epsilon_\psi]^T$ where the error components are defined as,

$$\epsilon = \begin{bmatrix} \epsilon_x \\ \epsilon_y \\ \epsilon_z \\ \epsilon_\psi \end{bmatrix} = \begin{bmatrix} x_d - x(t) \\ y_d - y(t) \\ z_d - z(t) \\ \psi_d - \psi(t) \end{bmatrix} \tag{23}$$

All controllers have their own set of gains including the proportional, integral and derivative gains, K_p, K_i and K_d. They were experimentally tuned.

The heading controller which provides the desired yaw moment to reach the desired heading is formulated as,

$$\tau_N = K_p \epsilon_\psi + K_i \int \epsilon_\psi dt + K_d \dot{\epsilon}_\psi \tag{24}$$

Similarly for the depth controller but with desired heave force,

$$\tau_Z = K_p \epsilon_z + K_i \int \epsilon_z dt + K_d \dot{\epsilon}_z \tag{25}$$

Regarding, the surge and sway controllers, a dynamic force limit is considered. For this, multiple conditions need to be taken into account. First, if the heading and depth errors are below the accepted error $\delta \in \mathcal{R}_{>0}^2, \delta = [\delta_z, \delta_\psi]^T$, the commanded force can be up to the maximum allowed force τ_{max}. It is important to consider the error in depth and heading since they are both important criteria for the inspection. Also, too large errors may result in a 3D drift from the reference trajectory if not compensated. To avoid situations were high forces for sway and surge are combined with large deviation terms for depth and heading a reduction term is introduced defined by λ.

$$|\epsilon_z| \le \delta_z \tag{26}$$

$$|\epsilon_\psi| \le \delta_\psi \tag{27}$$

If at least one of these values is exceeded, an unique ratio λ is calculated so that the allowed maximum forces for surge and sway decrease as the error increases. It is formulated as an exponential function as follows:

$$\lambda = e^{\delta_r \ln(\gamma_e)} \tag{28}$$

where δ_r is the total residual error defined as,

$$\delta_r = \begin{cases} |\epsilon_z| - \delta_z & \text{if } |\epsilon_z| > \delta_z \wedge |\epsilon_\psi| \le \delta_\psi \\ |\epsilon_\psi| - \delta_\psi & \text{if } |\epsilon_z| \le \delta_z \wedge |\epsilon_\psi| > \delta_\psi \\ |\epsilon_z| - \delta_z + |\epsilon_\psi| - \delta_\psi & \text{if } |\epsilon_z| > \delta_z \wedge |\epsilon_\psi| > \delta_\psi \end{cases} \tag{29}$$

γ_e, with $0 < \gamma_e < 1$, is the convergence rate. A γ_e close to 1 will result in a slow convergence towards 0 whereas a γ_e close to 0 will result in a fast convergence. If the tuning parameter $K_\gamma = 0.01$ is considered as a value close enough to the exponential plateau of (28), a good value of γ_e can be approximated as,

$$\gamma_e = e^{\frac{\ln (K_\gamma)}{\delta_z + \delta_\psi}} \tag{30}$$

It is important to note that if the vehicle is slow to reduce the error whether it is because of external forces or how the vehicle functions or other reasons, the approximation of the plateau should be decreased. On the contrary, if the vehicle is fast to minimize the error, it can be increased.

The resulting maximum allowed surge and sway forces can therefore be defined as follows:

$$\tau_{max\_capped} = \begin{cases} \tau_{max} & \text{if } |\epsilon_z| \leq \delta_z \wedge |\epsilon_\psi| \leq \delta_\psi \\ \lambda(\delta_r)\tau_{max} & \text{otherwise} \end{cases} \tag{31}$$

with τ_{max} the vector containing the original maximum force allowed as a percentage in surge and sway such that,

$$\tau_{max} = \begin{bmatrix} \tau_{max\_X} \\ \tau_{max\_Y} \end{bmatrix} \tag{32}$$

Both surge and sway controllers are PIDs that include the previous characteristics. By default, they are based on the horizontal errors ϵ_x and ϵ_y,

$$\tau_X = K_p\epsilon_x + K_i \int \epsilon_x dt + K_d\dot{\epsilon}_x \tag{33}$$

$$\tau_Y = K_p\epsilon_y + K_i \int \epsilon_y dt + K_d\dot{\epsilon}_y \tag{34}$$

However, in the presence of velocity instructions and/or constraints, the PIDs are based on desired velocities instead of desired positions.

6   Simulation

6.1   Setup

The simulation is based on the Robot Operating System (ROS) [14] using a python simulation node provided by Blueye Robotics [1] to simulate their underwater drones such as the one presented in Fig. 2. The simulated vehicle is a Pioneer X3 developed by Blueye Robotics. It is a 4 DOF vehicle, actuated for surge, sway, heave and yaw. There are two thrusters in the surge direction, one lateral and one vertical. The vehicle is equipped with pressure sensor for depth estimation, and IMU for heading. The vehicle also supports USBL and DVL navigation systems providing measurements of positions and velocities. For roll

and pitch angle, the drone is kept passively stable by the separation of centre of gravity and centre of buoyancy. The two different patterns, both constructed from straight lines, was tested, a lawnmower pattern and an inspection pattern. The former includes six rows of 10 m each, separated from each other by a distance of 2 m. The first half of the pattern, i.e. the first three rows, are free of constraints and are considered as transit path. The last three are considered as inspection path with heading constraints. The latter pattern resembles an inspection of the side a small ship hull, considering also the navigation to the beginning of the inspection route.

Fig. 2. Blueye X3 ROV [1].

For both simulations, the same variables defining the guidance and control systems are used and presented in Table 1.

Table 1. Table of variables used during the simulations.

Name	Parameter	Value
Lookahead distance (m)	$(\Delta_{min}, \Delta_{max})$	(0.8, 2.0)
LOS convergence rate	γ_r	1.3
Integral gain parameter	κ	0.1
Horizontal acceptance distance (m)	d_{hk}	0.2
Vertical acceptance distance (m)	d_{vk}	0.35
Accepted heading error (deg)	δ_ψ	4.0
Accepted depth error (m)	δ_z	0.5
Exponential convergence rate	γ_e	0.77
Starting position (m, deg)	$(x, y, z, \phi, \theta, \psi)$	(0, 0, 2, 0, 0, 0)

6.2   Lawnmower Pattern

With this pattern the goal is to test a typical path often used for surveys of areas. To test the proposed system, it is divided in two parts, using line of sight for heading control for the first part, and course control for the second part.

The constraints requested by the waypoints of this last part are related to the heading, the underwater drone has to follow the line while being perpendicular to it, therefore moving sideways.

(a)   (b)
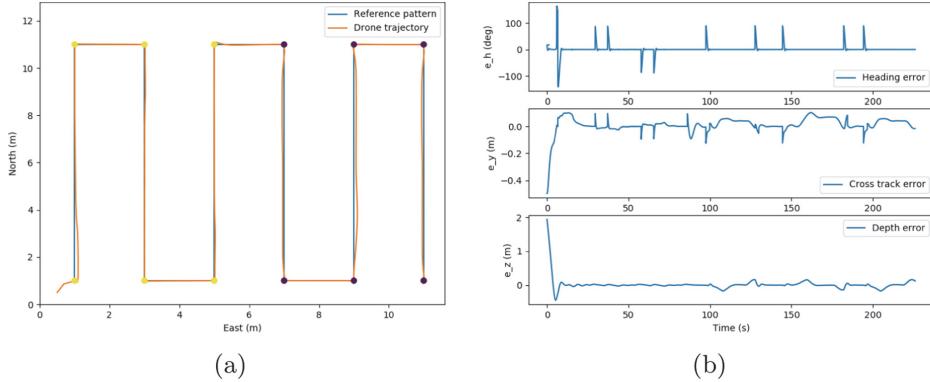
Fig. 3. Results of the framework with the lawnmower pattern. (a) shows the trajectory of the underwater drone following a lawnmower pattern in the horizontal plane. The dots represent the waypoints and their color, the guidance mode they contain. Yellow for transit, black for inspection. (b) shows the errors recorded over time while the drone is following the path. From top to bottom, the heading error ϵ_ψ, cross track error y_e and depth error ϵ_z.

With this pattern, the desired depth is constant at 4 m deep. So only at the beginning of the operation a notable change in depth is expected as the drone starts at 2 m depth.

The results of the mission are presented in Fig. 3a and b. In the first Figure, the dots represent the waypoints, and their color represents their status, i.e. transit (yellow) or inspection (black) path.

It is possible to observe that the mission is carried out successfully. The desired heading and depth are quickly reached, the errors grow larger only during the transitions, i.e. change of targeted waypoint and/or constraints, which is expected. Over the complete duration of the operation, the system successfully maintained the cross track error close to 0.

It took the drone more time to complete the second part that the first, about 80 s for the first and about 180 s for the second part. This was expected since the drone is moving slower sideways due to larger drag forces and lower thrust force in the lateral direction.

6.3   Inspection Pattern

In this case, the goal is to test a simplified version of an inspection route for ship hull inspection. Only one side of the hull is considered. The path is divided again into two parts, first navigating to the beginning of the inspection route and then completing the inspection path.

(a)

(b)   (c)
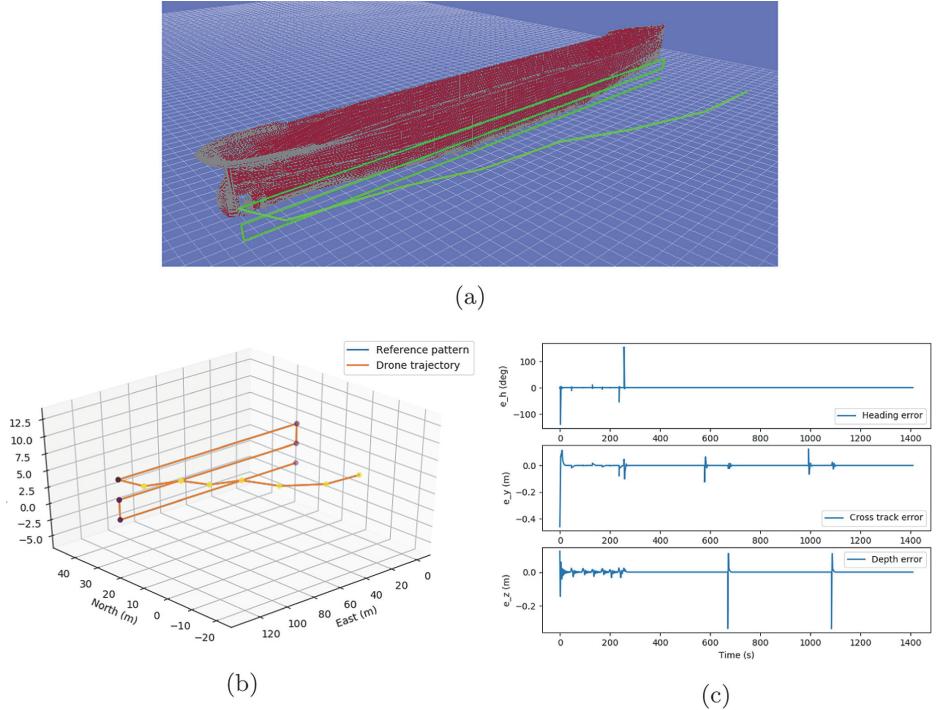
Fig. 4. Results of the simulation of an underwater ship hull inspection. (a) shows the planned path using PRRG to inspect the ship. (b) shows the 3D trajectory of the underwater drone, moving to the beginning of an inspection route and following it. The spheres represent the waypoints and their color, the guidance mode they contain. Yellow for transit, black for inspection. And (c) shows the errors recorded over time while the drone is following the path. From top to bottom, the heading error ϵ_ψ, cross track error y_e and depth error ϵ_z.

The second part is a vertical lawnmower pattern composed of three rows of 132 m separated from each other by a distance of 3 m. While the drone is following this pattern, the heading is kept perpendicular to the lateral direction of motion, simulating the drone facing the ship hull for visual inspection.

This simulation is based on the scenario developed in [4], using PRRG to create a planning graph around the ship and calculate a collision-free path under constraints to safely execute the path. This framework enables fast online replanning for collision avoidance and/or in case there is a change in the mission plan.

For this simulation the depth is slowly increasing from the beginning of the transit path until its end. The next section of the simulation has also varying depth from 0.6 m depth to 6.6 m. The inspection lines are either vertical or horizontal.

The 3D trajectory of the underwater drone can be observed in Fig. 4b and the errors related to the heading, cross track error and depth are presented in Fig. 4c.

The system performed as good as in the previous simulation. More variations in the depth error were recorded but still remain in an acceptable range.

7   Discussion

Based on the two simulations experimented, the proposed system for the Blueye ROV has proven its efficiency, and made it possible to exploit the high maneuverability capabilities offered by this drone. It was however tested considering a calm environment, but environmental loads, especially the water current, need to be taken into account to develop a robust system. Even though the proposed system should be able to scale to this problem, it needs to be tested.

The proposed force limit has its role to play in this situation and helps attenuate and potentially prevents horizontal drift when the error in heading and/or depth grows. This ensures that the drone does not deviate too far from the initial trajectory by proportionally reducing its potential speed in surge and sway while the errors are being corrected. This makes it possible to maintain the drone in its last valid position. Being able to perform sway motions is advantageous in that regard. Higher priorities are set for the depth and heading because of their importance in inspection missions. Additionally, with a guidance system based on the LOS laws, it is essential to have a correct heading in order to achieve good performance.

Despite the fact that features requiring additional processing were included, such as the time varying lookahead distance, integral action for the desired heading and the force limit ratio, the processing complexity and time remain low which is important for real time applications and onboard processing with low computational capacity vehicles.

The time varying lookahead distance allowed a more stable system and reduced significantly the oscillations around the path while keeping the possibility for a short lookahead distance.

Thanks to the proposed combination of the guidance system and the path planning framework, it was possible to successfully perform an inspection mission with heading constraints to visually inspect the ship's hull. However, the possibilities offered by the rule system of the planner and the guidance instructions system were not fully exploited here as only the line of sight instructions and heading constraints were considered during the simulations.

Conventional PID controllers were implemented and could benefit some improvement, especially for the depth controller which can have difficulties to maintain the desired depth in some conditions.

A specific reference model such as [6] could also help improve the solution, especially when taking into account multiple constraints.

8   Conclusion

In this paper, a 3D path following system of straight line was presented. It is based on the horizontal lookahead based line of sight guidance law which

is utilized for heading control and course control according to the presence of heading constraints. For heading control, Integral LOS was applied to improve the stability of the trajectory of the drone. To further improve it, the time varying lookahead distance was included together with a dynamic surge and sway force limit ratio.

The simulations proved the potential of this method when combined with the PRRG for inspection tasks which require for example visual feedback. And will be developed further for that purpose.

For future work, environmental loads will be considered and the system will be tested in real world conditions in the context of ship hull inspection.

The guidance system will be augmented with a constant jerk reference model [6], which is an alternative to filter based reference models. It provides a desired velocity and position by integrating of a constant jerk which is on or off. Improvements of the PID controllers will also be considered, including the addition of acceleration feedbacks.

References

1. Blueye robotics. https://www.blueyerobotics.com/
2. Breivik, M., Fossen, T.: Principles of guidance-based path following in 2D and 3D. In: Proceedings of the 44th IEEE Conference on Decision and Control, pp. 627–634 (2005)
3. Breivik, M., Fossen, T.: Guidance Laws for Autonomous Underwater Vehicles (2009)
4. Cardaillac, A., Ludvigsen, M.: Ruled path planning framework for safe and dynamic navigation. In: Global Oceans 2021, San Diego, pp. 1–7 (2021)
5. Dijkstra, E.W.: A note on two problems in connexion with graphs. Numer. Math. **1**(1), 269–271 (1959)
6. Dukan, F.: ROV Motion Control Systems (2014)
7. Fossen, T.: Handbook of Marine Craft Hydrodynamics and Motion Control, Chap. 7, pp. 133–186. Wiley (2011)
8. Haugaløkken, B.O., Lekkas, A., Schjølberg, I.: 3D Path Following and Tracking for an Inspection Class ROV, p. V07AT06A019 (2017)
9. Lekkas, A., Fossen, T.: A time-varying lookahead distance guidance law for path following. IFAC Proc. Vol. **45**, 398–403 (2012)
10. Lekkas, A., Fossen, T.: Line-of-Sight Guidance for Path Following of Marine Vehicles (2013)
11. Lekkas, A.M., Fossen, T.I.: Integral LOS path following for curved paths based on a monotone cubic hermite spline parametrization. IEEE Trans. Control Syst. Technol. **22**(6), 2287–2301 (2014)
12. Molnar, L., Omerdic, E., Toal, D.: Guidance, navigation and control system for the tethra unmanned underwater vehicle. Int. J. Control **80**(7), 1050–1076 (2007)

13. Nie, W., Feng, S.: Planar path-following tracking control for an autonomous underwater vehicle in the horizontal plane. Optik **127**(24), 11607–11616 (2016)
14. Quigley, M., Conley, K., Gerkey, B., Faust, J., Foote, T., Leibs, J., Wheeler, R., Ng, A.: ROS: an open-source robot operating system, vol. 3 (2009)

5.3.7 Paper G

Ruled Path Planning Framework for Safe and Dynamic Navigation

Alexandre Cardaillac, and Martin Ludvigsen

OCEANS 2021: San Diego – Porto

This paper is not included due to copyright restrictions available in
OCEANS 2021: San Diego – Porto
https://doi.org/10.23919/OCEANS44145.2021.9705699

5.4 Journal Papers

5.4.1 Paper H

Camera-Sonar Combination for Improved Underwater Localization and Mapping

Alexandre Cardaillac, and Martin Ludvigsen

RESEARCH ARTICLE

Camera-Sonar Combination for Improved Underwater Localization and Mapping

ALEXANDRE CARDAILLAC AND **MARTIN LUDVIGSEN**, (Member, IEEE)

Department of Marine Technology, Norwegian University of Science and Technology, 7491 Trondheim, Norway

Corresponding author: Alexandre Cardaillac (alexandre.cardaillac@ntnu.no)

ABSTRACT Taking advantage of the complimentary properties of sonars and cameras can improve underwater visual odometry and point cloud generation. However, this task remains difficult as the image generation concepts are different, giving challenges to direct acoustic and optic feature matching. Solving this problem can improve applications such as underwater navigation and mapping. A camera-sonar combination is proposed for real time scale estimation using underwater monocular image features combined with a multibeam forward looking sonar. The detected features from a monocular SLAM framework are matched with the acoustic features based on the relative distances in instrument reference frame calculated using the two data streams, and used to estimate a depth ratio. The ratio is optimised over a large sample set to ensure scale stability. The sensor combination enables real time scale estimation of the trajectory and the mapped environment, which is a requirement for autonomous systems. The proposed approach is experimentally demonstrated for two underwater environments and scenarios, a subsea module mapping and a ship hull inspection. The results demonstrate the efficiency and applicability of the proposed solution. In addition to correctly restoring the scale, it significantly improves the localization and outperforms the tested dead reckoning and visual inertial SLAM methods.

INDEX TERMS Imaging sonar, visual SLAM, underwater perception, 3D reconstruction.

I. INTRODUCTION

Situational awareness of robots is fundamental to enable their autonomy. Simultaneous Localisation And Mapping (SLAM) [1] methods can significantly contribute to the autonomy as they improve the knowledge and understanding of the environment where the robots are operating in real time. However, when the method depends on a monocular camera only, the scale information of the resulting map and calculated vehicle path is lost or ambiguous. The scale information is important for both localization and mapping to enable the autonomy of the robotic platforms.

Underwater scenes can be difficult to observe and understand with an optical camera because of the light conditions in underwater environments. The light refraction makes the object appear blurry or distorted and the produced image becomes dimmer as the depth increases, resulting in loss

The associate editor coordinating the review of this manuscript and approving it for publication was Chengpeng Hao.

of color and contrast perception. The turbidity of the water and the floating particles have an negative impact on the visual range by scattering and absorbing light. Using artificial light, movements of the light source and receiver may cause challenging light and shadow patterns. The advantage of optical imaging is the high resolution and rich information content in the data. Acoustic signals do not depend on seawater turbidity and allow larger observation ranges for underwater structures and objects. Compared to optical data, the resolution of acoustical data is considerably lower. For underwater vehicles, multibeam forward-looking sonars (MB-FLS) is often used to provide accurate observations of the surroundings to enable collision avoidance and safe paths.

In spite of the challenges to optical underwater imaging, features can be detected using computer vision and learning methods through processing to adjust and compensate for the effects present underwater. For MB-FLS imagery, the 3D information of the features is not available, only the relative

FIGURE 1. Overview of the proposed approach to perform camera-sonar combination by matching the sensors respective features.

azimuths and distances are computed, leaving the elevation of the data points ambiguous.

Visual SLAM (VSLAM) is a an active research field where the algorithms and methods are set up to match the available sensors and their configuration to detect and identify features in the environment. Both single and multiple camera systems are used, but the former is most common [2], [3], [4]. The sensors are easy to use and deploy, but for single camera systems in particular, the navigation solution experiences drift. The resulting scale ambiguity represents a particular challenge for SLAM based methods. To improve the results a second camera, a depth camera or an IMU can be added [5], [6], [7]. Monocular SLAM methods have also been developed or augmented specifically for the underwater environment [8], [9]. Sonars can be used for range detection by time of flight measurements. In [10], a FLS is employed with a feature based approach using detection of well-constrained landmarks to accurately estimate 3D points for mapping purposes. A filter-based approach is adopted in [11], the registered scans are processed together with an IMU and a DVL to create online a 2D grid map of the environment. In [12], a method to combine an IMU, a stereo camera and a mechanical scanning profiling sonar is proposed. The camera and sonar are combined over multiple samples. Patches based on the visual features are created and used to determine if they correspond to the features previously observed by the sonar. The complementary properties of optic and acoustic sensors represents a promising solution [13], [14], [15]. In [16], particle filter is used as the data association technique to calibrate the camera and sonar to obtain an accurate transformation matrix. The 3D camera features are then projected onto the sonar scan using the sonar coordinate system. A VSLAM framework is augmented in [17] where the camera is combined with a single beam

echosounder to dynamically restore the scale of the SLAM estimate. To this end, the acoustic cone is modelled and matched to the best corresponding visual feature. The depth ratio is then calculated and applied to all the 3D points and the estimated trajectory.

The efforts made to enable optical and acoustic data combination depend strongly on the setup and application, and very often with low level feature matching mechanisms, i.e., using the main image characteristics such as shape and texture. Direct combination at the feature level for improved navigation and mapping requires more advanced inter-sensor calibration and methods, and is not well studied, and requires specific sensors and calibration routines. Using a sonar in addition to a camera provides a robust, drift free, and consistent solution, together with a basic sensor suite with implementation that are convenient to operate.

This paper aims at combining a monocular camera and a MB-FLS for improved underwater localisation and mapping independent of inertial or gyro data, making it suitable also in areas where inexpensive magnetometer based gyros are not feasible. The optical images are processed in a VSLAM framework to obtain a trajectory and point cloud over time. The sonar measurements are first used to rescale the SLAM estimates by finding correspondences between the sonar features and camera features. A depth ratio is estimated during the initialisation and updated online using the Maximum Likelihood Estimation (MLE). The depth ratio is a single value describing the factor to correct the depth scale of the VSLAM framework. It allows to convert the SLAM's distance unit to meters. The correspondences between the two sensors can be done thanks to the prior knowledge of intrinsic and extrinsic calibration details for the camera. The overlapping acoustic and visual areas can then be estimated, and a sonar feature can be represented as a segment in the camera image. Feature matching is performed based on the relative distances, which also helps removing outliers from the set of visual features such as particles. The matched points enable estimation of the depth ratio used later for the entire set of poses and visual points from the VSLAM framework. The optical-acoustic data combination is performed within the SLAM framework itself, which enables a verification step for the visual features. This provides improved localisation and mapping accuracy together with scale correction. Finally, 3D surface estimation based on the generated re-scaled point cloud is performed, using an adapted Poisson surface reconstruction approach.

To achieve real time underwater SLAM for low cost ROVs used for ship hull inspection is the main objective of this work, and the solutions are applicable to any underwater vehicle equipped with camera and MB-FLS. The camera and sonar sensor models are first presented in Section II including explanations of the inter-sensor correspondence mechanisms. Section III describes the depth ration estimation obtained using the inter-sensor feature matching method. The experiments and results are then presented and discussed in Sections IV and V. Finally, conclusive remarks are
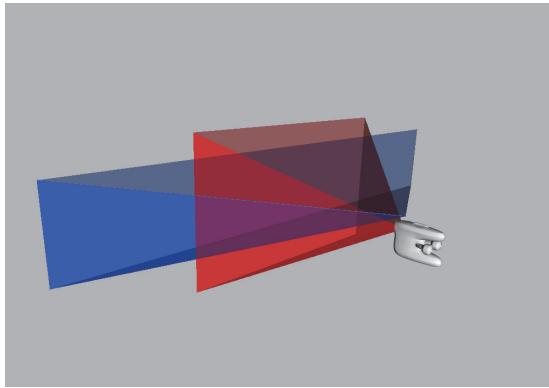
FIGURE 2. The footprints of the perception sensors are represented while the ROV is facing a wall. The camera field of view is in red, and the field of view for the forward looking sonar is shown in blue.

FIGURE 3. The footprint of the forward looking sonar is represented with the corresponding geometry. The minimum and maximum elevation planes are represented, as well as the zero-elevation plane, in which all the planes are merged to after the processing of the measurements. A beam i is also represented, going through all the elevation planes.

formulated in Section VI. An overview of the components and their interactions in the proposed approach is presented in Figure 1.

II. SENSOR MODELS

To understand how correspondences between the features in the sonar data and the optical camera imagery can be created, both sensor models are described. The field of view for the sensors have a large overlap and are horizontally aligned. However, there is a vertical offset because the sonar is mechanically mounted above the camera. The footprints of both sensors are represented in Figure 2. In this paper, we refer to the camera measurements as images, and to sonar measurements as scans, where a scan is defined as the data from all acoustic beams for a single acoustic ping.

A. SONAR MODEL

The sonar emits sound pulses referred to as pings and using the wave properties of acoustics, the multi-element transmitter and receiver array enables directionality for both signal transmission and reception providing acoustic beams. These beams have a vertical and horizontal opening and direction defined by the transducer element array and the signal transceiver. The pings propagate to a target before they are reflected back to the sonar receiver. The target range is estimated based on the signal travel time and the bearing is calculated using the phase difference measured using the transducer array. Most MB-FLS have a one dimensional transducer element array resulting in undefined depression angles for the echos and the sonar can therefore not derive the vertical position of the targets. This means that each point on the sonar imagery is a point on a 3D arc going from the minimum elevation to the maximum allowed by the sensor.

The sonar employed in the experiments was a Blueprint Oculus 750/1200 kHz with horizontal aperture of 130° and 20° vertically. It has 512 beams uniformly distributed and with angular width $\sigma_h = 0.25°$. The ping rate is controlled
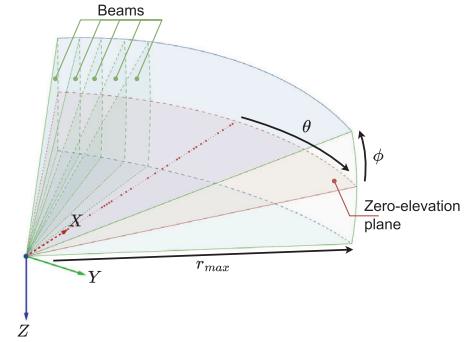
and configured to 10Hz. For the experiment used in this work, the sonar was configured in high frequency mode, corresponding to 1200 kHz, with low gain. A fixed maximum range of 4 meters was set to correlate to the visible range of the camera.

A sonar scan represents a 2D acoustic intensity array representing the features in polar coordinates $[\theta, r]^\top$, where θ is the azimuth angle and r is the range. The scan is formed as a polar image. The 3D geometry of the beams are represented in Figure 3 where the 3D acoustic features are expressed in spherical coordinates $[\theta, \phi, r]^\top$ with the elevation angle ϕ. When the acoustic ping reflections have returned to the sonar, the measurements are merged into a polar grid without elevation information. This grid can be projected onto the zero-elevation plane and placed in the relevant 3D reference frame. To represent the acoustic points in a 3D Cartesian world, given that the elevation angle is known or estimated, the coordinates need to be converted. The spherical-Cartesian coordinates conversion is formulated as

$$P = \begin{bmatrix} P_x \\ P_y \\ P_z \end{bmatrix} = r \begin{bmatrix} \cos\phi \cos\theta \\ \cos\phi \sin\theta \\ \sin\phi \end{bmatrix}, \tag{1}$$

where P is the 3D point in Cartesian coordinates. The inverse conversion is also possible, and given by

$$r = \sqrt{P_x^2 + P_y^2 + P_z^2}, \tag{2}$$

$$\theta = \tan^{-1}\left(\frac{P_y}{P_x}\right), \tag{3}$$

$$\phi = \tan^{-1}\left(\frac{P_z}{\sqrt{P_x^2 + P_y^2}}\right). \tag{4}$$

B. CAMERA MODEL

The camera used in the presented experiments has an imaging frequency of 25Hz and a resolution of 1280×720px. It has

a vertical and horizontal Field Of Views (FOV) underwater of $\sim48°$ and $\sim77°$ respectively. The image was calibrated underwater using a checkerboard and follows the pinhole model which formulates the 2D-3D correspondence as

$$p = \frac{P}{P_z}K, \qquad (5)$$

converting the 3D point P in the world to the 2D point p in pixels in the image, using the intrinsic matrix of the camera K defined as

$$K = \begin{pmatrix} f_x & 0 & c_u \\ 0 & f_y & c_v \\ 0 & 0 & 1 \end{pmatrix}. \qquad (6)$$

The focal length is described by (f_x, f_y), and (c_u, c_v) are the pixel coordinates of the optical centre of the camera.

C. CAMERA-SONAR CORRESPONDENCE

To combine both sensors, correspondences and mapping functions must be setup. They are defined based on both models to formulate the features of the first sensor in the second's sensor frame. For the correspondences, we consider the camera to be the origin of the local reference frame and use the features detected by the SLAM framework. Since the sonar is aligned with the camera with offset only vertically, the transformation matrix is simplified and constitutes an identity matrix for the rotation and a translation vector $[0, 0, t_z]^\top$ describing the vertical offset t_z. This removes the need of computing 6-DoFs sensor transformations. However, this comes with the risk of calibration imprecision which can significantly impact the results. Given that the main objective of this work is to inspect underwater structures, the imprecision is negligible since the operation will be performed with a close range to the objects.

Because the elevation of the sonar features, ϕ, is ambiguous, the exact corresponding points on the camera image cannot be known from the sonar data directly. Instead, the potential locations of an interest point can be represented by a moving vertical segment for each beam, where the beam and the image plane coincide. For an ideal setup where the camera is perfectly calibrated and the mounting offset between the camera and sonar is exactly compensated, each beam corresponds to a segment of the pixel column in the optical image. Because both sensors have different vertical field of views and have a vertical offset, the intersecting beam segment does not include the entire pixel column, and its length varies with the distance to the target. u_i represents the corresponding pixel column for a sonar beam of azimuth θ_i,

$$u_i = f_x \tan(\theta_i) + c_x. \qquad (7)$$

However, since a beam has an angular width σ_h wider than the pixel width, there are multiple corresponding pixel columns for each beam in the optical image. The first and last columns must be calculated with $\theta_i \pm \sigma_h$ where σ_h represents the angle between the beam's central axis and its boundary. To obtain the list of possible vertical pixels for a given beam,
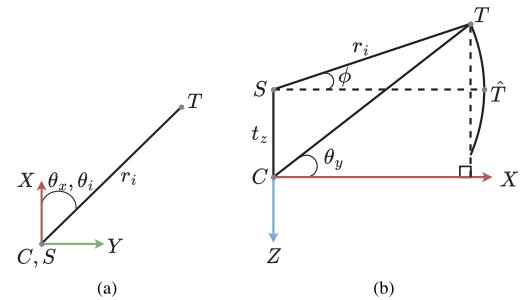
FIGURE 4. The geometry involved to obtain the pixel position on the optical image of a sonar feature T is represented. (a) is a top-down view, in the *Oxy* reference plane, and shows the parameters used to obtain the horizontal position u_i of the pixel with the azimuth θ_i and range r_i of the sonar beam i. (b) presents a side view, in the *Oxz* plane, with a possible sonar beam elevation ϕ. C and S respectively correspond to the camera and sonar positions.

the pinhole formula is not sufficient, the sonar range r_i and the vertical offset t_z must be included in the estimation of the vertical pixel locations v_i,

$$v_i = f_y \tan(\theta_y) + c_y. \qquad (8)$$

The elevation angle for the light ray from the target to the camera is represented by θ_y, and is obtained given a target with location T seen by the sonar at a distance r_i. Its estimated position $\hat{T}$ is initially placed on the sonar's zero-elevation plane and moved along the elevation circle arc constrained by the acoustic beam vertical width, for all $\phi \in [\phi_{min}, \phi_{max}]$. Given that the camera is at the origin of the reference frame, the coordinates of T are enough to obtain the angle θ_y, such that

$$\theta_y = \text{atan2}(T_z, T_x). \qquad (9)$$

Equation (8) can be simplified to avoid multiple operations with tangents,

$$v_i = \begin{cases} f_y \dfrac{T_z}{T_x} + c_y, & \text{if } T_x \neq 0 \\ c_y, & \text{otherwise.} \end{cases} \qquad (10)$$

This problem can be solved in a 2D environment, in the *Oxz* plane, since the camera and the sonar are horizontally aligned. Therefore, the possible positions of T are computed as follows:

$$T = \begin{bmatrix} t_x \\ t_z \end{bmatrix} + r_i \begin{bmatrix} \cos\phi \\ \sin\phi \end{bmatrix}. \qquad (11)$$

A visual representation of the parameters is displayed in Figure 4 with a top-down and side views. The angles are defined relative to a target T and then used together with the Pinhole definitions to obtain a list of pixel candidates on the optical image. The top-down views shows the alignment of the sensors and the horizontal angles from both sensor are the same and remain constant regardless of the vertical angle. The side view shows how are the vertical angles related, given the vertical offset of the sonar.

The mapping from the sonar scan to the camera image is now established with (7) and (10), considering only the overlapping areas. However, a sufficient number of points, which are distributed in the image, are matched to ensure that robust results are obtained in the following sections and can be applied to the not-overlapping areas.

Each visual feature on a sonar line should correspond to a sonar feature. Matching the two features enables the estimation of a depth ratio.

III. DEPTH RATIO ESTIMATION

The feature matching mechanism was developed and executed in three steps followed by the estimation of the ratio.

1) All features are detected in the corresponding image and scan. In the case of the optical camera, 2D features are required as well as triangulated 3D points. To this end, a monocular V-SLAM framework is utilized, ORB-SLAM [18]. For the sonar scans, only 2D features are sampled.

2) All the features are filtered, and only the closest visual and acoustic points are kept.

3) The features are matched based on their respective relative distances and constrained by the possible locations on the image plane.

4) Each detected correspondence is processed to obtain a depth ratio and the MLE is applied over all matches to obtain a unique and consistent depth ratio.

In the following section III-A, the first two steps are covered, the selection and filtering of the good features to match. The last two steps are presented in section III-B, the actual matching of visual and acoustic features and how they are used to obtain scale information.

A. CAMERA-SONAR FEATURE MATCHING

The ORB-SLAM framework for monocular image data provides a trajectory and 3D point cloud over time. It has real-time performance and can work in large environments. It performs feature detection and matching for each image and builds a pose graph over time which enables loop closure and camera relocalisation capabilities. It is a popular lightweight framework that has proven to be very efficient in many applications [19], [20], including in underwater environments [21], [22] in spite of the challenges related to the ORB descriptor applied to image features and characteristics common underwater. Scenarios close to the water surface will often suffer from non-uniform ambient lightning conditions, and in deeper water the motion of the camera and light carrying robot may cause dynamic light and shadow patterns. The Contrast Limited Adaptive Histogram Equalisation (CLAHE) has proven to be an efficient method to compensate for non-uniform lighting environment to highlight the present features before the images are passed through a marine snow filter [23]. The ORB-SLAM's embedded parallax mechanism is made more flexible to enable continuous triangulation of points with
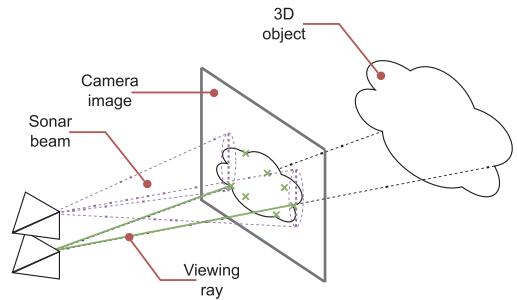
FIGURE 5. A 3D scene is represented with the camera-sonar correspondence and matching mechanisms. The green rays come from the camera, and the purple beams from the sonar.

a slow speed manoeuvring ROV and high camera frame rate. This mechanism also accounts for unwanted features coming from dynamic objects by computing the local median disparity of the tracked features and keeping only those below a threshold. This also results in a fast initialisation process.

Only the polar features of the sonar scans are required for the matching mechanism as they already hold positioning information related to the vehicle's reference frame, i.e., the distance to the object and its horizontal angle relative to the ROV. However, depending on the surrounding structures, the scans might include a significant amount of noise. They are therefore preprocessed to remove the noise and to highlight areas with structural information. A combination of a Gaussian filter and CLAHE is used for that purpose, significantly diminishing the noise while at the same time increasing the intensity values of the structures in sight. Furthermore, this approach allows uniform intensity over the scan sequence.

One feature per beam is selected, the closest with a reflectance above a high reflectance threshold. They correspond to the features with the highest chances of being visually detected as they should also be the closest to the camera.

Three sets of data are now available: the closest sonar points, the 3D point cloud, and the corresponding 2D features on the current image. For each sonar line on the image, based on the sonar feature information and (7) and (8), the closest 3D point that has its 2D correspondence lying on the line is matched. The 3D representation of the data types is displayed in Figure 5 with the sonar beams and camera reprojections.

B. MLE OF THE DEPTH RATIO

Because the ROV is continuously moving, timing is essential. The sonar processing is tightly integrated in the SLAM framework and the time difference between the sonar scans and optical images is monitored to make sure they are synchronised. If the latency is below a threshold, defined as a percentage of the rate difference, the depth ratio is computed for this sonar measurement. This latency check is applied to ensure both sensors are observing the same scene. With a high
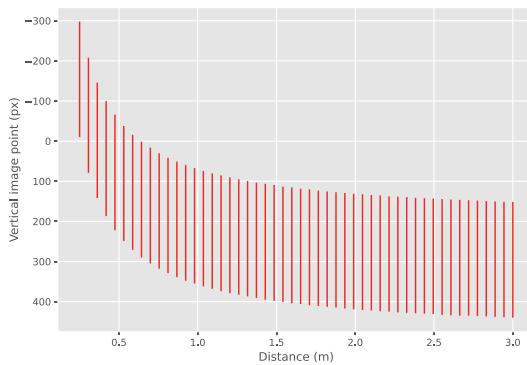
FIGURE 6. The visual table of the camera-sonar correspondences is computed with acoustic distances ranging from 0.25m to 3.0m. Each red line corresponds to a possible projected sonar beam on an image, i.e., its vertical pixel coverage.

latency, it is very likely that the sensors captured the scene from different locations.

Each sonar point, corresponding to a vertical line in the image, is now matched to a visual feature if such exists. For each match, a distance ratio is computed using the visual distance and acoustic distance, such that

$$d_i^c = ||\eta - P_i||, \tag{12}$$

$$_c d_i^s = \frac{r_i}{d_i^c}. \tag{13}$$

where η is the ROV position, P_i the 3D visual point used to obtain the visual distance d_i^c to the camera, r_i the sonar range, and $_c d_i^s$, the distance ratio for the match i. Once performed on each match, a new set of values is obtained. The MLE is employed to extract the final depth ratio, as it robustly find a consistent estimate. More data is accumulated over time, which makes the MLE adapt and estimate a value closer to the optimal one. The set of distance ratios is assumed to be following a Normal distribution $\mathcal{N}(\mu, \sigma^2)$ with mean μ and standard deviation σ. Its probability density function (pdf) is defined as follows,

$$P(x; \mu, \sigma) = \frac{1}{\sigma\sqrt{2\pi}} e^{-\frac{(x-\mu)^2}{2\sigma^2}}, \tag{14}$$

for the observation x. For simplification, the log likelihood is applied by taking the natural logarithm of the expression. This is possible because the natural logarithm is a monotonically increasing function. The equation (14) becomes

$$\ln(P(x; \mu, \sigma)) = \ln\left(\frac{1}{\sigma\sqrt{2\pi}}\right) - \frac{(x-\mu)^2}{2\sigma^2}. \tag{15}$$

Iteratively maximising the above equation, or minimising its negative equivalent, results in optimised estimated values $\hat{\mu}$ and $\hat{\sigma}$ for the current data collected. The depth ratio λ is then assigned to the mean of the estimated normal distribution such that

$$\lambda = \hat{\mu}. \tag{16}$$

The continuous scale correction using the MLE enables a stable correction of the trajectory and point cloud over time, which results in improved localisation performance. Additionally, the normal distribution is used for outlier rejection and correction of the visual 3D points. The points that are more that $2\hat{\sigma}$ away from $\hat{\mu}$, corresponding approximately to the 95% confidence interval, are considered as outliers. The points inside this interval are updated, i.e. displaced further away or closer to match the predicted depth ratio. The elevation and azimuth angles of the updated points remain the same. This verification step is possible because the sonar is accurate and reliable, and has no error growth over time. Therefore, a 3D point with an irregular individual depth ratio can be detected and rejected to prevent the SLAM system from using it for future estimates.

IV. EVALUATION

In this section, the proposed approach is tested and quantitatively compared with three alternative SLAM navigation approaches and the ground truth. The camera-sonar correspondence model is first validated. The list of camera-sonar correspondence possibilities was computed geometrically and plotted in Figure 6. The red bars represent the possible intersections of the sonar beams with the image plane. Given the geometrical configuration, the beams with lower acoustic ranges intersect the higher parts of the image plane because the sonar is placed above the camera. Beams with larger acoustic ranges converge towards the center of the image.

To experimentally validate the setup, objects with known positions were placed in a pool and the ROV, equipped with the camera and sonar, positioned in front of them. The ROV was equipped with a GNSS receiver mounted on a pole, enabling the computation of its position and the distance between the ROV and the objects. The visual results of the first test scene are displayed in Figure 7. The main objects of the scene were detected by the sonar and were easily recognisable because they included high acoustic intensity values. Figure 7d is visually correct since the projected beams on the close objects in the camera image are higher than the rest, because the detected acoustic features corresponding to the objects reported close distances. When observing the stone pillar in both the sonar scan (Figure 7b) and camera image (Figure 7d), it is possible to understand how the sonar beams intersect the image plane at different sections. The edge of the pillar being the closest part of the pillar to the camera and sonar, the intersection segment is naturally higher, closer to the sonar's depth. And the further away the points are from the edge, the further away they are from the camera and sonar, gradually moving the intersection segment towards the center of the image, close to the camera's depth.

The numerical errors were estimated using GNSS as ground truth and are reported in Table 1. Here, the setup was tested in an additional scene, where the vehicle was facing the corner of the pool. While the second column shows a measure of the sonar accuracy, the third reports how well the sonar
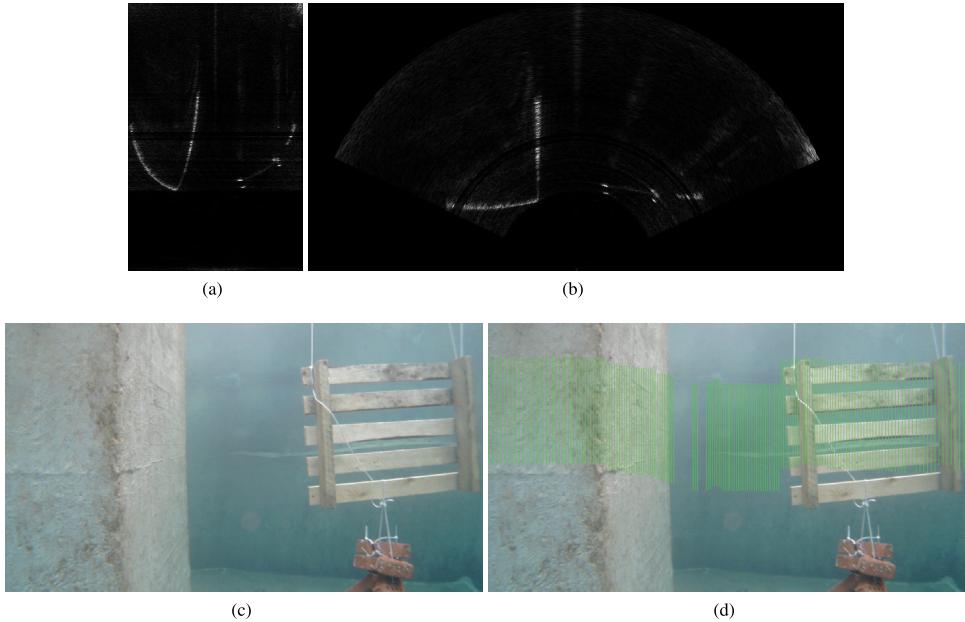
FIGURE 7. (a) is the original sonar scan as a polar image with rows as ranges and columns as bearings. It is converted to cartesian coordinates in (b). The contours of the objects in the scene are recognisable as they present high intensity values. (c) is the original camera image. After applying the sonar features on the image, (d) is obtained. Each green line corresponds to an intersection of a sonar beam with the camera image plane. They highlight the possible locations of the acoustic features on the image plane.

TABLE 1. Camera-sonar correspondence results.

Scene	Distance error	Horizontal angle error
1	$0.04m \pm 0.08m$	$0.22° \pm 0.5°$
2	$0.02m \pm 0.07m$	$0.15° \pm 0.5°$
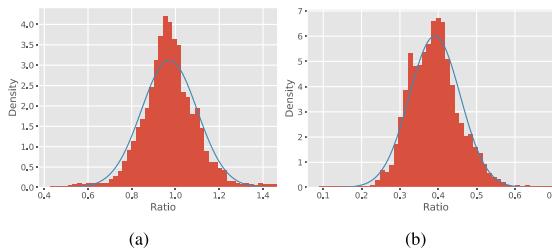
FIGURE 8. Distance ratios were collected and accumulated over a sequence in two different scenes. Histograms (a) and (b) corresponds to the two scenes and Normal probability distributions were fitted and their density functions displayed on top of the histograms.

beams are corresponding to the image features, i.e., the angle difference.

Experimentally, the distance ratios acquired during field trials were found to fit a Normal distribution. The previous two scenes were expanded to include a few minutes of image and scan sequence of the surroundings to compute and create

a set of ratios over time and with a changing scene. The corresponding histograms are displayed in Figure 8 with the density function on top. This validated the choice of the Normal distribution for the MLE. In both scenes, the distance and angle errors are very low, with centimeter level accuracy for the distances, 0.04m and 0.02m, and decimal level accuracy for the angles, 0.22° and 0.15°. For the ship hull mapping and inspection application considered in this work, theses errors are acceptable since the operations are performed close to the structures. For example, given the results from Table 1, at three meters distance, the maximum expected total error of the point correspondence is $\sim 0.15m$, and $\sim 0.05m$ on average.

Ideally, the estimated depth ratio should converge towards 1, meaning the scale does not need to be re-updated. Our approach using the MLE is compared to three alternative approaches, including using simply the median or the mean, and using a single central beam. In this scenario, for each method, the depth ratio is estimated and applied every time there is a new keyframe created in the SLAM framework. The convergence rate of each method can be observed in Figure 9. While all methods converge rapidly, only the proposed one is continuously stable once it has converged. This is especially important for real-time operations as scale errors can quickly propagate to the depending systems. Peaks can appear when there is a sudden change of geometry in the scene, or when the ROV is turning, but they are immediately corrected. The method using the median showed high variations because it
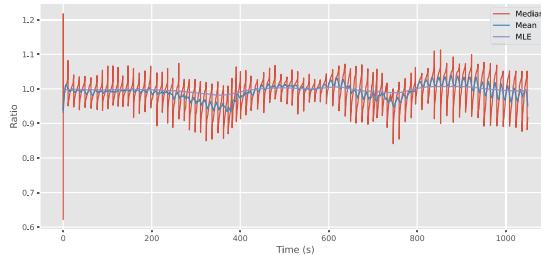
(a)
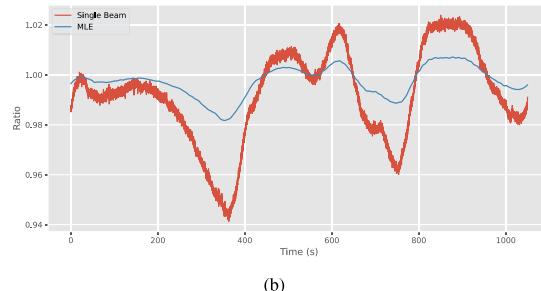
(b)

FIGURE 9. The depth ratio evolution over time is displayed. The proposed method using the MLE is compared to the mean and median in (a) and to a single central beam estimation in (b).

(a)

(b)

(c)

FIGURE 10. The 2D trajectories of all the methods used for comparisons are plotted in (a) and only the scaled ones in (b). (c) displays the position error over time of all the trajectories including the manually rescaled monocular SLAM trajectory.

TABLE 2. Performance metrics for trajectory evaluation.

Method	ATE	RPE	Init. time	Complete- ness
Mono SLAM	0.091m	0.088m	1.2s	92%
VI SLAM	0.229m	0.203m	10.9s	84%
Dead Reckoning	0.201m	0.168m	0.0s	100%
VS SLAM	0.053m	0.049m	1.2s	98%

was heavily influenced by the new values added to the set and therefore by the shifts in sonar range. In comparison, using the mean was more stable, but still contained oscillatory results. When a single beam was used, the results improved. However, this method was more prone to noise, which can then destabilize the future SLAM estimates. Using the proposed method based on the MLE brings scale stability and consistency over longer periods of time, and once it has converged, it remains stable with low variance around the convergence point.

To show how the proposed method performs and improves the VSLAM framework, the trajectory estimate was compared to the default monocular SLAM from ORB-SLAM, visual-inertial SLAM, and dead reckoning using an IMU and a DVL. Additionally, a trajectory interpolating GNSS fixes and visual markers was computed and used as the ground truth.

The estimated trajectory of each method is displayed in Figure 10. They were all manually aligned. This visual comparison enables a first assessment of the method's performance and of the rescaled trajectory from the proposed method. The trajectory of the monocular SLAM (Mono SLAM), although correct, is off scale and can not be used for robotic applications. However, it was manually rescaled for the purpose of comparison. The rescaled version of the trajectory using the sonar (VS SLAM) appears close to the ground-truth compared to the other solutions. The visual-inertial SLAM (VI SLAM) was also able correctly

rescale the trajectory, however, as the scale factor is estimated during the initialisation, if it is incorrectly estimated, it will lead to acceleration bias errors which can quickly propagate to the position estimates. Also, the noise of the low cost IMU influenced the plotted trajectory negatively. The dead reckoning solution performed well but showed apparent drift over time that made the trajectory end at a different location. The numerical results are highlighted in Table 2, with for each method, the Absolute Trajectory Error (ATE) computed with the Root Mean Square Error (RMSE), and the Relative Position Error (RPE). They were calculated over the whole trajectory. The initialisation time is also included, corresponding to how much time the framework needed to converge to an initial position estimate. Finally, the completeness represents how much of the dataset is successfully covered by the method, i.e., how many estimates were provided over time compared to the data available. Typically, long initialisation processes and visual tracking losses will result in significant loss of coverage.

The dead reckoning method was quickly initialising and always provided an estimate. However, it drifted quickly. The VI-SLAM showed the largest drift and lowest accuracy of the candidates, but thanks to the ORB-SLAM capabilities, the

(a)

(b)

(c)

(d)
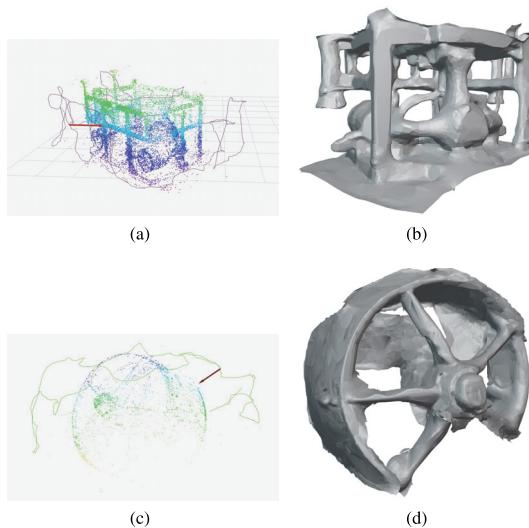
FIGURE 11. (a) and (c) are the rescaled point clouds and trajectories from the proposed pipeline, and (b) and (c), their corresponding 3D models from the online Poisson surface estimation.

trajectory still ended close to the ground-truth. In comparison, the proposed method had very low ATE and RPE, and also ended close to the ground-truth. However, this method lost accuracy during turns.

V. APPLICATIONS

The proposed method can be used for image enhancement using depth prior, robotic navigation, or 3D reconstruction. The latter will be explored in this section in two independent inspection scenarios. The first one consists of an inspection of a subsea module, and the second, of an inspection of a ship propeller. Underwater inspections are important to assess the structure integrity. In the case of remote inspections, the operation is typically overviewed by an inspector monitoring the inspection through a transmitted visual stream. Establishing scale to the scene allows additional and automatically processed data enabling better inspection condition and assessment of the structure.

The 3D reconstruction is based on the online generated point cloud from the proposed approach, combining the camera and the sonar within the ORB-SLAM framework, ensuring the estimation of a correctly scaled model. It is performed in real-time using the inactive rescaled visual point from the modified SLAM framework. The inactive points represent the SLAM 3D points not being tracked or modified. The Poisson surface estimation was applied to obtain a set of 3D faces displayed to the operator for monitoring purposes. This method is particularly efficient for the mapping application since it can work with noisy data and misregistered points while estimating the surface fast. The 3D surface was estimated in real time to facilitate object and place recognition for the inspector enabling real time updates

of the mission plan based on the findings. The results for the two scenarios are displayed in Figure 11, with both the prior point cloud and the resulting estimated surface. The geometry of the 3D objects is not exact, but provides a representative presentation with the correct scale. In the case of inspection missions, the generated model can be exported along with annotations from the inspector, making the inspection process more efficient, repeatable and accurate.

VI. CONCLUSION

A new approach to monocular SLAM estimates rescaling is presented, using a MB-FLS for scale estimation. The proposed camera-sonar combination includes estimation of individual sonar beam coverage in the optical image, enabling visual-acoustic feature matching. This allows depth ratio estimation after the application of the maximum likelihood estimation, providing continuous rescaling, and stability. The proposed pipeline was experimentally tested and the results show improvements in stability and robustness compared to known methods.

However, it was observed during the experiments that the position error tends to increase when the vehicle turns. This is likely due to the camera-sonar calibration imprecision. A calibration step in the processing pipeline would improve these errors and will be studied in the future. Also, the method would benefit from a tighter integration of the sonar in the SLAM framework, including the addition of parameters such as the speed of sound and the reprojection errors of the acoustic features. This would also enable the sonar to keep estimating the pose of the vehicle during periods of camera outages, for example when images become too blurry to keep tracking the visual features. For monitoring applications, especially for inspection missions, semantic SLAM can significantly improve scene understanding and therefore, inspection results. This will be studied in the case of ship hull inspection, using the previously developed LIACi dataset [24].

REFERENCES

[1] H. Durrant-Whyte and T. Bailey, "Simultaneous localization and mapping: Part I," *IEEE Robot. Autom. Mag.*, vol. 13, no. 2, pp. 99–110, Jun. 2006.

[2] R. Mur-Artal, J. M. M. Montiel, and J. D. Tardós, "ORB-SLAM: A versatile and accurate monocular SLAM system," *IEEE Trans. Robot.*, vol. 31, no. 5, pp. 1147–1163, Oct. 2015.

[3] J. Engel, T. Schöps, and D. Cremers, "LSD-SLAM: Large-scale direct monocular SLAM," in *Computer Vision—ECCV*, D. Fleet, T. Pajdla, B. Schiele, and T. Tuytelaars, Eds. Cham, Switzerland: Springer, 2014, pp. 834–849.

[4] G. Klein and D. Murray, "Parallel tracking and mapping for small AR workspaces," in *Proc. 6th IEEE ACM Int. Symp. Mixed Augmented Reality*, Nov. 2007, pp. 225–234.

[5] T. Qin, P. Li, and S. Shen, "VINS-Mono: A robust and versatile monocular visual-inertial state estimator," *IEEE Trans. Robot.*, vol. 34, no. 4, pp. 1004–1020, Aug. 2018.

[6] R. Mur-Artal and J. D. Tardós, "ORB-SLAM2: An open-source SLAM system for monocular, stereo, and RGB-D cameras," *IEEE Trans. Robot.*, vol. 33, no. 5, pp. 1255–1262, Oct. 2017.

[7] J. Sturm, N. Engelhard, F. Endres, W. Burgard, and D. Cremers, "A benchmark for the evaluation of RGB-D SLAM systems," in *Proc. IEEE/RSJ Int. Conf. Intell. Robots Syst.*, Oct. 2012, pp. 573–580.

[8] M. Ferrera, J. Moras, P. Trouvé-Peloux, and V. Creuze, "Real-time monocular visual odometry for turbid and dynamic underwater environments," *Sensors*, vol. 19, no. 3, p. 687, Feb. 2019.

[9] S. Xu, T. Luczynski, J. S. Willners, Z. Hong, K. Zhang, Y. R. Petillot, and S. Wang, "Underwater visual acoustic SLAM with extrinsic calibration," in *Proc. IEEE/RSJ Int. Conf. Intell. Robots Syst. (IROS)*, Sep. 2021, pp. 7647–7652.

[10] E. Westman, A. Hinduja, and M. Kaess, "Feature-based SLAM for imaging sonar with under-constrained landmarks," in *Proc. IEEE Int. Conf. Robot. Autom. (ICRA)*, May 2018, pp. 3629–3636.

[11] C. Cheng, C. Wang, D. Yang, W. Liu, and F. Zhang, "Underwater localization and mapping based on multi-beam forward looking sonar," *Frontiers Neurorobotics*, vol. 15, Jan. 2022, Art. no. 801956.

[12] S. Rahman, A. Q. Li, and I. Rekleitis, "Sonar visual inertial SLAM of underwater structures," in *Proc. IEEE Int. Conf. Robot. Autom. (ICRA)*, May 2018, pp. 5190–5196.

[13] S. Negahdaripour, H. Sekkati, and H. Pirsiavash, "Opti-acoustic stereo imaging: On system calibration and 3-D target reconstruction," *IEEE Trans. Image Process.*, vol. 18, no. 6, pp. 1203–1214, Jun. 2009.

[14] S. Bejarano, P. J. Mumby, J. D. Hedley, and I. Sotheran, "Combining optical and acoustic data to enhance the detection of Caribbean forereef habitats," *Remote Sens. Environ.*, vol. 114, no. 11, pp. 2768–2778, Nov. 2010.

[15] A. Spears, A. M. Howard, M. West, and T. Collins, "Acoustic sonar and video sensor fusion for landmark detection in an under-ice environment," in *Proc. Oceans St. John's*, Sep. 2014, pp. 1–8.

[16] Y. Raaj, A. John, and T. Jin, "3D object localization using forward looking sonar (FLS) and optical camera via particle filter based calibration and fusion," in *Proc. OCEANS MTS/IEEE Monterey*, Sep. 2016, pp. 1–10.

[17] M. Roznere and A. Q. Li, "Underwater monocular image depth estimation using single-beam echosounder," in *Proc. IEEE/RSJ Int. Conf. Intell. Robots Syst. (IROS)*, Oct. 2020, pp. 1785–1790.

[18] C. Campos, R. Elvira, J. J. G. Rodríguez, J. M. M. Montiel, and J. D. Tardós, "ORB-SLAM3: An accurate open-source library for visual, visual–inertial, and multimap SLAM," *IEEE Trans. Robot.*, vol. 37, no. 6, pp. 1874–1890, Dec. 2021.

[19] A. Sujiwo, N. University, T. Ando, E. Takeuchi, Y. Ninomiya, and M. Edahiro, "Monocular vision-based localization using ORB-SLAM with LiDAR-aided mapping in real-world robot challenge," *J. Robot. Mechatronics*, vol. 28, no. 4, pp. 479–490, Aug. 2016.

[20] S. J. Haddadi and E. B. Castelan, "Visual-inertial fusion for indoor autonomous navigation of a quadrotor using ORB-SLAM," in *Proc. Latin Amer. Robotic Symp., Brazilian Symp. Robot. (SBR) Workshop Robot. Educ. (WRE)*, Brazil, Nov. 2018, pp. 106–111.

[21] F. Hidalgo, C. Kahlefendt, and T. Bräunl, "Monocular ORB-SLAM application in underwater scenarios," in *Proc. OCEANS-MTS/IEEE Kobe Techno-Oceans (OTO)*, May 2018, pp. 1–4.

[22] Y. Zhang, L. Zhou, H. Li, J. Zhu, and W. Du, "Marine application evaluation of monocular SLAM for underwater robots," *Sensors*, vol. 22, no. 13, p. 4657, Jun. 2022.

[23] A. Cardaillac and M. Ludvigsen, "Marine snow detection for real time feature detection," in *Proc. IEEE/OES Auto. Underwater Vehicles Symp. (AUV)*, Sep. 2022, pp. 1–6.

[24] M. Waszak, A. Cardaillac, B. Elvesæter, F. Rødølen, and M. Ludvigsen, "Semantic segmentation in underwater ship inspections: Benchmark and data set," *IEEE J. Ocean. Eng.*, vol. 48, no. 2, pp. 462–473, Apr. 2023.

ALEXANDRE CARDAILLAC received the Bachelor of Information Technology degree from the School of Digital Innovation, Nantes, France, in 2019, and the M.Sc. degree in artificial intelligence with speech and multimodal interaction from Heriot-Watt University, Edinburgh, U.K., in 2020. He is currently pursuing the Ph.D. degree in engineering with the Department of Marine Technology, Norwegian University of Science and Technology, Trondheim, Norway.

MARTIN LUDVIGSEN (Member, IEEE) was born in 1977. He received the Ph.D. degree in underwater technology from Norges Teknisk-Naturviten Skapelige Universitet (NTNU), Trondheim, Norway, in 2010.

Since 2014, he has been a Professor with the Department of Marine Technology, NTNU, where he is currently a Co-Founder and the Manager of the Applied Underwater Laboratory (AUR-Laboratory). The AUR-Laboratory (https://www.ntnu.edu/web/aur-lab/aur-lab) facilitates research within both engineering disciplines and marine science by providing ROV, AUV, and USV operations. He has long experience at-sea both in arctic waters and in benthic environments associated with Norwegian Midocean Ridge. He has been involved in research projects both in the deep sea, the upper water column, and arctic deploying robotic underwater vehicles. His research interests include the field of underwater vehicles, including perception and interpretation of cameras and sonar data together with autonomy. Adaptive mission planning for one or more vehicles for ocean column mapping has also been a focus point for his research group.

• • •

5.4.2 Paper I

ROV-Based Autonomous Maneuvering for Ship Hull Inspection with Coverage Monitoring

Alexandre Cardaillac, Roger Skjetne and Martin Ludvigsen

This article is awaiting publication and is not included in NTNU Open

5.4.3 Paper J

Semantic Segmentation in Underwater Ship Inspections: Benchmark and Data Set

Maryna Waszak, Alexandre Cardaillac, Brian Elvesæter, Frode Rødølen and Martin Ludvigsen

IEEE Journal of Oceanic Engineering

Semantic Segmentation in Underwater Ship Inspections: Benchmark and Data Set

Maryna Waszak ⓘ, *Member, IEEE*, Alexandre Cardaillac ⓘ, Brian Elvesæter ⓘ, Frode Rødølen ⓘ,
and Martin Ludvigsen ⓘ, *Member, IEEE*

Abstract—In this article, we present the first large-scale data set for underwater ship lifecycle inspection, analysis and condition information (LIACI). It contains 1893 images with pixel annotations for ten object categories: defects, corrosion, paint peel, marine growth, sea chest gratings, overboard valves, propeller, anodes, bilge keel and ship hull. The images have been collected during underwater ship inspections and annotated by human domain experts. We also present a benchmark evaluation of state-of-the-art semantic segmentation approaches based on standard performance metrics. Consequently, we propose to use U-Net with a MobileNetV2 backbone for the segmentation task due to its balanced tradeoff between performance and computational efficiency, which is essential if used for real-time evaluation. Also, we demonstrate its benefits for in-water inspections by providing quantitative evaluations of the inspection findings. With a variety of use cases, the proposed segmentation pipeline and the LIACI data set create new promising opportunities for future research in underwater ship inspections.

Index Terms—Data set, semantic segmentation, supervised machine learning, underwater inspection.

I. Introduction

ANNOTATED data sets of underwater ship hull inspections for semantic segmentation are scarce. In this section, we present our motivation for creating such a publicly available data set by describing how in-water ship inspections are conducted and how semantic segmentation would make the process more efficient.

The rest of this article is organized as follows. Section II describes the collection of data and the creation of the data set used for the training of the selected semantic segmentation models. Section III presents and discusses the experimental results of the

Maryna Waszak and Brian Elvesæter are with SINTEF AS, 0373 Oslo, Norway (e-mail: maryna.waszak@sintef.no; brian.elvesater@sintef.no).
Alexandre Cardaillac and Martin Ludvigsen are with the Department of Marine Technology, Norwegian University of Science and Technology, 7034 Trondheim, Norway (e-mail: alexandre.cardaillac@ntnu.no; martin.ludvigsen@ntnu.no).
Frode Rødølen is with VUVI AS, 5035 Bergen, Norway (e-mail: frode@vuvi.no).

benchmark evaluation. Section IV points out future directions in improving the data set and how a semantic segmentation model could aid other research topics in underwater computer vision. Finally, Section V concludes this article.

A. Underwater Ship Inspections

Visual inspections are rigorously applied in different domains of our lives. With increasing exploitation of marine resources, significant attention is being drawn to the importance of underwater ship inspections. As of today, the monitoring and inspection of marine vessels is performed based on recurrent visual observations and assessments of structural condition either in dry-dock or underwater. The main purpose of these inspections is to assist with the examination of the external coating, as well as detection of corrosion or marine growth. Inspections in dry-dock are significantly costlier than in-water inspections in addition to longer downtime of the ship. Therefore, ship hull inspections performed underwater are increasing in popularity. With the technological advances in the field of autonomous underwater vehicles, the need for automated data processing becomes inevitable as the manual reviewing and processing of collected videos, images, and other nondestructive inspection data (e.g., ultrasonic thickness measurements) becomes unfeasible [1].

B. Semantic Segmentation

The advances in computer vision provide ways for increasing reliability and effectiveness for acquiring, managing, integrating, and interpreting the acquired inspection data at a minimum cost while reducing the need for tedious and often unreliable data analysis by a human expert. Specifically, automated processing of image and video data is a great source of quantitative insight that can complement the largely qualitative information obtained from conventional visual inspections. In contrast to land images, however, the underwater environment poses several challenges for automated image processing. The images may be deteriorated by different artifacts, such as water turbidity, floating particles, severe absorption, reflections, scattering of light, nonuniform illumination, various noises, low contrast and monotonous colors. See Fig. 1 for some examples of mentioned artifacts.

This work focuses on semantic image segmentation in the domain of underwater ship inspections and how it can aid the inspection procedure by providing additional insight from the acquired underwater video data. Semantic segmentation refers to pixelwise classification, a class label is assigned to each pixel
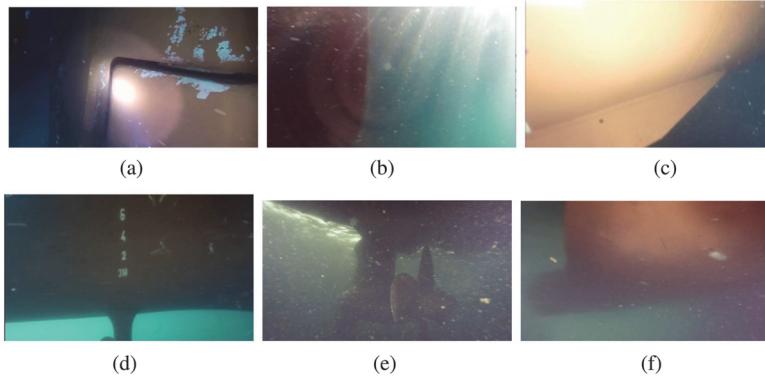
Fig. 1. Common artifacts in underwater imagery. (a) Light beam. (b) Light scattering. (c) Reflections. (d) Scratches on lens. (e) Floating particles. (f) Water turbidity.
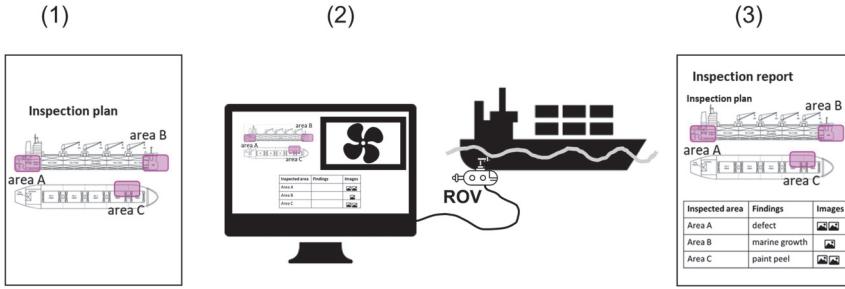
Fig. 2. Current inspection workflow is performed in three separate steps: 1) planning, 2) data acquisition, and 3) report creation.

of the image. It is a well-studied problem as it is a key for scene understanding. It decomposes the scene into objects or categories, which are significant semantic regions. Recent methods involving a deep learning approach have achieved outstanding results [2], [3], [4]. The current state-of-the-art segmentation networks have been mostly proposed for and applied to medical image analysis, driver-less cars or other surface applications. It remains to be shown that those successful networks can be successfully applied to underwater segmentation tasks. In this work, we aim at closing this gap through a benchmark evaluation on our data set.

C. Available Data Sets

Currently, manually labeled data sets such as ImageNet [5], ADE20K [6], PASCAL [7], and COCO [8] play a significant role in improving machine vision tasks and driving research in new directions. Data sets with underwater imagery such as SUIM [9] or Seagrass [10] exist that aim at the semantic segmentation task or the classification of fish [11] or marine growth [12] species. Although works related to the detection and segmentation of relevant classes and objects in the domain of visual surface inspections as marine growth, corrosion, and cracks exist, the underlying data sets remain undisclosed or are inaccessible [13], [14], [15], [16], [17], [18], [19].

We wanted to create a publicly available data set that aims at the task of semantic segmentation of underwater ship inspection images. This data set is meant to be used as a starting point for underwater scene understanding and improved machine vision in the domain of in-water ship inspections.

D. Lifecycle Inspection, Analysis and Condition Information (LIACI) Use Case

Here, we worked with a combination of commercial hardware and software for conducting underwater ship inspections. Several experts were involved and the inspections were performed in different steps as depicted in Fig. 2: 1) planning, 2) data acquisition, and 3) report creation. The software and hardware involved is named the LIACI system. The introduced use case is from two Norwegian companies: VUVI AS,[1] which is a commercial provider of underwater ship hull inspections, and Posciom AS,[2] which is the provider of the video tagging and management platform Seekuence.

The current data acquisition setup consists of the underwater remotely operated vehicle (ROV) and two separate video streams. One stream is used for the navigation of the ROV and

[1][Online]. Available: vuvi.no
[2][Online]. Available: www.posicom.no
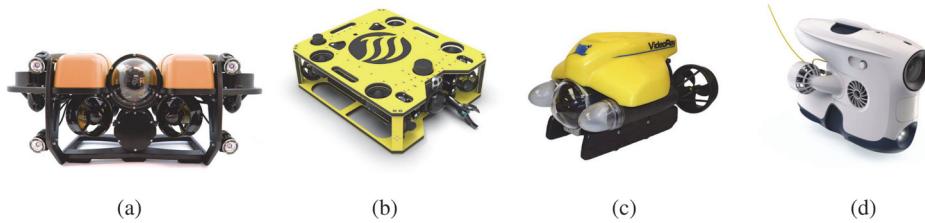
Fig. 3.   ROVs that were used for data collection during underwater ship inspections. (a) JM Robotics BlueROV2. (b) JM Robotics JM HD1. (c) VideoRay Pro 4. (d) Blueye Pioneer.

TABLE I
NUMBER OF IMAGES COLLECTED BY DIFFERENT ROV TYPES

ROV name	Image resolution	Image count	Number of different ships
VideoRay Pro 4	640 × 480	284	5
JM Robotics BlueROV2	1920 × 1080	725	4
JM Robotics JM HD1	1280 × 720	837	7
Blueye Pioneer	1920 × 1080	47	1

the second one for video frame annotation, where interesting frames in the video are marked to be further evaluated. The ROVs are supplied by different commercial vendors (see Section II-A on data collection for further details). After the video data are acquired, the annotated video snippets are screened in a postprocessing step and snap shots are extracted for a final inspection report. The acquired and annotated data are archived for later reference.

The current workflow is tedious and time consuming and does not incorporate any automated data processing. We propose to use semantic segmentation to identify and quantify different metrics relevant for the ship inspection procedure. By automatic annotation and quantitative analysis of video data, the inspection report can be created without human interaction. Hence, the effort in the third step in the current workflow can be significantly reduced.

II. LIACI DATA SET

This section describes the collection of inspection video data and the image extraction process. It illustrates the difficulties specific to labeling underwater inspection data and explains the classes that were chosen as labels for the annotation task. Further, it shows how the images were annotated, and the resulting statistical properties of the images. We also included an evaluation on the similarity of the images in the data set.

A. Data Collection

Videos from 16 underwater ship inspections were collected by the commercial inspection provider VUVI AS using two different ROVs from JM Robotics AS[3] and one ROV from

VideoRay[4] with an in-built filter from LYYN.[5] The names of the vessels remain secret due to nondisclosure agreements with the ship owners. Additionally, at the research vessel Gunnerus,[6] one video of the hull was acquired with the Pioneer drone from Blueye.[7] Fig. 3 shows the drones that were used for data collection, and in Table I, the individual image count that was chosen for the data set. The videos were recorded at different locations in the Norwegian Sea off the Norwegian coast. From these videos, a representative collection of images was extracted by the ROV operator during the video recording and in the postprocessing step preparing the inspection report.

Imaging tasks in an underwater environment are challenging. Even though some of characteristics are generalizable, many are dependent on the location and its situation. The underwater visibility is mainly affected by the penetration of the light and the water turbidity. Because of this, it is important that the proposed data set presents image diversity in terms of underwater scene conditions. This makes it possible to reduce the classwise water condition specific overfitting when training a model. Even though the data were acquired only at the Norwegian coast, we can observe a range of visibility conditions. The variety of ships presents different feature combinations, which is an important aspect to further improve the robustness.

The images were extracted by the ship inspector during video recording and in the postprocessing step to reflect the status of the inspected areas. These images were used to train an image classifier to find images in similar classes to ramp up the image count. In the first sweep, the inspector usually extracted approximately 50–100 images from the video. We trained a vision transformer multilabel classifier with Microsoft Custom

---

[3][Online]. Available: www.jmrobotics.no

[4][Online]. Available: videoray.com
[5][Online]. Available: www.lyyn.com
[6][Online]. Available: www.ntnu.edu/gunnerus
[7][Online]. Available: www.blueye.no

TABLE II
OVERVIEW OF ANNOTATED CLASSES WITH ASSOCIATED DESCRIPTION AND MASK COLOR

Group	Class	Description	Mask color
Ship parts	Ship hull	The main ship structure.	Blue
	Propeller	All revolving structures on the ship.	Purple
	Bilge keel	A stabilizing structure on the ship hull to reduce rolling motion.	Orange
	Anode	Sacrificial anodes that provide galvanic cathodic protection of submerged metal structures from corrosion.	Cyan
	Sea chest grating	Sea chests are intake reservoirs for water piping systems on a ship. They are protected by removable gratings.	White
	Overboard valve	Usually located on the sides of the ship. They are round openings on the ship hull that serve as in and outlets.	Turquoise
Inspection criteria	Corrosion	Oxidized metal parts of the ship.	Yellow
	Paint peel	Any damage to the condition of the anti-fouling coverage on the ship hull. That is coating, paint, or other surface treatment that is used on a ship to control or prevent attachment of unwanted marine organisms.	Red
	Marine growth	The accumulation of aquatic organisms such as microorganisms, algae, and animals on surfaces and structures immersed in or exposed to the aquatic environment. Bio-fouling types can include soft bio-fouling and hard calcareous bio-fouling.	Green
	Defect	All other defects that are neither corrosion, marine growth, nor paint peel.	Pink

Vision[8] [20] and indexed the videos to find images for the classes of interest. This way we could ramp up the image count to a total of 1893 images and also mimic the inspectors' choice for the data from the research vessel Gunnerus where no inspector was involved. Fig. 11 summarizes the steps visually.

B. Data Labeling

A total of ten different labels divided into two categories were proposed. They were selected to provide relevant and detailed information that could be used for an automated or aided inspection. The first category corresponds to the physical parts of a ship that can be found underwater, while the second category is about what can be found on the surface of the ship that is not originally part of it. The latter category is called inspection criteria because it corresponds to what the inspector is looking for when performing an inspection. These are often subject to evolve over time, e.g., disappear after maintenance, change over time, and reappear again. We have often noncanonical viewpoints and only some iconic images, thus we focus mostly on categories with clear boundaries. However, due to natural water turbidity that increases with the distance from the camera, the ship hull and other relatively big ship parts do not have clear boundaries.

An overview of the classes is given in Table II with a description for each class. The colors are used to differentiate the labels in the processed scenes. In the majority of cases, these two categories overlap each other, providing information about the location of the inspection criteria.

The selected classes cover a large part of the image while minimizing the "blank" part of the image, i.e., without annotation. These parts frequently correspond to the underwater background.

We created guidelines for labeling to have consensus among the annotators to mitigate some of the annotation difficulties. Specifically, it is not a trivial task separating marine growth, paint peel, and corrosion, as can be seen in Fig. 4. Here, it is extremely difficult to separate the different classes as they usually appear overlapping each other and rarely on their own.

The annotation task was performed by two annotators using the Microsoft Azure Machine Learning Studio[9] web-based platform. The annotation method consisted of layered polygons that when combined should cover the entire underwater scene without the background. After completion of the data set, all the images and associated annotations were reviewed again and corrected where necessary by the same annotators to guarantee

---

[8][Online]. Available: https://www.customvision.ai/

[9][Online]. Available: https://ml.azure.com
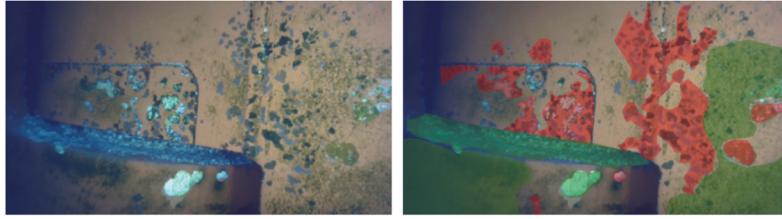
Fig. 4. Example of an image where separating the labels for paint peel and marine growth is challenging due to overlaps. The raw image is shown on the left and the same image with overlapped segmentation results on the right.
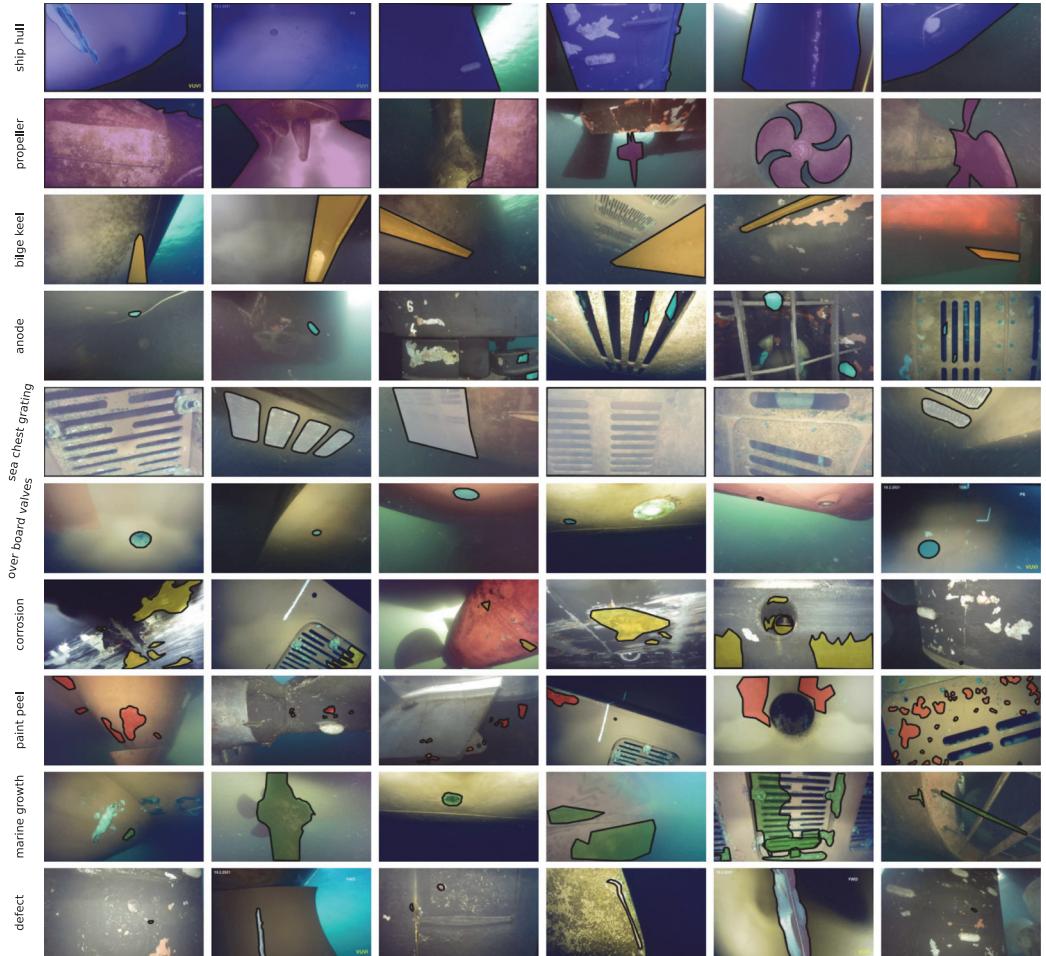
Fig. 5. Samples of annotated images in the LIACI data set for each class.

high fidelity annotations. The samples of annotated images for each class are depicted in Fig. 5, with one class per row.

A representative sample of the data set consisting of 100 images was sent to a professional ship inspector to assess the quality and precision of the annotations. The inspector had access to the labeling tools, allowing him to update the masks based on his knowledge. We used his review as ground truth to compute the precision, recall, and F1 score for each class and to determine if there was any action to be taken. The results are given in Table III for each class and metrics. The "ship parts" category is very accurate, this was expected since all the subparts are very easily recognizable and can hardly be confused. For

Metric	Ship hull	Propeller	Bilge keel	Anode	Sea chest grating	Overboard valve	Mean
Precision	98.41	99.51	98.85	99.00	98.46	99.74	99.00
Recall	98.67	99.98	99.93	99.00	99.98	99.00	99.42
F1 Score	98.54	99.74	99.39	99.00	99.21	99.37	99.21

Metric	Defect	Corrosion	Paint peel	Marine growth	Mean		Combined
Precision	99.00	89.99	92.68	80.94	90.65		95.66
Recall	99.00	99.06	86.04	92.00	94.02		97.26
F1 Score	99.00	94.31	89.23	86.11	92.30		96.45
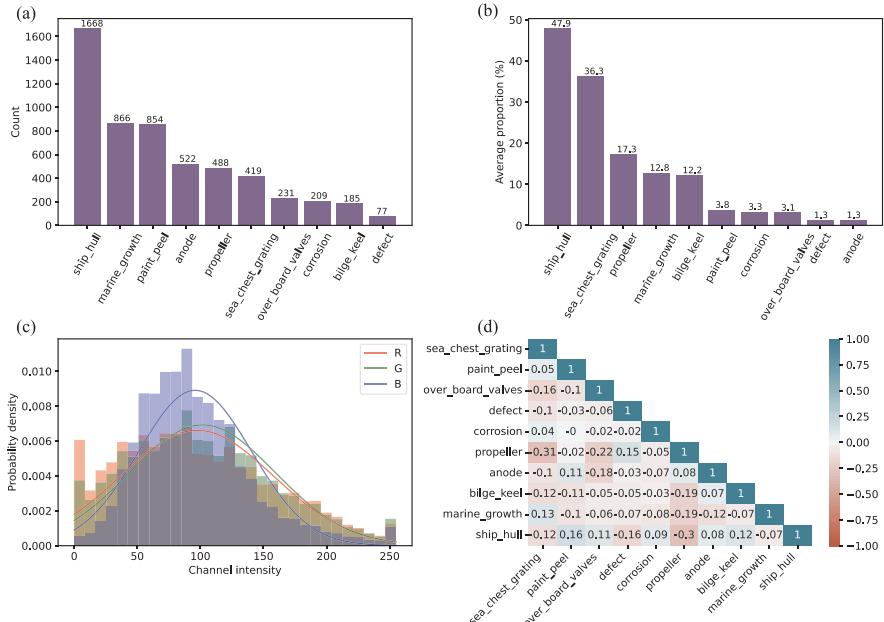
Fig. 6. Overview over the image and label statistics. (a) Number of annotated images per class. (b) Average proportion of annotated pixels in images for each class. (c) Distribution of the pixel intensities in each channel. (d) Pairwise correlation of the labels occurrences in the data set based on the Pearson method.

the "inspection criteria," however, the distinction between the subparts is not as easy, especially with marine growth and paint peel, and sometimes corrosion. Based on the inspector's review, some were misclassified, but overall, the three metrics remain acceptable and indicate the quality of the data set labels.

C. Data Set Presentation

The proposed data set contains 1893 RGB images alongside their pixelwise annotations for semantic segmentation. Images with different aspect ratio and resolution are included, e.g., 1920×1080, 1280×720 and 640×480. Detailed statistics of the images and labels are shown in Fig. 6. Since pixel intensity value is the primary information stored within pixels, it is the most popular and important feature used in computer vision.

The intensity value for each pixel consists of three values for the color images. In the presented data set, we observed that the blue channel is over-represented compared to the red and green colors that is easily explained by the underwater domain where the images were collected.

The pairwise correlations of the labels are calculated using Pearson's correlation coefficient r. It quantifies the linear relationship between two distributions based on the covariance and standard deviation

$$r_{X,Y} = \frac{\text{cov}(X,Y)}{\sigma_X \sigma_Y} \quad (1)$$

with the two distributions X and Y. r ranges from -1, the perfect negative correlation, to $+1$, the perfect positive correlation. Therefore, since the correlation matrix presented shows a good
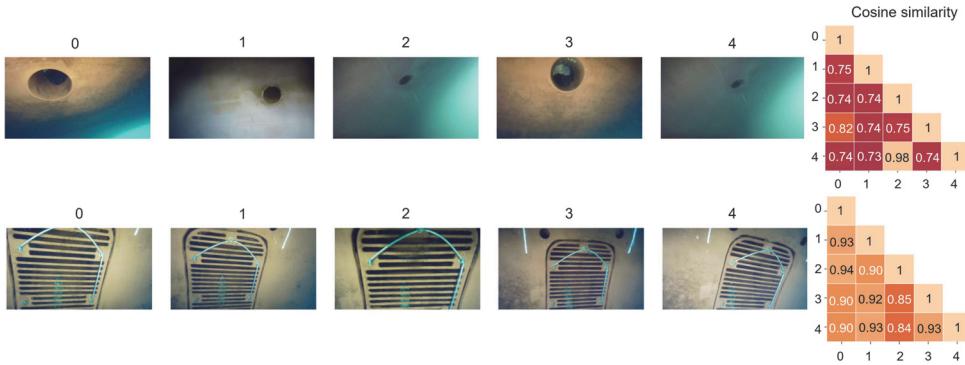
Fig. 7.   Similar images of a sea chest grating and an overboard valve with corresponding pairwise Cosine similarity index.

diversification of classes in images, there is no single combination that makes it possible to find a class based on another. There is then a good distribution/representation of classes in the data set imagewise. There are no strong correlations but some still exist, for example, with the pair propeller/sea chest grating, which is negatively correlated with a value of -0.31. We could think it should be stronger since sea chest gratings are never present on propellers, but some images in the data set contain both at different locations because of the viewpoint of the ROV.

We extracted the images from videos. Therefore, we had grounds to assume that similar images might be among the images in the data set. To quantitatively evaluate how many similar images there are, we calculated a feature vector by extracting the last fully connected layer from the ResNet101 classifier pretrained with ImageNet as provided by PyTorch.[10] We chose ResNet101 as recommended in [21] and an initial naive evaluation provided good results. The calculated image vectors were then used to calculate pairwise Cosine similarity, where an index of 1 means that images are exactly the same and 0 a complete orthogonality. The similarity index follows a normal distribution with a mean and standard deviation of 0.64 ± 0.07, indicating that we have similar images in our data set since the closer the values are to 1, the higher the similarity. Fig. 7 shows example similar images of a sea chest grating and an overboard valve. For different cut-off values for the Cosine similarity measure, Fig. 8 shows the number of unique images in the data set. If we were to choose a cut-off at 0.90 and consider the same labels are present, the data set will still have 1561 images left. Thus, this is the value we recommend to filter out images that are too similar as also confirmed by a qualitative visual evaluation.

III.   BENCHMARK EVALUATION

This section describes the motivation behind the chosen segmentation models for the benchmarking evaluation and presents the results of the evaluation in detail. It is done using multiple combinations of encoders and decoders to prove the capability

[10][Online]. Available: https://pypi.org/project/img2vec-pytorch/
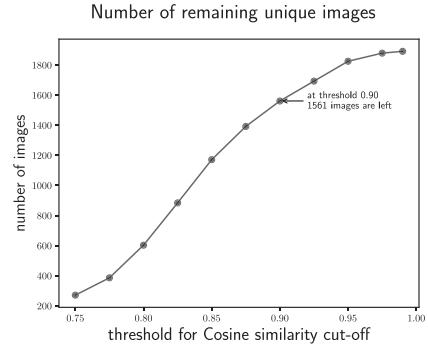
Fig. 8.   Number of remaining images after filtering at different thresholds of the Cosine similarity metric and same classes being present on the image.

of the data set to be used for training and converge at a reasonable rate.

A.   Semantic Segmentation Models

For the benchmark evaluation, multiple state-of-the-art deep convolutional neural network (CNN) models were considered. Often, CNN models can be divided into two parts: an encoder and a decoder. The way the layers are arranged in the encoder network corresponds to the architectural element called backbone. For example, a model such as MobileNetV2 can be used as an encoder for the UNet model, which retains the decoding layers [22]. During the evaluation, backbones based on other models were often included instead of vanilla CNNs; these were pretrained on ImageNet [5]. Also, some segmentation models were utilized multiple times but with different backbones. The complete list of models is displayed in Table IV.

All the models were implemented in Python using the TensorFlow libraries [30]. The same hardware setup is used for all models: NTNU IDUN computing cluster [31], with an NVIDIA Tesla P100 GPU for training, and a laptop with an NVIDIA Geforce GTX 1060 for testing. For the training, the data set was augmented by applying random image transformations

TABLE IV
LIST OF SEGMENTATION MODELS AND THEIR BACKBONES USED FOR THE BENCHMARK ALONG WITH THEIR NUMBER OF PARAMETERS, INPUT RESOLUTION, AND AVERAGE INFERENCE FRAME RATE AS COMPUTED ON A SINGLE NVIDIA GTX 1060 GPU

Referred as	Segmentation model	Backbone	Number of parameters	Resolution	FPS
UNet+MobileNetV2	UNet [23]	MobileNetV2 [24]	8,048 M	320 × 256	23.17
UNet+VGG	UNet [23]	VGG16 [25]	23,753 M	320 × 256	17.86
DeepLabV3	DeepLabV3 [26]	Vanilla	41,256 M	320 × 320	10.91
FPN+MobileNetV2	FPN [27]	MobileNetV2 [24]	5,220 M	320 × 256	17.16
FPN+ResNet50	FPN [27]	ResNet50 [28]	26,922 M	320 × 256	14.71
PSP+MobileNetV2	PSP [29]	MobileNetV2 [24]	1,662 M	336 × 336	25.68
SegNet+ResNet50	SegNet [3]	ResNet50 [28]	15,014 M	320 × 256	18.44
SuimNet+RSB	SuimNet [9]	RSB [9]	3,866 M	320 × 240	17.96
SuimNet+VGG	SuimNet [9]	VGG16 [25]	12,228 M	320 × 256	16.01

from a defined list. They consisted of rotation, shear and zoom effects, as well as, horizontal flip and slight brightness shift. This augmentation was done in addition to image removal based on the similarity measure. This might have made the models less accurate but able to generalize better.

After filtering the data set based on the similarity metric presented in Section II-C with a threshold of 0.90, we divided the remaining 1561 images into a training subset composed of 1370 (87.8%) images and a testing subset with 191 (12.2%) images. These numbers are the result of ensuring a uniform distribution of classes in the training and testing subsets.

B. Evaluation Criteria

To measure the performance of the models, multiple criteria were considered. To evaluate the correctness of the pixelwise classification, two supervised evaluation methods were utilized: the Intersection over Union (IoU) and the F1 Score. The former, also known as the Jaccard Index, is one of the most used metrics for semantic segmentation tasks. It consists of the area of overlap between the predicted masks and the ground truth divided by the area of union between the prediction and the ground truth

$$IoU = \frac{\text{Area of overlap}}{\text{Area of union}}$$
$$= \frac{\text{True Positive}}{\text{True Positive} + \text{False Positive} + \text{False Negative}}. \quad (2)$$

It is also regarded as a region similarity metric.

The latter is also called the dice coefficient and provides the contour accuracy $\mathcal{F}1$

$$\mathcal{F}1 = \frac{2 \times \mathcal{P} \times \mathcal{R}}{\mathcal{P} + \mathcal{R}}. \quad (3)$$

It is defined as the harmonic mean of the precision $\mathcal{P}$ and recall $\mathcal{R}$ of the model.

Also, for the considered applications, time constraints are present. Therefore, the inference time needs to be taken into account. For real-time capabilities, a minimum of ten frames per second (FPS) are required. Also, because the segmentation task needs to be performed during data acquisition, it needs to
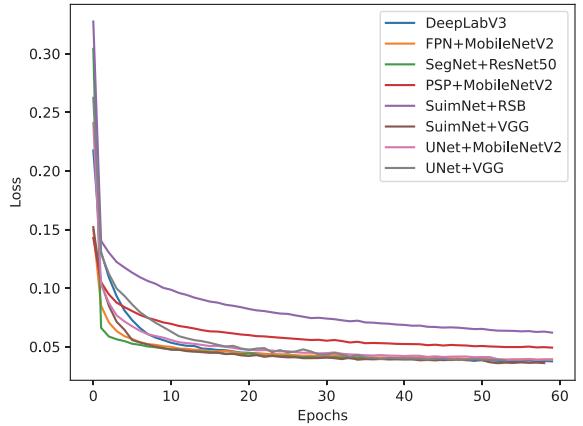
Fig. 9. Training loss over epochs of the considered models until epoch 60.

be possible to run it on the operator laptop which might contain a low-cost GPU or sometimes rely just on the CPU.

C. Quantitative and Qualitative Analysis

A benchmark evaluation with state-of-art deep learning segmentation models showed that good results can be obtained with all of the selected models. Also, all models show similar convergence behavior, with SegNet converging fastest, as depicted in Fig. 9. Table V lists the results of the benchmark evaluation. SegNet with the ResNet50 backbone provides the best results for the class of ship parts with a mean IoU of 86.07 and a mean F1 score of 88.17. The inference time for the PSP model with the MobileNetV2 backbone showed the best time of 25.68 FPS. Over all models, the segmentation accuracy for marine growth and paint peel is not as good compared to other classes. Several reasons could be the cause of this effect. Annotating the classes of marine growth and paints peel is challenging due to high variability of shapes and structures. Also, these label classes tend to naturally overlap as marine growth usually starts growing in areas with paint defects where the antifouling coating is missing. Corrosion also usually appeared on areas with paint

TABLE V
BENCHMARK FOR SEMANTIC SEGMENTATION WITH TWO SCORE METRICS F1 SCORE AND IoU FOR ALL CLASS CATEGORIES

Metric	Model	Ship hull	Propeller	Bilge keel	Anode	Sea chest grating	Overboard valve	Mean	Defect	Corrosion	Paint peel	Marine growth	Mean	Combined
IoU	UNet+MobileNetV2	77.52	83.82	89.13	82.2	90.03	93.06	85.96	92.76	83.36	47.64	61.37	71.28	80.09
	UNet+VGG16	80.81	84.68	88.21	78.75	90.58	91.44	85.74	93.79	81.16	45.98	58.32	69.81	79.37
	PSPNet+MobileNetV2	60.65	67.97	87.38	74.28	86.61	89.74	77.77	95.97	87.98	51.23	54.84	72.50	75.66
	DeeplabV3	74.10	79.04	87.92	74.53	80.72	92.44	81.46	94.82	79.60	37.38	52.20	66.00	75.28
	FPN+MobileNetV2	58.95	73.83	79.22	71.38	65.01	90.06	73.08	95.13	86.61	43.58	45.18	67.63	70.90
	FPN+ResNet50	55.54	65.27	76.07	74.25	48.82	88.09	68.01	95.93	87.76	43.53	47.77	68.74	68.30
	SuimNet+RSB	69.76	66.32	81.61	68.26	78.14	88.51	75.43	92.22	81.75	36.67	45.47	64.03	70.87
	SuimNet+VGG	72.38	73.09	77.57	79.94	83.85	89.61	79.41	94.20	83.56	38.56	54.65	67.74	74.74
	SegNet+ResNet50	76.85	85.46	87.75	80.40	93.80	92.17	86.07	95.83	87.03	43.38	63.62	72.46	80.63
F1 Score	UNet+MobileNetV2	82.26	85.56	90.18	84.25	91.29	93.84	87.90	93.00	84.19	51.82	66.07	73.77	82.25
	UNet+VGG16	85.22	86.04	89.06	81.04	91.95	92.28	87.60	94.04	81.72	50.50	62.71	72.24	81.46
	PSPNet+MobileNetV2	69.86	70.71	88.02	75.70	88.80	90.53	80.6	96.07	88.18	53.16	57.61	73.75	77.86
	DeeplabV3	79.12	81.19	88.78	76.36	82.30	93.14	83.48	95.07	80.06	41.77	55.64	68.13	77.34
	FPN+MobileNetV2	68.07	76.04	79.93	73.39	67.04	91.14	75.93	95.34	86.79	46.02	47.85	69.00	73.16
	FPN+ResNet50	65.52	67.12	77.40	76.11	50.68	88.98	70.97	96.01	87.94	46.19	50.31	70.11	70.63
	SuimNet+RSB	76.19	69.10	82.44	70.62	79.86	89.26	77.91	92.28	81.82	40.10	49.60	65.95	73.13
	SuimNet+VGG	77.98	75.07	78.81	82.08	85.21	90.40	81.59	94.45	84.22	42.90	59.51	70.27	77.06
	SegNet+ResNet50	81.79	87.3	88.88	82.84	95.33	92.89	88.17	96.09	87.58	47.39	67.78	74.71	82.79

peel but is less difficult to label resulting in better prediction results. Therefore, we performed another model training and evaluation round where the classes of marine growth and paint peel were merged. The results show that the accuracy of the merged label class could be increased for all models by almost ten points.

Another observation was that small objects disappeared due to downsampling of the images to the model resolution. Therefore, labels are reduced to only few pixels such that some models are no longer able to detect such areas, e.g., marine growth and paint peel. Dark areas on ship hulls in overboard valves, as well as ship hull areas that were further away from the camera are not correctly identified by the models. Such qualitative observations are depicted in Fig. 10.

IV. FUTURE WORK

Image quality plays a major role in the performance of computer vision algorithms. Hence, seeking to improve image quality retrospectively would improve the results of automated image processing as suggested in [32]. The ULTIR data set [33] or the UIEB [34] could also be used as a starting point for identifying a method to prospectively guide the data acquisition to collect only images with sufficient quality. Image enhancement can be used as a preprocessing task before using it in the model. However, it is computationally expensive and not necessary to reach satisfying results, and hence was not included in this work but remains important for generalization purposes and more robust results. For these reasons, it will be considered in future work.

Our data set was solely collected off the Norwegian Sea. The visibility in waters differs significantly depending on the geographical location and light conditions. Hence, we believe that the data set would benefit from including videos from various waters.

There are several promising directions for future annotations on our data set. We currently only label few ship parts but this could be extended to other parts as the manoeuvring thruster, rudder or box cooler. Also, quantitative evaluation of potential defects inside the vessel water cooling system, which contains the impressed current antifouling anodes and should be monitored closely, could be a target for automated image processing algorithms. Further classes for defects (dents, cracks, rope around parts, scratches, etc.), paint peel (adhesion, blistering, cracking, cold flow, delamination, polishing-off, grounding), and marine growth (soft corals, sponges, hydroids, anemones, algae, tunicates, barnacles, mussels, tube worms, bryozoan, oysters, etc.) could be included in the annotations to follow the guidelines from the International Chamber of Shipping and The Baltic and International Maritime Council [35].

To improve the segmentation results further, the model could account for class correlation, i.e., overboard valves and anodes can only be on a ship hull and not on a propeller. Sea chest grating has to be surrounded by ship hull as well as overboard valves. Introducing such additional constraints would potentially improve model performance and reduce classification errors.

Future work will focus on propagating the segmentation masks onto the whole video to achieve thorough video indexing and to possibly aid algorithms for the calculation of structure from motion, simultaneous localization and mapping, and subsequent 3-D reconstruction of the inspected structures from the video data [36]. Here, the feature extraction step would benefit from adapting its calculation to the segmented object and use different features (e.g., ORB, SIFT) for objects with different semantic and visual properties.

V. CONCLUSION

Semantic understanding of videos in in-water ship inspections is critically important to facilitate quantitative analysis of collected image and video data. The existing solutions are application- and domain-specific as dedicated to the medical domain or autonomous driving for terrestrial vehicles and drones or industrial surface inspections in manufacturing. In this work, we attempt to address these limitations by presenting the first large-scale annotated data set for semantic segmentation of underwater ship inspection images. We described and made available a new
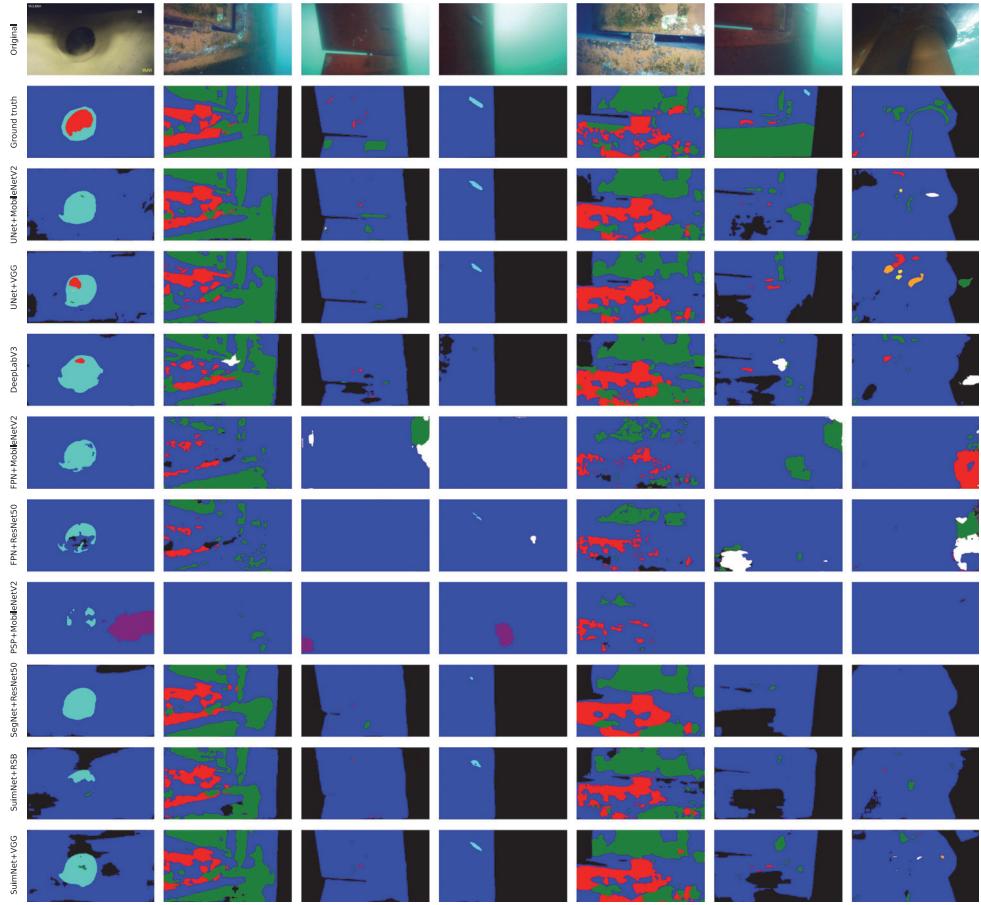
Fig. 10. Qualitative segmentation results for selected classes and models.

data set for detecting and segmenting objects in the domain of visual underwater ship inspections with ROVs. Involving two annotators and a reviewer, a collection of category instances was gathered, annotated, and organized to drive the advancement of object detection and segmentation algorithms. The proposed LIACI data set contains 1893 images with pixel annotations for ten object categories. The benchmark evaluation showed that the UNet segmentation model with the MobileNetV2 backbone provides the best overall performance in terms of segmentation results and inference time making it a good candidate for further investigations. Also, its architecture makes it possible to run the model on a consumer laptop without a GPU with an acceptable frame rate of up to 12 FPS. This is twice the frame rate that can be achieved with the SegNet model with ResNet50 backbone that has a frame rate of 5 FPS on average.

In comparison to humans, it is harder for segmentation models to extrapolate shapes, e.g., ship hull in the shade. The segmentation boundary of the target is not clear enough, the contour is incomplete, and the feature information is insufficient. Here, the annotations would benefit from other data sources as for example

sonar or stereovision cameras. Also, having a 3-D model of the vessel could help to estimate and extrapolate the shape of the seen object. Therefore, enhancing the images with additional data from other sources would improve not only the quality of the annotations but also the model training process.

We also have to conclude that it is very difficult to annotate marine growth, paint peel, and corrosion separately. These classes often appear together and overlap. Therefore, we propose to fuse those classes and run unsupervised segmentation algorithms in a postprocessing step for further refinement.

Also, we deliberately did not exclude blurry images as we would like the data set to reflect the natural quality differences that appear during the data collection. We extracted the images from inspection videos which provided a natural augmentation of the data by providing different views of the objects. For example, the illumination conditions and the water turbidity were naturally changing when the ROV was capturing the object from different distances and angles.

The data set is made available for noncommercial use on https://liaci.sintef.cloud.
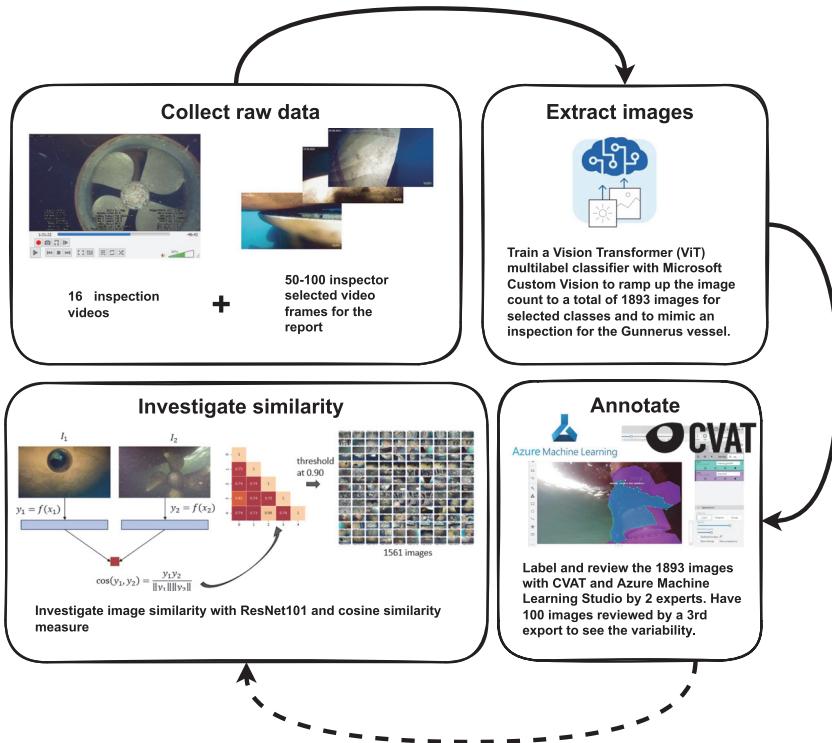
Fig. 11. Steps that were performed to create the data set.

APPENDIX

Fig. 11 shows the steps that were performed to create the data set.

ACKNOWLEDGMENT

REFERENCES

[1] B. Ghosh, M. O'Byrne, F. Schoefs, and V. Pakrashi, *Image Based Damage Assessment for Underwater Inspections*. Boca Raton, FL, USA: CRC, Jan. 2019.

[2] A. Garcia-Garcia, S. Orts-Escolano, S. Oprea, V. Villena-Martinez, P. Martinez-Gonzalez, and J. Garcia-Rodriguez, "A survey on deep learning techniques for image and video semantic segmentation," *Appl. Soft Comput.*, vol. 70, pp. 41–65, 2018.

[3] V. Badrinarayanan, A. Kendall, and R. Cipolla, "Segnet: A deep convolutional encoder-decoder architecture for image segmentation," *IEEE Trans. Pattern Anal. Mach. Intell.*, vol. 39, no. 12, pp. 2481–2495, Dec. 2017.

[4] J. Long, E. Shelhamer, and T. Darrell, "Fully convolutional networks for semantic segmentation," in *Proc. IEEE Conf. Comput. Vis. Pattern Recognit.*, Los Alamitos, CA, USA, 2015, pp. 3431–3440.

[5] J. Deng, W. Dong, R. Socher, L.-J. Li, K. Li, and L. Fei-Fei, "Imagenet: A large-scale hierarchical image database," in *Proc. IEEE Conf. Comput. Vis. Pattern Recognit.*, 2009, pp. 248–255.

[6] B. Zhou, H. Zhao, X. Puig, S. Fidler, A. Barriuso, and A. Torralba, "Scene parsing through ADE20 k dataset," in *Proc. IEEE Conf. Comput. Vis. Pattern Recognit.*, 2017, pp. 5122–5130.

[7] M. Everingham, L. Van Gool, C. K. Williams, J. Winn, and A. Zisserman, "The pascal visual object classes (VOC) challenge," *Int. J. Comput. Vis.*, vol. 88, no. 2, pp. 303–338, 2010.

[8] T.-Y. Lin et al., "Microsoft coco: Common objects in context," in *Computer Vision–ECCV*, D. Fleet, T. Pajdla, B. Schiele, and T. Tuytelaars, Eds. Cham, Switzerland: Springer, 2014, pp. 740–755.

[9] M. J. Islam et al., "Semantic segmentation of underwater imagery: Dataset and benchmark," in *Proc. IEEE/RSJ Int. Conf. Intell. Robots Syst.*, 2020, pp. 1769–1776.

[10] G. Reus et al., "Looking for seagrass: Deep learning for visual coverage estimation," in *Proc. IEEE/MTS OCEANS Conf., - Kobe Techno-Oceans*, 2018, pp. 1–6.

[11] D. Rathi, S. Jain, and S. Indu, "Underwater fish species classification using convolutional neural network and deep learning," in *Proc. 9th Int. Conf. Adv. Pattern Recognit.*, 2017, pp. 1–6.

[12] C. S. Chin, J. Si, A. Clare, and M. Ma, "Intelligent image recognition system for marine fouling using softmax transfer learning and deep convolutional neural networks," *Complexity*, vol. 2017, 2017, Art. no. 5730419.

[13] M. O'Byrne, V. Pakrashi, F. Schoefs, and a. B. Ghosh, "Semantic segmentation of underwater imagery using deep networks trained on synthetic imagery," *J. Mar. Sci. Eng.*, vol. 6, no. 3, Aug. 2018, Art. no. 93.

[14] S. K. Fondevik, A. Stahl, A. A. Transeth, and O. O. Knudsen, "Image segmentation of corrosion damages in industrial inspections," in *Proc. IEEE 32nd Int. Conf. Tools With Artif. Intell.*, 2020, pp. 787–792.

[15] F. Bonnín-Pascual and A. Ortiz, "Detection of cracks and corrosion for automated vessels visual inspection," in *Proc. Int. Conf. Catalan Assoc. Artif. Intell.*, 2010, pp. 111–120.

[16] F. Bonnin-Pascual and A. Ortiz, "A novel approach for defect detection on vessel structures using saliency-related features," *Ocean Eng.*, vol. 149, pp. 397–408, 2018.

[17] K. Yao, A. Ortiz, and F. Bonnin-Pascual, "A weakly-supervised semantic segmentation approach based on the centroid loss: Application to quality control and inspection," *IEEE Access*, vol. 9, pp. 69010–69026, 2021.

[18] F. Liu and M. Fang, "Semantic segmentation of underwater images based on improved deeplab," *J. Mar. Sci. Eng.*, vol. 8, no. 3, Mar. 2020, Art. no. 188.

[19] B. C. Kim, H. C. Kim, S. Han, and D. K. Park, "Inspection of underwater hull surface condition using the soft voting ensemble of the transfer-learned models," *Sensors*, vol. 22, no. 12, 2022, Art. no. 4392.

[20] A. Dosovitskiy et al., "An image is worth 16x16 words: Transformers for image recognition at scale," in *Proc. 9th Int. Conf. Learn. Representations*, 2021.

[21] K. He, X. Zhang, S. Ren, and J. Sun, "Deep residual learning for image recognition," in *Proc. IEEE Conf. Comput. Vis. Pattern Recognit.*, 2016, pp. 770–778.

[22] A. Kanadath, J. A. A. Jothi, and S. Urolagin, "Histopathology image segmentation using mobilenetv2 based U-net model," in *Proc. Int. Conf. Intell. Technol.*, 2021, pp. 1–8.

[23] O. Ronneberger, P. Fischer, and T. Brox, "U-net: Convolutional networks for biomedical image segmentation," in *Medical Image Computing and Computer-Assisted Intervention (MICCAI)*, vol. 9351. Berlin, Germany: Springer, 2015, pp. 234–241.

[24] M. Sandler, A. G. Howard, M. Zhu, A. Zhmoginov, and L.-C. Chen, "Mobilenetv2: Inverted residuals and linear bottlenecks," in *Proc. IEEE/CVF Conf. Comput. Vis. Pattern Recognit.*, 2018, pp. 4510–4520.

[25] K. Simonyan and A. Zisserman, "Very deep convolutional networks for large-scale image recognition," in *Proc. 3rd Int. Conf. Learn. Representations*, 2015, pp. 1–14.

[26] L.-C. Chen, G. Papandreou, F. Schroff, and H. Adam, "Rethinking atrous convolution for semantic image segmentation," 2017, *arXiv:1706.05587*.

[27] T.-Y. Lin, P. Dollár, R. Girshick, K. He, B. Hariharan, and S. Belongie, "Feature pyramid networks for object detection," in *Proc. IEEE Conf. Comput. Vis. Pattern Recognit.*, 2017, pp. 936–944.

[28] K. He, X. Zhang, S. Ren, and J. Sun, "Deep residual learning for image recognition," in *Proc. IEEE Conf. Comput. Vis. Pattern Recognit.*, 2016, pp. 770–778.

[29] H. Zhao, J. Shi, X. Qi, X. Wang, and J. Jia, "Pyramid scene parsing network," in *Proc. IEEE Conf. Comput. Vis. Pattern Recognit.*, 2017, pp. 6230–6239.

[30] M. Abadi et al., "Tensorflow: A system for large-scale machine learning," in *Proc. 12th USENIX Symp. Oper. Syst. Des. Implementation*, 2016, pp. 265–283.

[31] M. Själander, M. Jahre, G. Tufte, and N. Reissmann, "EPIC: An energy-efficient, high-performance GPGPU computing research infrastructure," 2019, *arXiv:1912.05848*.

[32] M. J. Islam, Y. Xia, and J. Sattar, "Fast underwater image enhancement for improved visual perception," *IEEE Robot. Automat. Lett.*, vol. 5, no. 2, pp. 3227–3234, Apr. 2020.

[33] M. O'Byrne, F. Schoefs, V. Pakrashi, and B. Ghosh, "An underwater lighting and turbidity image repository for analysing the performance of image-based non-destructive techniques," *Struct. Infrastructure Eng.*, vol. 14, no. 1, pp. 104–123, Jan. 2018.

[34] C. Li et al., "An underwater image enhancement benchmark dataset and beyond," *IEEE Trans. Image Process.*, vol. 29, pp. 4376–4389, 2020.

[35] *International Chamber of Shipping and the Baltic and International Maritime Council*, Industry Standard on In-Water Cleaning With Capture, vol. 1, London, U.K., Feb. 2021. [Online]. Available: https://www.ics-shipping.org/publication/industry-standard-on-in-water-cleaning-with-capture

[36] S. Hong and J. Kim, "Three-dimensional visual mapping of underwater ship hull surface using piecewise-planar slam," *Int. J. Control, Automat. Syst.*, vol. 18, no. 3, pp. 564–574, 2020.

Maryna Waszak (Member, IEEE) received the Ph.D. degree in electrical engineering from the École polytechnique fédérale de Lausanne, Lausanne, Switzerland, in 2016, and developed a new motion correction technique for magnetic resonance imaging.

She is a Research Scientist with SINTEF Digital Smart Data Group, Oslo, Norway. The expertise of the group focuses on the fusion of data of different modalities and from highly heterogeneous sources. Her current research work is tailored around applications in the processing industry in the context of digital twins.

Alexandre Cardaillac received the Bachelor of Information Technology from the School of Digital Innovation, Nantes, France, in 2019 and the M.Sc. degree in artificial intelligence with speech and multimodal interaction from Heriot-Watt University, Edinburgh, UK, in 2020. He is currently working toward the Ph.D. degree in engineering with the Department of Marine Technology, Norwegian University of Science and Technology, Trondheim, Norway.

Brian Elvesæter received the Cand.scient. degree in computer science from the University of Oslo, Oslo, Norway, in 2000.

He is a Senior Research Scientist with the Department for Sustainable Communication Technologies, SINTEF Digital. His current research interests include data management and data pipelines, knowledge graphs and semantic technologies, and AI and graph analytics.

Frode Rødølen received the Diploma from the Maritime Highschool, Bergen, Norway, in 1999.

He is the Founder and CEO of VUVI AS, Bergen, Norway. VUVI is a frontrunner in using ROV for surveys on ship hulls and is an approved supplier to the Norwegian Maritime Authorities, DNV, Lloyd's Register, Rina, CCS, and Bureau Veritas vessels. Since the commencement of operations, VUVI has executed more than 350 vessel inspections. He has more than 20 years of experience and has learned how to use and modify small inspection class ROV's to inspect ship hulls. He is passionate about lifelong learning, entrepreneurship, and social responsibility through nonprofit work, and he welcomes opportunities to explore, especially the ocean.

Martin Ludvigsen (Member, IEEE) was born in 1977. He received the Ph.D. degree in underwater technology from the Norges Teknisk-Naturvitenskapelige Universitet, Trondheim, Norway, in 2010.

Since 2014, he has been a Professor with the Department of Marine Technology, Norwegian University of Science and Technology (NTNU), Trondheim, Norway. He is a Cofounder and Manager for the Applied Underwater Laboratory (AUR-Lab) with NTNU. The AUR-Lab (https://www.ntnu.edu/web/aur-lab/aur-lab) facilitates research within both engineering disciplines and marine science by providing ROV, AUV, and USV operations. He has long experience at-sea both in arctic waters as well as in benthic environments associated with the Norwegian midocean ridge. He has been involved in research projects both in the deep sea, the upper water column, and arctic deploying robotic underwater vehicles. His research interests cover the field of underwater vehicles including perception and interpretation of cameras and sonar data together with autonomy. Adaptive mission planning for one or more vehicles for ocean column mapping has also been a focus point for his research group.

Previous PhD theses published at the Department of Marine Technology
(earlier: Faculty of Marine Technology)
NORWEGIAN UNIVERSITY OF SCIENCE AND TECHNOLOGY

Report No.	Author	Title
	Kavlie, Dag	Optimization of Plane Elastic Grillages, 1967
	Hansen, Hans R.	Man-Machine Communication and Data-Storage Methods in Ship Structural Design, 1971
	Gisvold, Kaare M.	A Method for non-linear mixed -integer programming and its Application to Design Problems, 1971
	Lund, Sverre	Tanker Frame Optimalization by means of SUMT-Transformation and Behaviour Models, 1971
	Vinje, Tor	On Vibration of Spherical Shells Interacting with Fluid, 1972
	Lorentz, Jan D.	Tank Arrangement for Crude Oil Carriers in Accordance with the new Anti-Pollution Regulations, 1975
	Carlsen, Carl A.	Computer-Aided Design of Tanker Structures, 1975
	Larsen, Carl M.	Static and Dynamic Analysis of Offshore Pipelines during Installation, 1976
UR-79-01	Brigt Hatlestad, MK	The finite element method used in a fatigue evaluation of fixed offshore platforms. (Dr.Ing. Thesis)
UR-79-02	Erik Pettersen, MK	Analysis and design of cellular structures. (Dr.Ing. Thesis)
UR-79-03	Sverre Valsgård, MK	Finite difference and finite element methods applied to nonlinear analysis of plated structures. (Dr.Ing. Thesis)
UR-79-04	Nils T. Nordsve, MK	Finite element collapse analysis of structural members considering imperfections and stresses due to fabrication. (Dr.Ing. Thesis)
UR-79-05	Ivar J. Fylling, MK	Analysis of towline forces in ocean towing systems. (Dr.Ing. Thesis)
UR-79- x	Finn Gunnar Nielsen, MH	Hydrodynamic problems related to oil barriers for offshore application
UR-80-06	Nils Sandsmark, MM	Analysis of Stationary and Transient Heat Conduction by the Use of the Finite Element Method. (Dr.Ing. Thesis)
UR-80-09	Sverre Haver, MK	Analysis of uncertainties related to the stochastic modeling of ocean waves. (Dr.Ing. Thesis)

UR-81-15	Odland, Jonas	On the Strength of welded Ring stiffened cylindrical Shells primarily subjected to axial Compression
UR-82-17	Engesvik, Knut	Analysis of Uncertainties in the fatigue Capacity of Welded Joints
UR-82-18	Rye, Henrik	Ocean wave groups
UR-83-30	Eide, Oddvar Inge	On Cumulative Fatigue Damage in Steel Welded Joints
UR-83-33	Mo, Olav	Stochastic Time Domain Analysis of Slender Offshore Structures
UR-83-34	Amdahl, Jørgen	Energy absorption in Ship-platform impacts
UR-84-37	Mørch, Morten	Motions and mooring forces of semi submersibles as determined by full-scale measurements and theoretical analysis
UR-84-38	Soares, C. Guedes	Probabilistic models for load effects in ship structures
UR-84-39	Aarsnes, Jan V.	Current forces on ships
UR-84-40	Czujko, Jerzy	Collapse Analysis of Plates subjected to Biaxial Compression and Lateral Load
UR-85-46	Alf G. Engseth, MK	Finite element collapse analysis of tubular steel offshore structures. (Dr.Ing. Thesis)
UR-86-47	Dengody Sheshappa, MP	A Computer Design Model for Optimizing Fishing Vessel Designs Based on Techno-Economic Analysis. (Dr.Ing. Thesis)
UR-86-48	Vidar Aanesland, MH	A Theoretical and Numerical Study of Ship Wave Resistance. (Dr.Ing. Thesis)
UR-86-49	Heinz-Joachim Wessel, MK	Fracture Mechanics Analysis of Crack Growth in Plate Girders. (Dr.Ing. Thesis)
UR-86-50	Jon Taby, MK	Ultimate and Post-ultimate Strength of Dented Tubular Members. (Dr.Ing. Thesis)
UR-86-51	Walter Lian, MH	A Numerical Study of Two-Dimensional Separated Flow Past Bluff Bodies at Moderate KC-Numbers. (Dr.Ing. Thesis)
UR-86-52	Bjørn Sortland, MH	Force Measurements in Oscillating Flow on Ship Sections and Circular Cylinders in a U-Tube Water Tank. (Dr.Ing. Thesis)
UR-86-53	Kurt Strand, MM	A System Dynamic Approach to One-dimensional Fluid Flow. (Dr.Ing. Thesis)
UR-86-54	Arne Edvin Løken, MH	Three Dimensional Second Order Hydrodynamic Effects on Ocean Structures in Waves. (Dr.Ing. Thesis)

UR-86-55	Sigurd Falch, MH	A Numerical Study of Slamming of Two-Dimensional Bodies. (Dr.Ing. Thesis)
UR-87-56	Arne Braathen, MH	Application of a Vortex Tracking Method to the Prediction of Roll Damping of a Two-Dimension Floating Body. (Dr.Ing. Thesis)
UR-87-57	Bernt Leira, MK	Gaussian Vector Processes for Reliability Analysis involving Wave-Induced Load Effects. (Dr.Ing. Thesis)
UR-87-58	Magnus Småvik, MM	Thermal Load and Process Characteristics in a Two-Stroke Diesel Engine with Thermal Barriers (in Norwegian). (Dr.Ing. Thesis)
MTA-88-59	Bernt Arild Bremdal, MP	An Investigation of Marine Installation Processes – A Knowledge - Based Planning Approach. (Dr.Ing. Thesis)
MTA-88-60	Xu Jun, MK	Non-linear Dynamic Analysis of Space-framed Offshore Structures. (Dr.Ing. Thesis)
MTA-89-61	Gang Miao, MH	Hydrodynamic Forces and Dynamic Responses of Circular Cylinders in Wave Zones. (Dr.Ing. Thesis)
MTA-89-62	Martin Greenhow, MH	Linear and Non-Linear Studies of Waves and Floating Bodies. Part I and Part II. (Dr.Techn. Thesis)
MTA-89-63	Chang Li, MH	Force Coefficients of Spheres and Cubes in Oscillatory Flow with and without Current. (Dr.Ing. Thesis
MTA-89-64	Hu Ying, MP	A Study of Marketing and Design in Development of Marine Transport Systems. (Dr.Ing. Thesis)
MTA-89-65	Arild Jæger, MH	Seakeeping, Dynamic Stability and Performance of a Wedge Shaped Planing Hull. (Dr.Ing. Thesis)
MTA-89-66	Chan Siu Hung, MM	The dynamic characteristics of tilting-pad bearings
MTA-89-67	Kim Wikstrøm, MP	Analysis av projekteringen for ett offshore projekt. (Licenciat-avhandling)
MTA-89-68	Jiao Guoyang, MK	Reliability Analysis of Crack Growth under Random Loading, considering Model Updating. (Dr.Ing. Thesis)
MTA-89-69	Arnt Olufsen, MK	Uncertainty and Reliability Analysis of Fixed Offshore Structures. (Dr.Ing. Thesis)
MTA-89-70	Wu Yu-Lin, MR	System Reliability Analyses of Offshore Structures using improved Truss and Beam Models. (Dr.Ing. Thesis)
MTA-90-71	Jan Roger Hoff, MH	Three-dimensional Green function of a vessel with forward speed in waves. (Dr.Ing. Thesis)
MTA-90-72	Rong Zhao, MH	Slow-Drift Motions of a Moored Two-Dimensional Body in Irregular Waves. (Dr.Ing. Thesis)

MTA-90-73	Atle Minsaas, MP	Economical Risk Analysis. (Dr.Ing. Thesis)
MTA-90-74	Knut-Aril Farnes, MK	Long-term Statistics of Response in Non-linear Marine Structures. (Dr.Ing. Thesis)
MTA-90-75	Torbjørn Sotberg, MK	Application of Reliability Methods for Safety Assessment of Submarine Pipelines. (Dr.Ing. Thesis)
MTA-90-76	Zeuthen, Steffen, MP	SEAMAID. A computational model of the design process in a constraint-based logic programming environment. An example from the offshore domain. (Dr.Ing. Thesis)
MTA-91-77	Haagensen, Sven, MM	Fuel Dependant Cyclic Variability in a Spark Ignition Engine - An Optical Approach. (Dr.Ing. Thesis)
MTA-91-78	Løland, Geir, MH	Current forces on and flow through fish farms. (Dr.Ing. Thesis)
MTA-91-79	Hoen, Christopher, MK	System Identification of Structures Excited by Stochastic Load Processes. (Dr.Ing. Thesis)
MTA-91-80	Haugen, Stein, MK	Probabilistic Evaluation of Frequency of Collision between Ships and Offshore Platforms. (Dr.Ing. Thesis)
MTA-91-81	Sødahl, Nils, MK	Methods for Design and Analysis of Flexible Risers. (Dr.Ing. Thesis)
MTA-91-82	Ormberg, Harald, MK	Non-linear Response Analysis of Floating Fish Farm Systems. (Dr.Ing. Thesis)
MTA-91-83	Marley, Mark J., MK	Time Variant Reliability under Fatigue Degradation. (Dr.Ing. Thesis)
MTA-91-84	Krokstad, Jørgen R., MH	Second-order Loads in Multidirectional Seas. (Dr.Ing. Thesis)
MTA-91-85	Molteberg, Gunnar A., MM	The Application of System Identification Techniques to Performance Monitoring of Four Stroke Turbocharged Diesel Engines. (Dr.Ing. Thesis)
MTA-92-86	Mørch, Hans Jørgen Bjelke, MH	Aspects of Hydrofoil Design: with Emphasis on Hydrofoil Interaction in Calm Water. (Dr.Ing. Thesis)
MTA-92-87	Chan Siu Hung, MM	Nonlinear Analysis of Rotordynamic Instabilities in Highspeed Turbomachinery. (Dr.Ing. Thesis)
MTA-92-88	Bessason, Bjarni, MK	Assessment of Earthquake Loading and Response of Seismically Isolated Bridges. (Dr.Ing. Thesis)
MTA-92-89	Langli, Geir, MP	Improving Operational Safety through exploitation of Design Knowledge - an investigation of offshore platform safety. (Dr.Ing. Thesis)
MTA-92-90	Sævik, Svein, MK	On Stresses and Fatigue in Flexible Pipes. (Dr.Ing. Thesis)

MTA-92-91	Ask, Tor Ø., MM	Ignition and Flame Growth in Lean Gas-Air Mixtures. An Experimental Study with a Schlieren System. (Dr.Ing. Thesis)
MTA-86-92	Hessen, Gunnar, MK	Fracture Mechanics Analysis of Stiffened Tubular Members. (Dr.Ing. Thesis)
MTA-93-93	Steinebach, Christian, MM	Knowledge Based Systems for Diagnosis of Rotating Machinery. (Dr.Ing. Thesis)
MTA-93-94	Dalane, Jan Inge, MK	System Reliability in Design and Maintenance of Fixed Offshore Structures. (Dr.Ing. Thesis)
MTA-93-95	Steen, Sverre, MH	Cobblestone Effect on SES. (Dr.Ing. Thesis)
MTA-93-96	Karunakaran, Daniel, MK	Nonlinear Dynamic Response and Reliability Analysis of Drag-dominated Offshore Platforms. (Dr.Ing. Thesis)
MTA-93-97	Hagen, Arnulf, MP	The Framework of a Design Process Language. (Dr.Ing. Thesis)
MTA-93-98	Nordrik, Rune, MM	Investigation of Spark Ignition and Autoignition in Methane and Air Using Computational Fluid Dynamics and Chemical Reaction Kinetics. A Numerical Study of Ignition Processes in Internal Combustion Engines. (Dr.Ing. Thesis)
MTA-94-99	Passano, Elizabeth, MK	Efficient Analysis of Nonlinear Slender Marine Structures. (Dr.Ing. Thesis)
MTA-94-100	Kvålsvold, Jan, MH	Hydroelastic Modelling of Wetdeck Slamming on Multihull Vessels. (Dr.Ing. Thesis)
MTA-94-102	Bech, Sidsel M., MK	Experimental and Numerical Determination of Stiffness and Strength of GRP/PVC Sandwich Structures. (Dr.Ing. Thesis)
MTA-95-103	Paulsen, Hallvard, MM	A Study of Transient Jet and Spray using a Schlieren Method and Digital Image Processing. (Dr.Ing. Thesis)
MTA-95-104	Hovde, Geir Olav, MK	Fatigue and Overload Reliability of Offshore Structural Systems, Considering the Effect of Inspection and Repair. (Dr.Ing. Thesis)
MTA-95-105	Wang, Xiaozhi, MK	Reliability Analysis of Production Ships with Emphasis on Load Combination and Ultimate Strength. (Dr.Ing. Thesis)
MTA-95-106	Ulstein, Tore, MH	Nonlinear Effects of a Flexible Stern Seal Bag on Cobblestone Oscillations of an SES. (Dr.Ing. Thesis)
MTA-95-107	Solaas, Frøydis, MH	Analytical and Numerical Studies of Sloshing in Tanks. (Dr.Ing. Thesis)
MTA-95-108	Hellan, Øyvind, MK	Nonlinear Pushover and Cyclic Analyses in Ultimate Limit State Design and Reassessment of Tubular Steel Offshore Structures. (Dr.Ing. Thesis)

MTA-95-109	Hermundstad, Ole A., MK	Theoretical and Experimental Hydroelastic Analysis of High Speed Vessels. (Dr.Ing. Thesis)
MTA-96-110	Bratland, Anne K., MH	Wave-Current Interaction Effects on Large-Volume Bodies in Water of Finite Depth. (Dr.Ing. Thesis)
MTA-96-111	Herfjord, Kjell, MH	A Study of Two-dimensional Separated Flow by a Combination of the Finite Element Method and Navier-Stokes Equations. (Dr.Ing. Thesis)
MTA-96-112	Æsøy, Vilmar, MM	Hot Surface Assisted Compression Ignition in a Direct Injection Natural Gas Engine. (Dr.Ing. Thesis)
MTA-96-113	Eknes, Monika L., MK	Escalation Scenarios Initiated by Gas Explosions on Offshore Installations. (Dr.Ing. Thesis)
MTA-96-114	Erikstad, Stein O., MP	A Decision Support Model for Preliminary Ship Design. (Dr.Ing. Thesis)
MTA-96-115	Pedersen, Egil, MH	A Nautical Study of Towed Marine Seismic Streamer Cable Configurations. (Dr.Ing. Thesis)
MTA-97-116	Moksnes, Paul O., MM	Modelling Two-Phase Thermo-Fluid Systems Using Bond Graphs. (Dr.Ing. Thesis)
MTA-97-117	Halse, Karl H., MK	On Vortex Shedding and Prediction of Vortex-Induced Vibrations of Circular Cylinders. (Dr.Ing. Thesis)
MTA-97-118	Igland, Ragnar T., MK	Reliability Analysis of Pipelines during Laying, considering Ultimate Strength under Combined Loads. (Dr.Ing. Thesis)
MTA-97-119	Pedersen, Hans-P., MP	Levendefiskteknologi for fiskefartøy. (Dr.Ing. Thesis)
MTA-98-120	Vikestad, Kyrre, MK	Multi-Frequency Response of a Cylinder Subjected to Vortex Shedding and Support Motions. (Dr.Ing. Thesis)
MTA-98-121	Azadi, Mohammad R. E., MK	Analysis of Static and Dynamic Pile-Soil-Jacket Behaviour. (Dr.Ing. Thesis)
MTA-98-122	Ulltang, Terje, MP	A Communication Model for Product Information. (Dr.Ing. Thesis)
MTA-98-123	Torbergsen, Erik, MM	Impeller/Diffuser Interaction Forces in Centrifugal Pumps. (Dr.Ing. Thesis)
MTA-98-124	Hansen, Edmond, MH	A Discrete Element Model to Study Marginal Ice Zone Dynamics and the Behaviour of Vessels Moored in Broken Ice. (Dr.Ing. Thesis)
MTA-98-125	Videiro, Paulo M., MK	Reliability Based Design of Marine Structures. (Dr.Ing. Thesis)
MTA-99-126	Mainçon, Philippe, MK	Fatigue Reliability of Long Welds Application to Titanium Risers. (Dr.Ing. Thesis)

MTA-99-127	Haugen, Elin M., MH	Hydroelastic Analysis of Slamming on Stiffened Plates with Application to Catamaran Wetdecks. (Dr.Ing. Thesis)
MTA-99-128	Langhelle, Nina K., MK	Experimental Validation and Calibration of Nonlinear Finite Element Models for Use in Design of Aluminium Structures Exposed to Fire. (Dr.Ing. Thesis)
MTA-99-129	Berstad, Are J., MK	Calculation of Fatigue Damage in Ship Structures. (Dr.Ing. Thesis)
MTA-99-130	Andersen, Trond M., MM	Short Term Maintenance Planning. (Dr.Ing. Thesis)
MTA-99-131	Tveiten, Bård Wathne, MK	Fatigue Assessment of Welded Aluminium Ship Details. (Dr.Ing. Thesis)
MTA-99-132	Søreide, Fredrik, MP	Applications of underwater technology in deep water archaeology. Principles and practice. (Dr.Ing. Thesis)
MTA-99-133	Tønnessen, Rune, MH	A Finite Element Method Applied to Unsteady Viscous Flow Around 2D Blunt Bodies With Sharp Corners. (Dr.Ing. Thesis)
MTA-99-134	Elvekrok, Dag R., MP	Engineering Integration in Field Development Projects in the Norwegian Oil and Gas Industry. The Supplier Management of Norne. (Dr.Ing. Thesis)
MTA-99-135	Fagerholt, Kjetil, MP	Optimeringsbaserte Metoder for Ruteplanlegging innen skipsfart. (Dr.Ing. Thesis)
MTA-99-136	Bysveen, Marie, MM	Visualization in Two Directions on a Dynamic Combustion Rig for Studies of Fuel Quality. (Dr.Ing. Thesis)
MTA-2000-137	Storteig, Eskild, MM	Dynamic characteristics and leakage performance of liquid annular seals in centrifugal pumps. (Dr.Ing. Thesis)
MTA-2000-138	Sagli, Gro, MK	Model uncertainty and simplified estimates of long term extremes of hull girder loads in ships. (Dr.Ing. Thesis)
MTA-2000-139	Tronstad, Harald, MK	Nonlinear analysis and design of cable net structures like fishing gear based on the finite element method. (Dr.Ing. Thesis)
MTA-2000-140	Kroneberg, André, MP	Innovation in shipping by using scenarios. (Dr.Ing. Thesis)
MTA-2000-141	Haslum, Herbjørn Alf, MH	Simplified methods applied to nonlinear motion of spar platforms. (Dr.Ing. Thesis)
MTA-2001-142	Samdal, Ole Johan, MM	Modelling of Degradation Mechanisms and Stressor Interaction on Static Mechanical Equipment Residual Lifetime. (Dr.Ing. Thesis)
MTA-2001-143	Baarholm, Rolf Jarle, MH	Theoretical and experimental studies of wave impact underneath decks of offshore platforms. (Dr.Ing. Thesis)

MTA-2001-144	Wang, Lihua, MK	Probabilistic Analysis of Nonlinear Wave-induced Loads on Ships. (Dr.Ing. Thesis)
MTA-2001-145	Kristensen, Odd H. Holt, MK	Ultimate Capacity of Aluminium Plates under Multiple Loads, Considering HAZ Properties. (Dr.Ing. Thesis)
MTA-2001-146	Greco, Marilena, MH	A Two-Dimensional Study of Green-Water Loading. (Dr.Ing. Thesis)
MTA-2001-147	Heggelund, Svein E., MK	Calculation of Global Design Loads and Load Effects in Large High Speed Catamarans. (Dr.Ing. Thesis)
MTA-2001-148	Babalola, Olusegun T., MK	Fatigue Strength of Titanium Risers – Defect Sensitivity. (Dr.Ing. Thesis)
MTA-2001-149	Mohammed, Abuu K., MK	Nonlinear Shell Finite Elements for Ultimate Strength and Collapse Analysis of Ship Structures. (Dr.Ing. Thesis)
MTA-2002-150	Holmedal, Lars E., MH	Wave-current interactions in the vicinity of the sea bed. (Dr.Ing. Thesis)
MTA-2002-151	Rognebakke, Olav F., MH	Sloshing in rectangular tanks and interaction with ship motions. (Dr.Ing. Thesis)
MTA-2002-152	Lader, Pål Furset, MH	Geometry and Kinematics of Breaking Waves. (Dr.Ing. Thesis)
MTA-2002-153	Yang, Qinzheng, MH	Wash and wave resistance of ships in finite water depth. (Dr.Ing. Thesis)
MTA-2002-154	Melhus, Øyvin, MM	Utilization of VOC in Diesel Engines. Ignition and combustion of VOC released by crude oil tankers. (Dr.Ing. Thesis)
MTA-2002-155	Ronæss, Marit, MH	Wave Induced Motions of Two Ships Advancing on Parallel Course. (Dr.Ing. Thesis)
MTA-2002-156	Økland, Ole D., MK	Numerical and experimental investigation of whipping in twin hull vessels exposed to severe wet deck slamming. (Dr.Ing. Thesis)
MTA-2002-157	Ge, Chunhua, MK	Global Hydroelastic Response of Catamarans due to Wet Deck Slamming. (Dr.Ing. Thesis)
MTA-2002-158	Byklum, Eirik, MK	Nonlinear Shell Finite Elements for Ultimate Strength and Collapse Analysis of Ship Structures. (Dr.Ing. Thesis)
IMT-2003-1	Chen, Haibo, MK	Probabilistic Evaluation of FPSO-Tanker Collision in Tandem Offloading Operation. (Dr.Ing. Thesis)
IMT-2003-2	Skaugset, Kjetil Bjørn, MK	On the Suppression of Vortex Induced Vibrations of Circular Cylinders by Radial Water Jets. (Dr.Ing. Thesis)
IMT-2003-3	Chezhian, Muthu	Three-Dimensional Analysis of Slamming. (Dr.Ing. Thesis)

IMT-2003-4	Buhaug, Øyvind	Deposit Formation on Cylinder Liner Surfaces in Medium Speed Engines. (Dr.Ing. Thesis)
IMT-2003-5	Tregde, Vidar	Aspects of Ship Design: Optimization of Aft Hull with Inverse Geometry Design. (Dr.Ing. Thesis)
IMT-2003-6	Wist, Hanne Therese	Statistical Properties of Successive Ocean Wave Parameters. (Dr.Ing. Thesis)
IMT-2004-7	Ransau, Samuel	Numerical Methods for Flows with Evolving Interfaces. (Dr.Ing. Thesis)
IMT-2004-8	Soma, Torkel	Blue-Chip or Sub-Standard. A data interrogation approach of identity safety characteristics of shipping organization. (Dr.Ing. Thesis)
IMT-2004-9	Ersdal, Svein	An experimental study of hydrodynamic forces on cylinders and cables in near axial flow. (Dr.Ing. Thesis)
IMT-2005-10	Brodtkorb, Per Andreas	The Probability of Occurrence of Dangerous Wave Situations at Sea. (Dr.Ing. Thesis)
IMT-2005-11	Yttervik, Rune	Ocean current variability in relation to offshore engineering. (Dr.Ing. Thesis)
IMT-2005-12	Fredheim, Arne	Current Forces on Net-Structures. (Dr.Ing. Thesis)
IMT-2005-13	Heggernes, Kjetil	Flow around marine structures. (Dr.Ing. Thesis
IMT-2005-14	Fouques, Sebastien	Lagrangian Modelling of Ocean Surface Waves and Synthetic Aperture Radar Wave Measurements. (Dr.Ing. Thesis)
IMT-2006-15	Holm, Håvard	Numerical calculation of viscous free surface flow around marine structures. (Dr.Ing. Thesis)
IMT-2006-16	Bjørheim, Lars G.	Failure Assessment of Long Through Thickness Fatigue Cracks in Ship Hulls. (Dr.Ing. Thesis)
IMT-2006-17	Hansson, Lisbeth	Safety Management for Prevention of Occupational Accidents. (Dr.Ing. Thesis)
IMT-2006-18	Zhu, Xinying	Application of the CIP Method to Strongly Nonlinear Wave-Body Interaction Problems. (Dr.Ing. Thesis)
IMT-2006-19	Reite, Karl Johan	Modelling and Control of Trawl Systems. (Dr.Ing. Thesis)
IMT-2006-20	Smogeli, Øyvind Notland	Control of Marine Propellers. From Normal to Extreme Conditions. (Dr.Ing. Thesis)
IMT-2007-21	Storhaug, Gaute	Experimental Investigation of Wave Induced Vibrations and Their Effect on the Fatigue Loading of Ships. (Dr.Ing. Thesis)
IMT-2007-22	Sun, Hui	A Boundary Element Method Applied to Strongly Nonlinear Wave-Body Interaction Problems. (PhD Thesis, CeSOS)

IMT-2007-23	Rustad, Anne Marthine	Modelling and Control of Top Tensioned Risers. (PhD Thesis, CeSOS)
IMT-2007-24	Johansen, Vegar	Modelling flexible slender system for real-time simulations and control applications
IMT-2007-25	Wroldsen, Anders Sunde	Modelling and control of tensegrity structures. (PhD Thesis, CeSOS)
IMT-2007-26	Aronsen, Kristoffer Høye	An experimental investigation of in-line and combined inline and cross flow vortex induced vibrations. (Dr. avhandling, IMT)
IMT-2007-27	Gao, Zhen	Stochastic Response Analysis of Mooring Systems with Emphasis on Frequency-domain Analysis of Fatigue due to Wide-band Response Processes (PhD Thesis, CeSOS)
IMT-2007-28	Thorstensen, Tom Anders	Lifetime Profit Modelling of Ageing Systems Utilizing Information about Technical Condition. (Dr.ing. thesis, IMT)
IMT-2008-29	Refsnes, Jon Erling Gorset	Nonlinear Model-Based Control of Slender Body AUVs (PhD Thesis, IMT)
IMT-2008-30	Berntsen, Per Ivar B.	Structural Reliability Based Position Mooring. (PhD-Thesis, IMT)
IMT-2008-31	Ye, Naiquan	Fatigue Assessment of Aluminium Welded Box-stiffener Joints in Ships (Dr.ing. thesis, IMT)
IMT-2008-32	Radan, Damir	Integrated Control of Marine Electrical Power Systems. (PhD-Thesis, IMT)
IMT-2008-33	Thomassen, Paul	Methods for Dynamic Response Analysis and Fatigue Life Estimation of Floating Fish Cages. (Dr.ing. thesis, IMT)
IMT-2008-34	Pákozdi, Csaba	A Smoothed Particle Hydrodynamics Study of Two-dimensional Nonlinear Sloshing in Rectangular Tanks. (Dr.ing.thesis, IMT/ CeSOS)
IMT-2007-35	Grytøyr, Guttorm	A Higher-Order Boundary Element Method and Applications to Marine Hydrodynamics. (Dr.ing.thesis, IMT)
IMT-2008-36	Drummen, Ingo	Experimental and Numerical Investigation of Nonlinear Wave-Induced Load Effects in Containerships considering Hydroelasticity. (PhD thesis, CeSOS)
IMT-2008-37	Skejic, Renato	Maneuvering and Seakeeping of a Singel Ship and of Two Ships in Interaction. (PhD-Thesis, CeSOS)
IMT-2008-38	Harlem, Alf	An Age-Based Replacement Model for Repairable Systems with Attention to High-Speed Marine Diesel Engines. (PhD-Thesis, IMT)
IMT-2008-39	Alsos, Hagbart S.	Ship Grounding. Analysis of Ductile Fracture, Bottom Damage and Hull Girder Response. (PhD-thesis, IMT)

IMT-2008-40	Graczyk, Mateusz	Experimental Investigation of Sloshing Loading and Load Effects in Membrane LNG Tanks Subjected to Random Excitation. (PhD-thesis, CeSOS)
IMT-2008-41	Taghipour, Reza	Efficient Prediction of Dynamic Response for Flexible amd Multi-body Marine Structures. (PhD-thesis, CeSOS)
IMT-2008-42	Ruth, Eivind	Propulsion control and thrust allocation on marine vessels. (PhD thesis, CeSOS)
IMT-2008-43	Nystad, Bent Helge	Technical Condition Indexes and Remaining Useful Life of Aggregated Systems. PhD thesis, IMT
IMT-2008-44	Soni, Prashant Kumar	Hydrodynamic Coefficients for Vortex Induced Vibrations of Flexible Beams, PhD thesis, CeSOS
IMT-2009-45	Amlashi, Hadi K.K.	Ultimate Strength and Reliability-based Design of Ship Hulls with Emphasis on Combined Global and Local Loads. PhD Thesis, IMT
IMT-2009-46	Pedersen, Tom Arne	Bond Graph Modelling of Marine Power Systems. PhD Thesis, IMT
IMT-2009-47	Kristiansen, Trygve	Two-Dimensional Numerical and Experimental Studies of Piston-Mode Resonance. PhD-Thesis, CeSOS
IMT-2009-48	Ong, Muk Chen	Applications of a Standard High Reynolds Number Model and a Stochastic Scour Prediction Model for Marine Structures. PhD-thesis, IMT
IMT-2009-49	Hong, Lin	Simplified Analysis and Design of Ships subjected to Collision and Grounding. PhD-thesis, IMT
IMT-2009-50	Koushan, Kamran	Vortex Induced Vibrations of Free Span Pipelines, PhD thesis, IMT
IMT-2009-51	Korsvik, Jarl Eirik	Heuristic Methods for Ship Routing and Scheduling. PhD-thesis, IMT
IMT-2009-52	Lee, Jihoon	Experimental Investigation and Numerical in Analyzing the Ocean Current Displacement of Longlines. Ph.d.-Thesis, IMT.
IMT-2009-53	Vestbøstad, Tone Gran	A Numerical Study of Wave-in-Deck Impact usin a Two-Dimensional Constrained Interpolation Profile Method, Ph.d.thesis, CeSOS.
IMT-2009-54	Bruun, Kristine	Bond Graph Modelling of Fuel Cells for Marine Power Plants. Ph.d.-thesis, IMT
IMT 2009-55	Holstad, Anders	Numerical Investigation of Turbulence in a Sekwed Three-Dimensional Channel Flow, Ph.d.-thesis, IMT.
IMT 2009-56	Ayala-Uraga, Efren	Reliability-Based Assessment of Deteriorating Ship-shaped Offshore Structures, Ph.d.-thesis, IMT

IMT 2009-57	Kong, Xiangjun	A Numerical Study of a Damaged Ship in Beam Sea Waves. Ph.d.-thesis, IMT/CeSOS.
IMT 2010-58	Kristiansen, David	Wave Induced Effects on Floaters of Aquaculture Plants, Ph.d.-thesis, CeSOS.
IMT 2010-59	Ludvigsen, Martin	An ROV-Toolbox for Optical and Acoustic Scientific Seabed Investigation. Ph.d.-thesis IMT.
IMT 2010-60	Hals, Jørgen	Modelling and Phase Control of Wave-Energy Converters. Ph.d.thesis, CeSOS.
IMT 2010- 61	Shu, Zhi	Uncertainty Assessment of Wave Loads and Ultimate Strength of Tankers and Bulk Carriers in a Reliability Framework. Ph.d. Thesis, IMT/ CeSOS
IMT 2010-62	Shao, Yanlin	Numerical Potential-Flow Studies on Weakly-Nonlinear Wave-Body Interactions with/without Small Forward Speed, Ph.d.thesis,CeSOS.
IMT 2010-63	Califano, Andrea	Dynamic Loads on Marine Propellers due to Intermittent Ventilation. Ph.d.thesis, IMT.
IMT 2010-64	El Khoury, George	Numerical Simulations of Massively Separated Turbulent Flows, Ph.d.-thesis, IMT
IMT 2010-65	Seim, Knut Sponheim	Mixing Process in Dense Overflows with Emphasis on the Faroe Bank Channel Overflow. Ph.d.thesis, IMT
IMT 2010-66	Jia, Huirong	Structural Analysis of Intect and Damaged Ships in a Collission Risk Analysis Perspective. Ph.d.thesis CeSoS.
IMT 2010-67	Jiao, Linlin	Wave-Induced Effects on a Pontoon-type Very Large Floating Structures (VLFS). Ph.D.-thesis, CeSOS.
IMT 2010-68	Abrahamsen, Bjørn Christian	Sloshing Induced Tank Roof with Entrapped Air Pocket. Ph.d.thesis, CeSOS.
IMT 2011-69	Karimirad, Madjid	Stochastic Dynamic Response Analysis of Spar-Type Wind Turbines with Catenary or Taut Mooring Systems. Ph.d.-thesis, CeSOS.
IMT - 2011-70	Erlend Meland	Condition Monitoring of Safety Critical Valves. Ph.d.-thesis, IMT.
IMT – 2011-71	Yang, Limin	Stochastic Dynamic System Analysis of Wave Energy Converter with Hydraulic Power Take-Off, with Particular Reference to Wear Damage Analysis, Ph.d. Thesis, CeSOS.
IMT – 2011-72	Visscher, Jan	Application of Particla Image Velocimetry on Turbulent Marine Flows, Ph.d.Thesis, IMT.
IMT – 2011-73	Su, Biao	Numerical Predictions of Global and Local Ice Loads on Ships. Ph.d.Thesis, CeSOS.
IMT – 2011-74	Liu, Zhenhui	Analytical and Numerical Analysis of Iceberg Collision with Ship Structures. Ph.d.Thesis, IMT.

IMT – 2011-75	Aarsæther, Karl Gunnar	Modeling and Analysis of Ship Traffic by Observation and Numerical Simulation. Ph.d.Thesis, IMT.
Imt – 2011-76	Wu, Jie	Hydrodynamic Force Identification from Stochastic Vortex Induced Vibration Experiments with Slender Beams. Ph.d.Thesis, IMT.
Imt – 2011-77	Amini, Hamid	Azimuth Propulsors in Off-design Conditions. Ph.d.Thesis, IMT.
IMT – 2011-78	Nguyen, Tan-Hoi	Toward a System of Real-Time Prediction and Monitoring of Bottom Damage Conditions During Ship Grounding. Ph.d.thesis, IMT.
IMT- 2011-79	Tavakoli, Mohammad T.	Assessment of Oil Spill in Ship Collision and Grounding, Ph.d.thesis, IMT.
IMT- 2011-80	Guo, Bingjie	Numerical and Experimental Investigation of Added Resistance in Waves. Ph.d.Thesis, IMT.
IMT- 2011-81	Chen, Qiaofeng	Ultimate Strength of Aluminium Panels, considering HAZ Effects, IMT
IMT- 2012-82	Kota, Ravikiran S.	Wave Loads on Decks of Offshore Structures in Random Seas, CeSOS.
IMT- 2012-83	Sten, Ronny	Dynamic Simulation of Deep Water Drilling Risers with Heave Compensating System, IMT.
IMT- 2012-84	Berle, Øyvind	Risk and resilience in global maritime supply chains, IMT.
IMT- 2012-85	Fang, Shaoji	Fault Tolerant Position Mooring Control Based on Structural Reliability, CeSOS.
IMT- 2012-86	You, Jikun	Numerical studies on wave forces and moored ship motions in intermediate and shallow water, CeSOS.
IMT- 2012-87	Xiang ,Xu	Maneuvering of two interacting ships in waves, CeSOS
IMT- 2012-88	Dong, Wenbin	Time-domain fatigue response and reliability analysis of offshore wind turbines with emphasis on welded tubular joints and gear components, CeSOS
IMT- 2012-89	Zhu, Suji	Investigation of Wave-Induced Nonlinear Load Effects in Open Ships considering Hull Girder Vibrations in Bending and Torsion, CeSOS
IMT- 2012-90	Zhou, Li	Numerical and Experimental Investigation of Station-keeping in Level Ice, CeSOS
IMT- 2012-91	Ushakov, Sergey	Particulate matter emission characteristics from diesel enignes operating on conventional and alternative marine fuels, IMT
IMT- 2013-1	Yin, Decao	Experimental and Numerical Analysis of Combined In-line and Cross-flow Vortex Induced Vibrations, CeSOS

IMT-2013-2	Kurniawan, Adi	Modelling and geometry optimisation of wave energy converters, CeSOS
IMT-2013-3	Al Ryati, Nabil	Technical condition indexes doe auxiliary marine diesel engines, IMT
IMT-2013-4	Firoozkoohi, Reza	Experimental, numerical and analytical investigation of the effect of screens on sloshing, CeSOS
IMT-2013-5	Ommani, Babak	Potential-Flow Predictions of a Semi-Displacement Vessel Including Applications to Calm Water Broaching, CeSOS
IMT-2013-6	Xing, Yihan	Modelling and analysis of the gearbox in a floating spar-type wind turbine, CeSOS
IMT-7-2013	Balland, Océane	Optimization models for reducing air emissions from ships, IMT
IMT-8-2013	Yang, Dan	Transitional wake flow behind an inclined flat plate-----Computation and analysis, IMT
IMT-9-2013	Abdillah, Suyuthi	Prediction of Extreme Loads and Fatigue Damage for a Ship Hull due to Ice Action, IMT
IMT-10-2013	Ramìrez, Pedro Agustìn Pèrez	Ageing management and life extension of technical systems- Concepts and methods applied to oil and gas facilities, IMT
IMT-11-2013	Chuang, Zhenju	Experimental and Numerical Investigation of Speed Loss due to Seakeeping and Maneuvering. IMT
IMT-12-2013	Etemaddar, Mahmoud	Load and Response Analysis of Wind Turbines under Atmospheric Icing and Controller System Faults with Emphasis on Spar Type Floating Wind Turbines, IMT
IMT-13-2013	Lindstad, Haakon	Strategies and measures for reducing maritime CO_2 emissons, IMT
IMT-14-2013	Haris, Sabril	Damage interaction analysis of ship collisions, IMT
IMT-15-2013	Shainee, Mohamed	Conceptual Design, Numerical and Experimental Investigation of a SPM Cage Concept for Offshore Mariculture, IMT
IMT-16-2013	Gansel, Lars	Flow past porous cylinders and effects of biofouling and fish behavior on the flow in and around Atlantic salmon net cages, IMT
IMT-17-2013	Gaspar, Henrique	Handling Aspects of Complexity in Conceptual Ship Design, IMT
IMT-18-2013	Thys, Maxime	Theoretical and Experimental Investigation of a Free Running Fishing Vessel at Small Frequency of Encounter, CeSOS
IMT-19-2013	Aglen, Ida	VIV in Free Spanning Pipelines, CeSOS

IMT-1-2014	Song, An	Theoretical and experimental studies of wave diffraction and radiation loads on a horizontally submerged perforated plate, CeSOS
IMT-2-2014	Rogne, Øyvind Ygre	Numerical and Experimental Investigation of a Hinged 5-body Wave Energy Converter, CeSOS
IMT-3-2014	Dai, Lijuan	Safe and efficient operation and maintenance of offshore wind farms ,IMT
IMT-4-2014	Bachynski, Erin Elizabeth	Design and Dynamic Analysis of Tension Leg Platform Wind Turbines, CeSOS
IMT-5-2014	Wang, Jingbo	Water Entry of Freefall Wedged – Wedge motions and Cavity Dynamics, CeSOS
IMT-6-2014	Kim, Ekaterina	Experimental and numerical studies related to the coupled behavior of ice mass and steel structures during accidental collisions, IMT
IMT-7-2014	Tan, Xiang	Numerical investigation of ship's continuous- mode icebreaking in leverl ice, CeSOS
IMT-8-2014	Muliawan, Made Jaya	Design and Analysis of Combined Floating Wave and Wind Power Facilities, with Emphasis on Extreme Load Effects of the Mooring System, CeSOS
IMT-9-2014	Jiang, Zhiyu	Long-term response analysis of wind turbines with an emphasis on fault and shutdown conditions, IMT
IMT-10-2014	Dukan, Fredrik	ROV Motion Control Systems, IMT
IMT-11-2014	Grimsmo, Nils I.	Dynamic simulations of hydraulic cylinder for heave compensation of deep water drilling risers, IMT
IMT-12-2014	Kvittem, Marit I.	Modelling and response analysis for fatigue design of a semisubmersible wind turbine, CeSOS
IMT-13-2014	Akhtar, Juned	The Effects of Human Fatigue on Risk at Sea, IMT
IMT-14-2014	Syahroni, Nur	Fatigue Assessment of Welded Joints Taking into Account Effects of Residual Stress, IMT
IMT-1-2015	Bøckmann, Eirik	Wave Propulsion of ships, IMT
IMT-2-2015	Wang, Kai	Modelling and dynamic analysis of a semi-submersible floating vertical axis wind turbine, CeSOS
IMT-3-2015	Fredriksen, Arnt Gunvald	A numerical and experimental study of a two-dimensional body with moonpool in waves and current, CeSOS
IMT-4-2015	Jose Patricio Gallardo Canabes	Numerical studies of viscous flow around bluff bodies, IMT

IMT-5-2015	Vegard Longva	Formulation and application of finite element techniques for slender marine structures subjected to contact interactions, IMT
IMT-6-2015	Jacobus De Vaal	Aerodynamic modelling of floating wind turbines, CeSOS
IMT-7-2015	Fachri Nasution	Fatigue Performance of Copper Power Conductors, IMT
IMT-8-2015	Oleh I Karpa	Development of bivariate extreme value distributions for applications in marine technology,CeSOS
IMT-9-2015	Daniel de Almeida Fernandes	An output feedback motion control system for ROVs, AMOS
IMT-10-2015	Bo Zhao	Particle Filter for Fault Diagnosis: Application to Dynamic Positioning Vessel and Underwater Robotics, CeSOS
IMT-11-2015	Wenting Zhu	Impact of emission allocation in maritime transportation, IMT
IMT-12-2015	Amir Rasekhi Nejad	Dynamic Analysis and Design of Gearboxes in Offshore Wind Turbines in a Structural Reliability Perspective, CeSOS
IMT-13-2015	Arturo Jesùs Ortega Malca	Dynamic Response of Flexibles Risers due to Unsteady Slug Flow, CeSOS
IMT-14-2015	Dagfinn Husjord	Guidance and decision-support system for safe navigation of ships operating in close proximity, IMT
IMT-15-2015	Anirban Bhattacharyya	Ducted Propellers: Behaviour in Waves and Scale Effects, IMT
IMT-16-2015	Qin Zhang	Image Processing for Ice Parameter Identification in Ice Management, IMT
IMT-1-2016	Vincentius Rumawas	Human Factors in Ship Design and Operation: An Experiential Learning, IMT
IMT-2-2016	Martin Storheim	Structural response in ship-platform and ship-ice collisions, IMT
IMT-3-2016	Mia Abrahamsen Prsic	Numerical Simulations of the Flow around single and Tandem Circular Cylinders Close to a Plane Wall, IMT
IMT-4-2016	Tufan Arslan	Large-eddy simulations of cross-flow around ship sections, IMT
IMT-5-2016	Pierre Yves-Henry	Parametrisation of aquatic vegetation in hydraulic and coastal research,IMT

IMT-6-2016	Lin Li	Dynamic Analysis of the Instalation of Monopiles for Offshore Wind Turbines, CeSOS
IMT-7-2016	Øivind Kåre Kjerstad	Dynamic Positioning of Marine Vessels in Ice, IMT
IMT-8-2016	Xiaopeng Wu	Numerical Analysis of Anchor Handling and Fish Trawling Operations in a Safety Perspective, CeSOS
IMT-9-2016	Zhengshun Cheng	Integrated Dynamic Analysis of Floating Vertical Axis Wind Turbines, CeSOS
IMT-10-2016	Ling Wan	Experimental and Numerical Study of a Combined Offshore Wind and Wave Energy Converter Concept
IMT-11-2016	Wei Chai	Stochastic dynamic analysis and reliability evaluation of the roll motion for ships in random seas, CeSOS
IMT-12-2016	Øyvind Selnes Patricksson	Decision support for conceptual ship design with focus on a changing life cycle and future uncertainty, IMT
IMT-13-2016	Mats Jørgen Thorsen	Time domain analysis of vortex-induced vibrations, IMT
IMT-14-2016	Edgar McGuinness	Safety in the Norwegian Fishing Fleet – Analysis and measures for improvement, IMT
IMT-15-2016	Sepideh Jafarzadeh	Energy effiency and emission abatement in the fishing fleet, IMT
IMT-16-2016	Wilson Ivan Guachamin Acero	Assessment of marine operations for offshore wind turbine installation with emphasis on response-based operational limits, IMT
IMT-17-2016	Mauro Candeloro	Tools and Methods for Autonomous Operations on Seabed and Water Coumn using Underwater Vehicles, IMT
IMT-18-2016	Valentin Chabaud	Real-Time Hybrid Model Testing of Floating Wind Tubines, IMT
IMT-1-2017	Mohammad Saud Afzal	Three-dimensional streaming in a sea bed boundary layer
IMT-2-2017	Peng Li	A Theoretical and Experimental Study of Wave-induced Hydroelastic Response of a Circular Floating Collar
IMT-3-2017	Martin Bergström	A simulation-based design method for arctic maritime transport systems
IMT-4-2017	Bhushan Taskar	The effect of waves on marine propellers and propulsion

IMT-5-2017	Mohsen Bardestani	A two-dimensional numerical and experimental study of a floater with net and sinker tube in waves and current
IMT-6-2017	Fatemeh Hoseini Dadmarzi	Direct Numerical Simualtion of turbulent wakes behind different plate configurations
IMT-7-2017	Michel R. Miyazaki	Modeling and control of hybrid marine power plants
IMT-8-2017	Giri Rajasekhar Gunnu	Safety and effiency enhancement of anchor handling operations with particular emphasis on the stability of anchor handling vessels
IMT-9-2017	Kevin Koosup Yum	Transient Performance and Emissions of a Turbocharged Diesel Engine for Marine Power Plants
IMT-10-2017	Zhaolong Yu	Hydrodynamic and structural aspects of ship collisions
IMT-11-2017	Martin Hassel	Risk Analysis and Modelling of Allisions between Passing Vessels and Offshore Installations
IMT-12-2017	Astrid H. Brodtkorb	Hybrid Control of Marine Vessels – Dynamic Positioning in Varying Conditions
IMT-13-2017	Kjersti Bruserud	Simultaneous stochastic model of waves and current for prediction of structural design loads
IMT-14-2017	Finn-Idar Grøtta Giske	Long-Term Extreme Response Analysis of Marine Structures Using Inverse Reliability Methods
IMT-15-2017	Stian Skjong	Modeling and Simulation of Maritime Systems and Operations for Virtual Prototyping using co-Simulations
IMT-1-2018	Yingguang Chu	Virtual Prototyping for Marine Crane Design and Operations
IMT-2-2018	Sergey Gavrilin	Validation of ship manoeuvring simulation models
IMT-3-2018	Jeevith Hegde	Tools and methods to manage risk in autonomous subsea inspection,maintenance and repair operations
IMT-4-2018	Ida M. Strand	Sea Loads on Closed Flexible Fish Cages
IMT-5-2018	Erlend Kvinge Jørgensen	Navigation and Control of Underwater Robotic Vehicles
IMT-6-2018	Bård Stovner	Aided Intertial Navigation of Underwater Vehicles

IMT-7-2018	Erlend Liavåg Grotle	Thermodynamic Response Enhanced by Sloshing in Marine LNG Fuel Tanks
IMT-8-2018	Børge Rokseth	Safety and Verification of Advanced Maritime Vessels
IMT-9-2018	Jan Vidar Ulveseter	Advances in Semi-Empirical Time Domain Modelling of Vortex-Induced Vibrations
IMT-10-2018	Chenyu Luan	Design and analysis for a steel braceless semi-submersible hull for supporting a 5-MW horizontal axis wind turbine
IMT-11-2018	Carl Fredrik Rehn	Ship Design under Uncertainty
IMT-12-2018	Øyvind Ødegård	Towards Autonomous Operations and Systems in Marine Archaeology
IMT-13-2018	Stein Melvær Nornes	Guidance and Control of Marine Robotics for Ocean Mapping and Monitoring
IMT-14-2018	Petter Norgren	Autonomous Underwater Vehicles in Arctic Marine Operations: Arctic marine research and ice monitoring
IMT-15-2018	Minjoo Choi	Modular Adaptable Ship Design for Handling Uncertainty in the Future Operating Context
MT-16-2018	Ole Alexander Eidsvik	Dynamics of Remotely Operated Underwater Vehicle Systems
IMT-17-2018	Mahdi Ghane	Fault Diagnosis of Floating Wind Turbine Drivetrain- Methodologies and Applications
IMT-18-2018	Christoph Alexander Thieme	Risk Analysis and Modelling of Autonomous Marine Systems
IMT-19-2018	Yugao Shen	Operational limits for floating-collar fish farms in waves and current, without and with well-boat presence
IMT-20-2018	Tianjiao Dai	Investigations of Shear Interaction and Stresses in Flexible Pipes and Umbilicals
IMT-21-2018	Sigurd Solheim Pettersen	Resilience by Latent Capabilities in Marine Systems
IMT-22-2018	Thomas Sauder	Fidelity of Cyber-physical Empirical Methods. Application to the Active Truncation of Slender Marine Structures
IMT-23-2018	Jan-Tore Horn	Statistical and Modelling Uncertainties in the Design of Offshore Wind Turbines
IMT-24-2018	Anna Swider	Data Mining Methods for the Analysis of Power Systems of Vessels

IMT-16-2020	Asle Natskår	Reliability-based Assessment of Marine Operations with Emphasis on Sea Transport on Barges
IMT-17-2020	Shi Deng	Experimental and Numerical Study of Hydrodynamic Responses of a Twin-Tube Submerged Floating Tunnel Considering Vortex-Induced Vibration
IMT-18-2020	Jone Torsvik	Dynamic Analysis in Design and Operation of Large Floating Offshore Wind Turbine Drivetrains
IMT-1-2021	Ali Ebrahimi	Handling Complexity to Improve Ship Design Competitiveness
IMT-2-2021	Davide Proserpio	Isogeometric Phase-Field Methods for Modeling Fracture in Shell Structures
IMT-3-2021	Cai Tian	Numerical Studies of Viscous Flow Around Step Cylinders
IMT-4-2021	Farid Khazaeli Moghadam	Vibration-based Condition Monitoring of Large Offshore Wind Turbines in a Digital Twin Perspective
IMT-5-2021	Shuaishuai Wang	Design and Dynamic Analysis of a 10-MW Medium-Speed Drivetrain in Offshore Wind Turbines
IMT-6-2021	Sadi Tavakoli	Ship Propulsion Dynamics and Emissions
IMT-7-2021	Haoran Li	Nonlinear wave loads, and resulting global response statistics of a semi-submersible wind turbine platform with heave plates
IMT-8-2021	Einar Skiftestad Ueland	Load Control for Real-Time Hybrid Model Testing using Cable-Driven Parallel Robots
IMT-9-2021	Mengning Wu	Uncertainty of machine learning-based methods for wave forecast and its effect on installation of offshore wind turbines
IMT-10-2021	Xu Han	Onboard Tuning and Uncertainty Estimation of Vessel Seakeeping Model Parameters
IMT-01-2022	Ingunn Marie Holmen	Safety in Exposed Aquacultrue Operations
IMT-02-2022	Prateek Gupta	Ship Performance Monitoring using In-service Measurements and Big Data Analysis Methods
IMT-03-2022	Sangwoo Kim	Non-linear time domain analysis of deepwater riser vortex-induced vibrations
IMT-04-2022	Jarle Vinje Kramer	Hydrodynamic Aspects of Sail-Assisted Merchant Vessels
IMT-05-2022	Øyvind Rabliås	Numerical and Expermental Studies of Maneuvering in Regular and Irregular Waves

IMT-06-2022	Pramod Ghimire	Simulation-Based Ship Hybrid Power System Conspet Studies and Performance Analyses
IMT-07-2022	Carlos Eduardo Silva de Souza	Structural modelling, coupled dynamics, and design of large floating wind turbines
IMT-08-2022	Lorenzo Balestra	Design of hybrid fuel cell & battery systems for maritime vessels
IMT-09-2022	Sharmin Sultana	Process safety and risk management using system perspectives – A contribution to the chemical process and petroleum industry
IMT-10-2022	Øystein Sture	Autonomous Exploration for Marine Minerals
IMT-11-2022	Tiantian Zhu	Information and Decision-making for Major Accident Prevention – A concept of information-based strategies for accident prevention
IMT-12-2022	Siamak Karimi	Shore-to-Ship Charging Systems for Battery-Electric Ships
IMT-01-2023	Huili Xu	Fish-inspired Propulsion Study: Numerical Hydrodynamics of Rigid/Flexible/Morphing Foils and Observations on Real Fish
IMT-02-2023	Chana Sinsabvarodom	Probabilistic Modelling of Ice-drift and Ice Loading on Fixed and Floating Offshore Structures
IMT-03-2023	Martin Skaldebø	Intelligent low-cost solutions for underwater intervention using computer vision and machine learning
IMT-04-2023	Hans Tobias Slette	Vessel operations in exposed aquaculture – Achieving safe and efficient operation of vessel fleets in fish farm systems experiencing challenging metocean conditions
IMT-05-2023	Ruochen Yang	Methods and models for analyzing and controlling the safety in operations of autonomous marine systems
IMT-06-2023	Tobias Rye Torben	Formal Approaches to Design and Verification of Safe Control Systems for Autonomous Vessels
IMT-07-2023	YoungRong Kim	Modeling Operational Performance for the Global Fleet & Application of an Energy Saving Measure
IMT-08-2023	Henrik Schmidt-Didlaukies	Modeling and Hybrid Feedback Control of Underwater Vehicles
IMT-09-2023	Ehsan Esmailian	Optimal Ship Design for Operating in Real Sea States
IMT-10-2023	Astrid Vamråk Solheim	Exploring the performance of conceptual offshore production systems for deep-sea mining
IMT-11-2023	Benjamin Lagemann	Conceptual design of low-emission ships